Fluid Dynamics in Liquid Entry and Exit

Seong Jin Kim

Dissertation submitted to the faculty of
Virginia Polytechnic Institute and State University
in partial fulfillment of the requirements for the degree of

Doctor of Philosophy
in Engineering Mechanics

Sunghwan Jung, Chair
Mark S. Cramer
Nicole T. Abaid
Anne E. Staples
Chang Lu

Keywords: Surface tension, water-entry, water-exit, contact line

September 12, 2017
Blacksburg, Virginia

Fluid Dynamics in Liquid Entry and Exit

Seong Jin Kim

Abstract

Interaction between a solid body and a liquid-air interface plays an important role in multiphase flows, which includes numerous engineering applications such as mineral flotation [92, 93], dip coating operations [129], and air-to-sea & sea-to-air projectiles [143]. It is also crucial in animal behaviors like the locomotion of water-walking animals [16], the plunge-diving of birds [19], and the jumping out of water of marine creatures [77]. Depending on the moving direction of a solid, such diverse phenomena can be classified into two categories; liquid-entry and liquid-exit. Liquid-entry, or more widely called water-entry, is the behavior of a solid object entering liquid from air. The opposite case is referred to as liquid-exit.

Liquid-entry has been extensively studied, especially focusing on cavity formation [5] and the estimation on capillary and hydrodynamic forces on a solid object [16, 19]. However, as the behavior of a triple contact line has not been understood on a sinking object, previous studies were limited to the special case of hydrophobic object to fix the contact line [5]. Moreover, a more recent study [92] pointed out the important role of contact line behavior to characterize the performance of film flotation, which is one of the direct applications of liquid-entry. However, there are no existing previous studies on the dynamics of the contact line on a sinking object. This subject will be first discussed in Chapter 2.

In Chapters 3 & 4, the topics related to liquid-exit will be discussed, where a solid sphere exits out of a liquid toward air with constant velocity, acceleration, or deceleration. Chapter 3 will focus on the penetration & bouncing behaviors of a solid sphere while impacting a liquid-air interface. The solid sphere experiences the resistance of surface tension and gravity while impacting the interface. Thus, liquid-exit spheres should have enough momentum to penetrate the interface to overcome these resistances, which indicates that the critical momentum exits. This understanding would give a mechanistic explanation as to why some aquatic species, especially plankton, are able to jump out of water while the others cannot

despite their similar size [77]. This study can help to understand the particle-bubble interaction for froth flotation applications [156], in which the particle tends to attach to the bubble.

In the last Chapter, the formation of a liquid column during the liquid-exit will be discussed. It has been observed that the evolution of a liquid column strongly depends on experimental conditions, especially the acceleration of a solid sphere. The pinch-off dynamics of a liquid column is categorized as two branches: upper and lower pinch-off's. The pinch-off location affects the entrained liquid volume adhered to the solid object, which is directly related to the uniform quality of a dip-coating operation [129]. In addition to the pinch-off location and time in relation to the aforementioned experimental conditions will be discussed.

In summary, studies in the present dissertation are designed and performed to provide mechanistic insight to the problems in the liquid-entry and liquid-exit, which are all closely related to animal's daily life as well as engineering applications.

Fluid Dynamics in Liquid Entry and Exit

Seong Jin Kim

General audience abstract

Interactions between a solid body and a liquid-air interface play an important role in multiphase flows, which is also crucial in animal behaviors [16, 19, 77] and numerous engineering applications [92, 93, 129, 143]. Depending on the moving direction of a solid, such diverse phenomena can be classified into two categories; liquid-entry and liquid-exit. Liquid-entry is when a solid object enters a liquid from air. The opposite case is referred to as liquid-exit.

In the Chapter 2, contact-line spreading dynamics on a sinking solid sphere will be discussed, where the contact-line indicates the line meeting all three phases of liquid/air/solid. The contact line motion is important as this local motion significantly affects macroscopic liquid flow. Experiments performed in high temporal and spatial resolutions by x-ray illumination show the characteristics of capillarity-driven (in other words, driven by the surface tension) spreading up to the sinking speed ≈ 1 m/s. Scaling dynamics based on capillary-viscous and capillary-inertial balances are observed to rationalize the contact-line motion.

In the last two Chapters, the liquid-exit behaviors will be presented with focusing on a liquid-exit solid (Chapter 3) and a stretched liquid column (Chapter 4). The penetration & bouncing behaviors while a solid sphere exits out of a liquid bath are viewed in analogy with bio-example of jumping and non-jumping plankton. The dynamics on the liquid-exit sphere are described by the exit-momentum of the sphere and the resistance of surface tension and gravity. Lastly, the pinch-off dynamics on the stretched liquid column are investigated with noticing that the column evolution shifts from capillarity-driven to inertial-driven as the sphere exits out with higher acceleration.

Dedication

I would like to dedicate this thesis to God and my beloved wife and mother

Acknowledgements

First of all, I would like to thank God for his guidance on my study.

During my doctoral course, I receive real favors and numerous helps from my advisor, Prof. Sunghwan Jung. I sincerely appreciate all of academic and personal supports from him. I feel that it has been a great luck for me to meet and know him in my life. Advising from Prof. S. Jung motivates me to challenge becoming a great advisor like him.

I hope to express my deep thanks and love to my family. Without them, I couldn't start this work. I thank for them to be the reason for me to live and study.

Also, I acknowledge that all works written in this dissertation couldn't be done without helps from others. The experiment by use of x-ray on Chapter 2 was greatly helped by Dr. Kamel Fezzaa and Dr. Tao Sun in Argonne National Laboratory. Also, I appreciate for theoretical discussion with Prof. Sungyon Lee in Texas A&M University on the work in Chapter 3. In the same chapter, the biological discussion especially about plankton, it was helped by Prof. Brad J. Gemmell in University of South Florida. And I also express my deep thanks to Jalil Hasanyan, Jim An, and Michael Valosin in Virginia Tech for helping experiments and data processing. Also, I hope to appreciate the helps and supports from my labmates: Dr. Sean Gart, Dr. Peng Zhang, Stephane Poulain, and Brian Chang.

Table of contents

List of figures

List of tables

Chapter 1

Background

1.1 Concept of surface-tension

Surface tension is a substantial concept in understanding liquid behavior interacting with its interface, especially on the length-scale less than a centimeter. Surface tension indicates the tension acting along the surface or interface between two different phases, e.g. the interface between water and air. It originates from attraction between molecules. Let me consider liquid molecules inside a liquid bulk as shown in Fig. 1.1(a). As all molecules attract each other, a molecule is supposed to experience almost zero resultant force as denoted by the molecule colored in purple. However, molecules near an interface (e.g. an interface with air as in Fig. 1.1(b)) experience inward resultant force due to weak attraction from

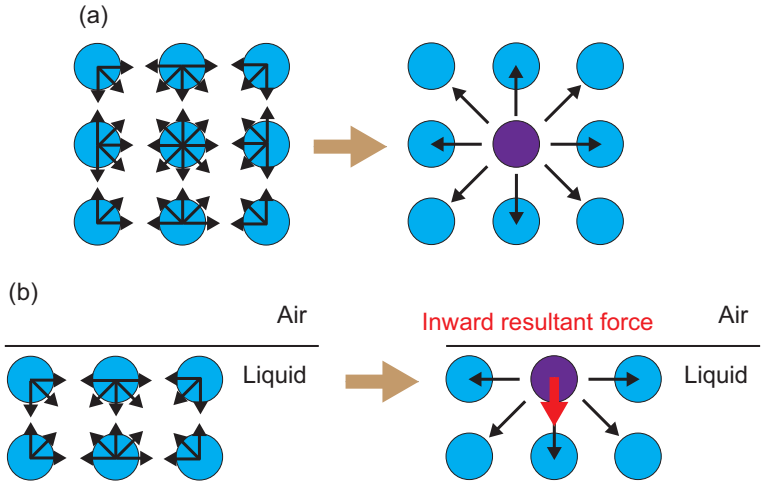

Fig. 1.1 Schematic of liquid molecules attracting each other located (a) inside liquid bulk and (b) near the interface between liquid and air.

air molecules. The inward force makes the liquid to be cohesive at the interface, in other words, lets the liquid/air system to reduce the interfacial area as much as it could. The line force has been estimated and measured by use of the quantity called 'surface tension coefficient' (σ), or simply 'surface tension', which has the physical unit of N/m. It is named 'tension' because an interface is considered stretched already due to its cohesive nature. When one considers a solid interface such as a solid-air or solid-liquid interface, this cohesive property is more generally referred to as surface 'energy' rather than called 'tension'. It might be because a liquid-air interface is easily-deforming compared to any other solid interfaces, so the terminology of 'tension' would imply better the nuance of the dynamic situation of a deforming interface, e.g. a water drop bouncing on a super-hydrophobic surface. On the contrary, a solid interface is not easily-deformed, thus it is difficult to observe this cohesive property in a dynamic situation. It might be the reason why people have chosen the terminology of 'energy' in order to convey the nuance of the static energy state rather than 'tension' acting in a dynamic state.

Surface tension can be categorized as a line force as σ [N/m] becomes to have force unit when a length scale is multiplied. For an example, the contact line force for a liquid drop spreading on identical liquid can be estimated as '$\sigma\times$ (circumference length of liquid drop)' [79, 78]. As mentioned previously, the surface tension acts always toward the direction to reduce the area of liquid-air interface. If multiple interfaces are considered together, e.g. at triple contact line between liquid-air-solid phases, it acts toward the direction to reduce total surface energy of all interfaces implicated. This is the reason why a liquid drop is able to spread on hydrophilic solid surface as it is energetically favorable even though it inevitably increases the liquid-air interfacial energy by stretching the liquid-air interface. On the other energetic point of view, the surface tension force can be estimated as a negative spatial derivative of interfacial energies in the principle that surface tension force acts to minimize the surface area [77, 76, 120].

1.2 Fluid equation of motion and scaling analysis

To analyze the fluid motion, the equation of motion known as Naiver-Stokes equation should be considered:

$$\rho \frac{D\underline{u}}{Dt} = \rho \left[\frac{\partial \underline{u}}{\partial t} + (\underline{u} \cdot \nabla)\, \underline{u} \right] = -\nabla p + \nabla \cdot \left[\mu (\nabla \underline{u} + \nabla \underline{u}^T) \right] + \rho \underline{g}, \tag{1.1}$$

where $\underline{u}$ is the fluid velocity vector, ρ the density, p the pressure, μ the dynamic viscosity, and $\underline{g}$ the gravitational acceleration vector. The equation is solved generally to obtain $\underline{u}$ and p with specified initial and boundary conditions. Surface tension can be implicated as the boundary condition for p at the interface. Equation (1.1) conceptually states

$$\text{Fluid inertia} = \text{Pressure acting on fluid} + \text{Viscous resistance} + \text{Gravity as body force}. \tag{1.2}$$

However, Eq. (1.1) does not guarantee to yield analytical solution in a general case. Alternatively, people have tried to simplify Eq. (1.1) to be mathematically solvable by eliminating some terms that can be treated as being not important for a specific problem. For this purpose, Eq. (1.1) can be non-dimensionalized by use of suitable length (l) and velocity (U) scales:

$$\mathrm{Re} \left[\frac{\partial \tilde{\underline{u}}}{\partial \tilde{t}} + \left(\tilde{\underline{u}} \cdot \tilde{\nabla} \right) \tilde{\underline{u}} - \frac{1}{\mathrm{Fr}^2} \underline{g} \right] = -\tilde{\nabla} \tilde{p} + \tilde{\nabla}^2 \tilde{\underline{u}}, \tag{1.3}$$

where $\mathrm{Re} = \rho U l / \mu$ and $\mathrm{Fr} = U / \sqrt{gl}$ being well-known dimensionless quantities called Reynolds and Froude numbers, and the tilde indicates dimensionless quantity, and $\tilde{p}$ is non-dimensionalized as $p \times \left[l^2 / (\mu U) \right]$. Thus, for very small Reynolds number, Eq. (1.3) can be further simplified:

$$0 = -\tilde{\nabla} \tilde{p} + \tilde{\nabla}^2 \tilde{\underline{u}}, \tag{1.4}$$

which is widely known as Stokes equation that governs viscous flow. When one non-dimensionalize Eq. (1.1) differently for $\tilde{p}$ as $p \times l / (\rho U^2)$, Eq. (1.1) becomes

$$\frac{\partial \tilde{\underline{u}}}{\partial \tilde{t}} + \left(\tilde{\underline{u}} \cdot \tilde{\nabla} \right) \tilde{\underline{u}} = -\tilde{\nabla} \tilde{p} + \frac{1}{\mathrm{Re}} \tilde{\nabla}^2 \tilde{\underline{u}} + \frac{1}{\mathrm{Fr}^2} \underline{g}. \tag{1.5}$$

For high $\mathrm{Re} \to \infty$, which also accompanies high Fr^2 in general due to dependency on U^2, Eq. (1.5) can be simplified as

$$\frac{\partial \tilde{\underline{u}}}{\partial \tilde{t}} + \left(\tilde{\underline{u}} \cdot \tilde{\nabla} \right) \tilde{\underline{u}} = -\tilde{\nabla} \tilde{p}, \tag{1.6}$$

which is known as Euler equation that approximates inviscid flow. Besides Eqs. (1.4,1.6), numerous equations are available that have been mathematically simplified by employing suitable mathematical techniques such as the perturbation method [66].

Equations (1.1,1.4,1.6) should be solved spatial and temporal fields with specified boundary and initial conditions. For deforming fluid interfaces, following boundary conditions should be applied at the interface

$$\underline{n}\cdot\underline{\underline{T}}\cdot\underline{n} = \sigma(\nabla\cdot\underline{n}) \tag{1.7}$$

$$\underline{n}\cdot\underline{\underline{T}}\cdot\underline{t} = \nabla\sigma\cdot\underline{t}, \tag{1.8}$$

where Eq. (1.7) and Eq. (1.8) specify the force balances at the interface in normal and tangential directions to the interface respectively. Along with it, $\underline{n}$ and $\underline{t}$ indicate the unit normal and tangent to the interface respectively. $\underline{\underline{T}}$ is the stress tensor ($= -p\underline{\underline{I}} + \mu\left[\nabla\underline{u} + (\nabla\underline{u})^T\right]$), where $\underline{\underline{I}}$ is the identity tensor. For inviscid flow ($\mu = 0$), $\underline{\underline{T}} = -p\underline{\underline{I}}$, so that $\underline{n}\cdot\underline{\underline{T}}\cdot\underline{n} = -p$ and $\underline{n}\cdot\underline{\underline{T}}\cdot\underline{t} = 0$. In general, fluid equations such as Eqs. (1.1,1.4,1.6) have been solved numerically for the problems interacting with an effect of surface tension [38, 5, 39, 139]. In those cases, the solution will be given as numerical data.

Instead of seeking an analytical or numerical solution as a function of *spatial* coordinates, rough analytical expression for local fluid motion can be obtained by assuming *a fluid bulk* (or lumped mass), where dominant forces are considered only acting on a location of interest such as the center of local fluid mass or the contact line [128, 120, 79]. In this case, the forces acting on the local fluid body and the corresponding solution can be independent on spatial coordinates. With ignoring spatial variation, analytical expression is more likely sought out compared to the case obtaining the solution as a function of spatial coordinate. This is called *scaling analysis*, which might be rough but powerful to provide order-of-magnitude accuracy and most importantly gives physical insight how physical quantities depend on each other.

Besides this simplification, recent advance in mathematical techniques such as Volume-Of-Fluid method to track fluids interface [67] enables to solve Eq. (1.1) numerically for multiphase problems. Among numerical codes, *Gerris* has been widely used for multiphase simulation and acknowledged reliable in academic community [117, 118]. Appendix C provides detailed explanation on *Gerris* with solving traditional drop-spreading problem on different boundary condition. Moreover, in Chapters 2 & 4, the studies are carried out with numerical simulation by *Gerris* along with experimental validation.

Chapter 2

Capillary spreading of contact line over a sinking sphere

2.1 Abstract

The contact line dynamics over a sinking solid sphere are investigated in comparison with classical spreading theories. Experimentally, high-speed imaging systems with optical light or x-ray illumination are employed to accurately measure the spreading motion and dynamic contact angle of the contact line. Millimetric spheres are controlled to descend with a constant speed ranging from 7.3×10^{-5} to 0.79 m/s. We observed three different spreading stages over a sinking sphere, which depends on the contact line velocity and contact angle. These stages consistently showed the characteristics of capillarity-driven spreading as the contact line spreads faster with a higher contact angle. The contact line velocity is observed to follow a classical capillary-viscous model at a high Ohnesorge number (> 0.02). For the cases with a relatively low Ohnesorge number (< 0.02), the contact line velocity is significantly lower than the speed predicted by the capillary-viscous balance. This indicates the existence of an additional opposing force (inertia) for a decreasing Ohnesorge number. The capillary-inertial balance is only observed at the very beginning of the capillary rise, in which the maximum velocity is independent of the sphere's sinking speed. Additionally, we observed the linear relation between the contact line velocity and the sphere sinking speed during the second stage, which represents capillary adjustment by dynamic contact angle.

Related article

S.J. Kim, K. Fezzaa, J. An, T. Sun, and S. Jung, “Capillary spreading of contact line over a sinking sphere," *Appl. Phys. Lett.* **111**, 134102 (2017).

2.2 Introduction

Dynamics of the triple contact line between a solid and two immiscible fluids have brought up interesting scientific questions and inspired many engineering applications [131, 146, 120, 92, 24]. Traditionally, the spreading behavior of the triple contact line is described as a result of the balance between capillarity and resistant forces in the vicinity of the contact line [11]. R. L. Hoffman in 1975 performed pioneering experimental work and established a relation between the spreading speed (U_c) and the dynamic contact angle (θ)[68], and later provided the molecular explanation for the experimental data [69]. In 1986, P. G. de Gennes derived a mathematical relation as $U_c \propto \sigma\theta(\theta^2 - \theta_s^2)/\mu$ for small θ, which is referred to as the Hoffman-de Gennes equation [29, 104], where σ is the surface tension, μ is the liquid viscosity, and θ_s is the static contact angle. This capillary-viscous model also can be employed to describe the spreading speed of the contact line as a function of time (t). When spreading occurs axi-symmetrically, the spreading speed follows $U_c \propto t^{-9/10}$, known as Tanner's law [139]. Theoretically, Hoffman-de Gennes and Tanner's equations are interchangeable in the case of a spreading droplet with a simple geometry [78]. Even though these equations are derived only for small θ, the equations are experimentally proven to be valid even up to $\theta \approx 150^\circ$ within minor error [131, 47, 20]. It would suggest that the effective region of a small angle exists to endure dominant viscous dissipation [40]. A similar solution, $9\mathrm{Ca}\ln(\alpha l_M/l_m) = \theta^3 - \theta_s^3$, was derived for small Ca $(= \mu U_c/\sigma \ll 1)$ from the matched asymptotic expansion between micro-, meso-, and macroscopic regions. This is known as the Cox-Voinov equation [131, 26, 149], where l_M and l_m are macroscopic & microscopic length scales respectively, and α is a constant.

Besides the capillary-viscous balance, different balances have been introduced to describe the spreading dynamics in different situations [11]. For example, in the case of spreading for a large liquid drop ($a \gg l_c = \sqrt{\sigma/(\rho_l g)}$, where l_c is the capillary length, a is the initial drop radius and ρ_l is the liquid density), a different power law has been observed as $U_c \propto t^{-7/8}$ from the balance between gravity and viscosity [95]. In the very initial stage of a liquid drop spreading, the fluid inertia, rather than viscosity, balances with the capillary force, thereby showing $U_c \propto t^{-1/2}$.[10]

The contact line dynamics of a solid object entering a liquid-air interface have been studied extensively for a plunging plate [37, 29, 26, 114, 40]. While a vertical plate plunges into a liquid bath, the contact line velocity relative to the plate increases with the plunging speed until it reaches a critical speed. This critical speed has been observed to be proportional to the capillary-viscous velocity [26, 37, 32, 29]. The critical contact line speed is the same

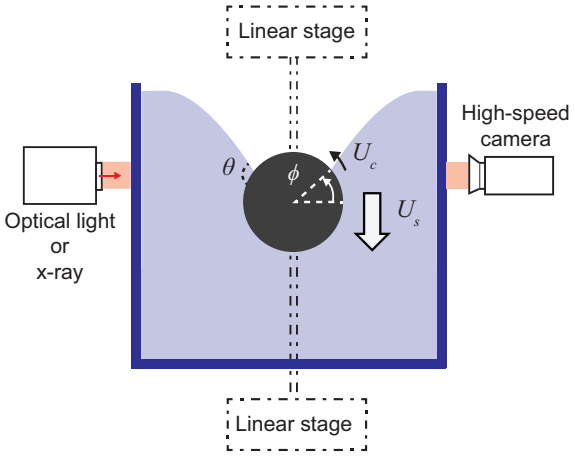

Fig. 2.1 A schematic of the experimental set-up to track the angular location (ϕ) and the dynamic contact angle (θ) of the contact line over time (t) on a solid sphere with diameter of D sinking into the air-liquid interface. The images are recorded by high-speed camera systems using either optical light or x-ray. A sphere descends with a constant falling speed of U_s controlled by a linear stage. The linear stage is tethered to the sphere through a thin rigid rod on the very top or bottom part of the sphere depending on whether the lower or upper part on the sphere is of interest respectively.

as air entrainment velocity as air starts to be dragged by the plate because the contact line cannot keep up with the plunging speed [40, 102].

Force balances on a contact line have been extensively discussed in the context of drop impact [128, 8, 37, 33], which should be valid for the contact line on a sinking sphere. In drop-impact dynamics, the Ohnesorge number ($= \mu/\sqrt{\rho\sigma l}$) and Weber number ($= \rho U^2 l/\sigma$) are non-dimensional numbers to characterize the spreading mechanism, where l and U are the characteristic length and velocity scales, respectively. The Ohnesorge number can be interpreted as the ratio of the inertial time scale ($\sqrt{\rho l^3/\sigma}$) over the viscous time scale ($\rho l^2/\mu$) [128]. Thus, as Oh increases, the dominant resisting force changes from inertia to viscous stress [128, 8]. The dominant driving pressure is known to transition from capillary ($\sim \sigma$) to impact pressure ($\sim \rho_l U^2 l$) as the Weber number (We) increases. However, such a transition in spreading dynamics has not been discussed well for the present problem of contact line motion over a sinking sphere. In the present work, we focus on the capillarity-driven mechanism in a range of small and moderate Weber numbers ($= \rho_l U_s^2 l_c/\sigma$); from 3.8×10^{-7} to 4.4×10^{1}.

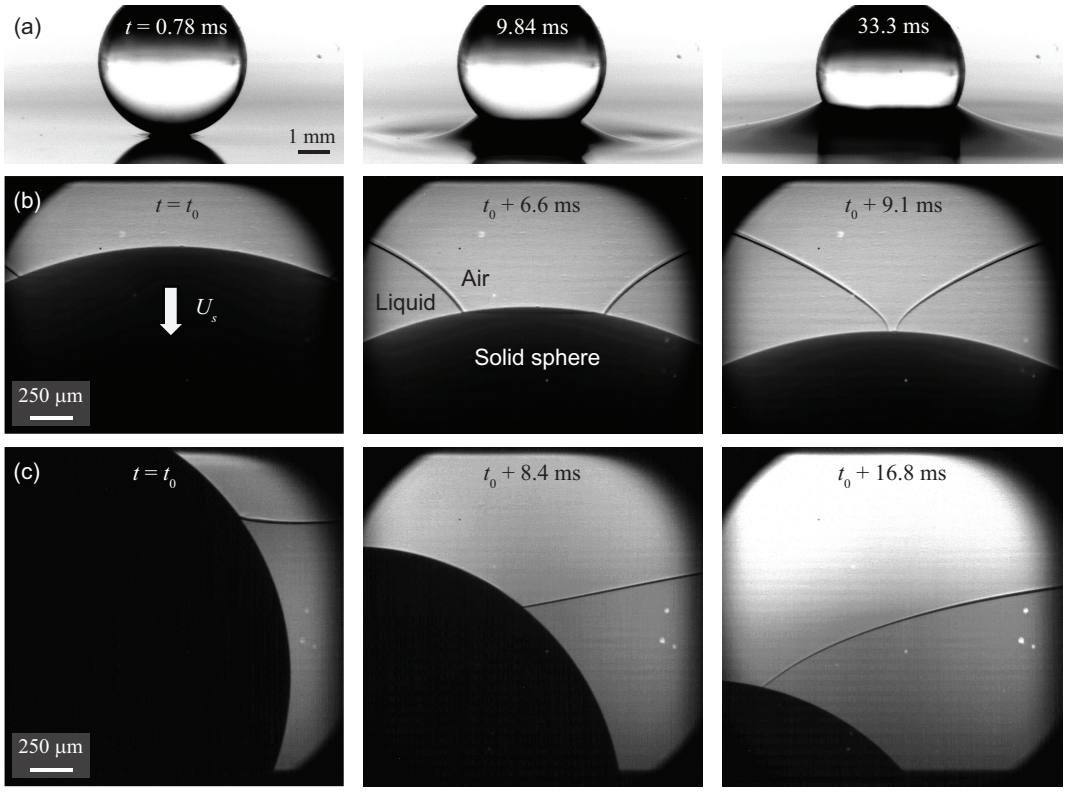

Fig. 2.2 Image sequences recorded with the illumination of (a) optical light and (b-c) x-ray beam. (a) An air-plasma treated glass sphere with a diameter of $D = 4.8$ mm descending into water at a speed of $U_s = 1$ cm/s shows spreading behaviors on the bottom part of the glass sphere. (b) A glass sphere with a diameter of $D = 4.8$ mm descending into ethanol at a speed of $U_s = 5$ cm/s and (c) a steel sphere descending into PDMS 10 cSt with $D = 3.2$ mm and $U_s = 0.1$ m/s.

2.3 Experimental

We designed and performed experiments of a sphere falling at a constant speed, U_s. Either the top or bottom of the sphere was tethered to the linear stage (BiSlide MB10-0150/Velmex, Inc.) as illustrated in Fig. 2.1. For high-speed x-ray imaging, a polychromatic beam with the 1st harmonic energy near 13 keV was used to illuminate the system to resolve the triple contact line (see Fig. 4.1(b-c)). A 100 μm-thick LuAG:Ce scintillator was employed to convert the x-rays to visible light photons, and a high-speed camera (Fastcam SA1.1/Photron Inc.) recorded the images with a frame rate up to 25,000 hz. To avoid overheating of the scintillator by the intense x-ray beam, shutters were used to allow the x-ray to expose to samples for less than 40 ms [48]. However, to observe the overall spreading dynamics as

shown in Fig. 4.1(a), we used optical light illumination. Here, we used a high-speed camera (Fastcam Mini UX100/Photron Inc.) with a frame rate up to 6,400 hz.

We tested four different liquids; [ρ_l (kg/m^3), μ (g/m·s), σ (mN/m)]=[998, 1.0, 73] for water, [762, 1.2, 22] for ethanol, [965, 9.7, 20] for PDMS 10 cSt, and [965, 48.3, 20] for PDMS 50 cSt. Solid spheres with different materials were used: glass, steel, aluminum, and polyoxymethylene (Delrin). Static contact angles for water were measured by the sessile drop method as $\theta_s = 57 \pm 5^\circ$ for glass, $85 \pm 3^\circ$ for steel, $91 \pm 3^\circ$ for aluminum, and $101 \pm 7^\circ$ for Delrin (N=3 for all materials). The values of θ_s from the other liquids are nearly zero as they totally wet the solid surface due to its low σ. We also prepared more hydrophilic glass spheres ($\theta_s = 24 \pm 10^\circ$ for water) by applying air-plasma treatment for 3 min using a plasma cleaner (PE-25/Plasma Etch Inc.). The sphere diameter, D, and the sinking velocity, U_s, varied in the ranges of $0.79 \leq D \leq 9.5$ mm and $3.2 \times 10^{-4} \leq U_s \leq 0.79$ m/s respectively. Detailed experimental conditions are listed in Tables 2.1–2.2. Using Mathematica in-house code, the angular locations (ϕ) of the contact line with respect to the sphere center were tracked over time t. First, the contact line velocity is calculated by differentiating the position data as $U_c = 0.5D(\Delta\phi/\Delta t)$, which represents the velocity in the moving frame. Then, the dynamic contact angles (θ) were measured in the microscale level down to 2 μm/pixel by using the manual tracking module in ImageJ.

2.3.1 Physical and dimensionless parameters

In this section, the physical and dimensionless parameters are tabulated to summarize the experimental range in the present study as in Tables 2.1–2.2.

Table 2.1 Diameter of different spheres.

	Diameter (mm)
Steel	0.8, 1.2, 2.0, 2.8, 3.2, 4.0, 7.9, 9.5
Glass	2.4, 3.2, 4.8, 6.4
Polymer (Delrin)	1.6, 2.3, 3.2, 4.0, 5.5, 9.5
Aluminum	0.8, 2.0, 2.4, 3.2
Glass (air-plasma treated)	2.4, 4.7

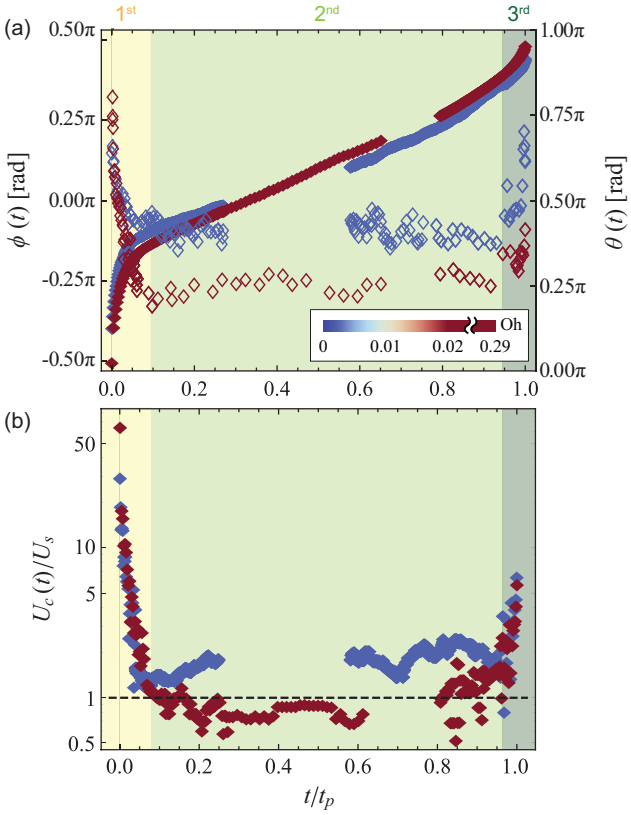

Fig. 2.3 (a) Representative time evolutions of the angular location ϕ (filled diamonds) and the dynamic contact angle θ (open diamonds) of the contact line for two experiments of different Ohnesorge numbers ($\mathrm{Oh} = \mu/\sqrt{\rho_l \sigma l_c}$). Time, t, is normalized by the pinch-off time, t_p. (b) Time evolution of the contact line velocity, U_c, normalized by the sphere sinking velocity, U_s, for two experiments in (a). In the experiment of high Oh ($= 0.28$), a steel sphere with a diameter of $D = 7.9$ mm descends into PDMS 50 cSt at a constant speed of $U_s = 5$ mm/s. For low Oh ($= 2.2 \times 10^{-3}$), a glass sphere of $D = 4.8$ mm treated by air-plasma sinks into water with $U_s = 1$ cm/s. The regions shortly after $t/t_p = 0.25$ in blue and 0.65 in red have missing data due to an overlap between the contact line and the free surface.

Table 2.2 Experimental range of characteristic lengthscale and velocity, and non-dimensional numbers for different liquids.

	Liquids			
	Water	Ethanol	PDMS 10 cSt	PDMS 50 cSt
Capillary length ($l_c = \sqrt{\sigma/(\rho_l g)}$)	2.7 mm	1.7 mm	1.5 mm	1.5 mm
Capillary-inertial velocity ($= \sqrt{\sigma/(\rho_l l_c)}$)	0.16 m/s	0.13 m/s	0.12 m/s	0.12 m/s
Ohnesorge number ($= \mu/\sqrt{\rho_l \sigma l_c}$)	2.2×10^{-3}	7.0×10^{-3}	5.8×10^{-2}	2.8×10^{-1}
Weber number ($= \rho_l U_s^2 l_c/\sigma$)	3.3×10^{-6} -2.3×10^{1}	3.6×10^{-5} -9.6×10^{0}	3.8×10^{-7} -4.0×10^{1}	3.7×10^{-6} -4.4×10^{1}

2.4 Results and Discussion

2.4.1 Three spreading stages

In the experiments, we identified three spreading stages based on kinematic behaviors as shown in Fig. 2.3, where t is normalized by the pinch-off time, t_p. In the first stage, when the contact line position (filled diamonds) is near the bottom of the sphere ($\phi \gtrsim -\pi/2$), the contact line spreads rapidly in the beginning but decelerates soon after. Meanwhile, the dynamic contact angle θ (open diamonds) rapidly decreases and reaches a constant contact angle as the sphere sinks. Then, in the second stage near the equator of the sphere ($\phi \sim 0$), the contact line position changes linearly with t and the dynamic contact angle stays at a terminal value. A similar observation of $\phi \propto t$ was experimentally reported for a sinking cylinder, however the underlying mechanisms were not discussed [147]. In the last stage, just before the pinch-off ($\phi \lesssim \pi/2$), both the speed and the angle of the contact line increase with time. This behavior is primarily driven by the pinch-off dynamics in a cylindrical air cavity above the contact line [72]. The regions shortly after $t/t_p = 0.25$ in blue and 0.65 in red of the Fig. 2.3 have missing data due to an overlap between the contact line and the free surface. Figure 2.3(b) shows the changes in the normalized contact line velocity of two different Oh numbers. The contact line velocity decreases in the first stage, but reaches a terminal speed in the second stage. This terminal velocity is close to the sphere-sinking speed regardless of Oh numbers. A similar trend in the contact line velocity has been observed in a plunging plate [114, 102, 40], in which the contact line slows down to the plunging speed by adjusting the contact angle (see Fig. 2.7) [114].

2.4.2 Capillary-viscous model

As described earlier, a change in the contact line velocity is closely related to a change in the dynamic contact angle, which reveals the characteristics of a capillarity-driven mechanism. The classical Hoffman-de Gennes equation describes the spreading dynamics as a capillary-viscous model in the most of present experimental range of θ [47, 20, 40]. Figure 2.4(a) shows the relation between the instantaneous capillary number, $\mu U_c(t)/\sigma$, and instantaneous contact angle difference, $\theta(t)\left[\theta(t)^2 - \theta_s^2\right]$. All symbols are colored by the Ohnesorge number ($\mathrm{Oh} = \mu/\sqrt{\rho_l \sigma l_c}$), where the capillary length l_c is used as the characteristic length scale[131, 29, 40, 33] rather than the sphere diameter D.

Figure 2.4(a) shows that experiments with high Ohnesorge numbers (red symbols) follow the capillary-viscous model. Here, the capillary-viscous model of $\mathrm{Ca} = 0.013\theta(\theta^2 - \theta_s^2)$

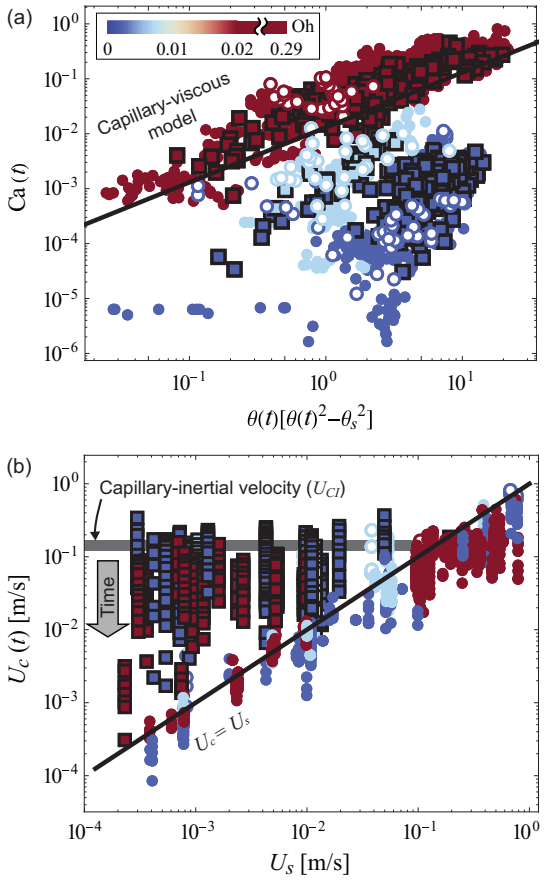

Fig. 2.4 (a) Instantaneous $\mathrm{Ca}(t)(=\mu U_c(t)/\sigma)$ versus instantaneous $\theta(t)[\theta(t)^2-\theta_s^2)]$. Data are colored by Ohnesorge number. The data with higher Oh (red) follow Hoffman-de Gennes equation of $\mathrm{Ca}=0.013\theta(\theta^2-\theta_s^2)$ that is drawn as the black line. Squares with a black edge (■) denote the first stage data, circles (●) the second stage data, and open circles (○) denote the third stage data. (b) Instantaneous U_c versus U_s in the second stage. The black line is that $U_c=U_s$ as the contact line velocity equals to the plunging speed. The gray horizontal stripe indicates a range of the capillary-inertial velocity ($U_{CI}=\sqrt{\sigma/(\rho_l l_c)}$) in the present study. And the big arrow in light gray expresses that U_c decreases with time during the first stage. Data are colored and symboled in the same manner as in (a).

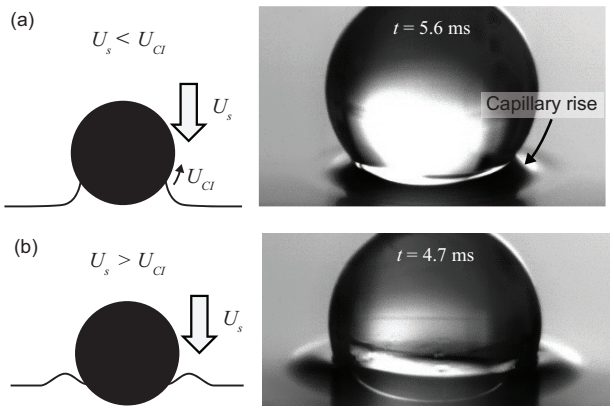

Fig. 2.5 A glass sphere with $D = 4.8$ mm descends into PDMS 10 cSt at a speed of (a) $U_s = 0.1$ and (b) $U_s = 0.3$ m/s. The first stage of capillary rise is observed for a U_s less than the capillary-inertial velocity ($U_{CI} = 0.12$ m/s).

is plotted as a solid line, where the constant prefactor of 0.013 is from Hoffman's previous experiments [68]. The prefactor weakly depends on a spreading geometry and boundary condition logarithmically [131, 149]. This capillary-viscous model is in good agreement with experiments with high Oh (> 0.02) [8]. It is worth noting that Figure 2.4(a) shows high scattering in the data; however, sub-sampled data less than a certain Weber number reduces the scattering (for details, see Figure 2.6). It suggests that data becomes dispersed from a capillary-viscous model due to the effect of impact pressure.

2.4.3 Contact line velocity versus sphere-velocity, and capillary-inertial velocity

Figure 2.4(b) plots the instantaneous $U_c(t)$ versus U_s, where data in the first stage (symbols with a black edge) are clearly separated from data in the second stage (symbols without edge). At the very beginning of the first stage, the contact line is anticipated to move as a balance between capillarity and inertia. This balance predicts a capillary-inertial velocity ($U_{CI} = \sqrt{\sigma/(\rho_l l_c)}$) which is independent of the sinking speed of a sphere. The capillary-inertial velocity is shown as a gray stripe in Fig. 2.4(b); 0.12 – 0.16 m/s depending on different liquids we used (see Table S1 of supplementary material). We observed that data points at the beginning of the first stage started from the capillary-inertial velocity. Similarly, the capillary-inertial velocity was observed only within a short time just after drop impact [10]. When the capillary-inertia rise becomes slower than the falling speed of a sphere as in Fig. 2.5(b), the sphere sinks before the meniscus rises up above the free surface. After this very early stage, the contact line velocity slows down to less than U_{CI} while θ is

decreasing. As shown in Fig. 2.4(a), the contact line velocity with a relatively small Oh is observed to be significantly lower than that predicted in the capillary-viscous model. These data are not governed by simple scaling dynamics as neither inertia nor viscous resistance are negligible. It shares the same conclusion with a previous study, where the capillary and viscous properties were key factors determining flow characteristics near a sinking solid sphere, even on water [37]. Since the driving force spreads both viscous resistance and inertia, the capillary-viscous model would predict a higher contact line speed. A similar force balance has been observed and discussed in the case of drop dynamics [128, 8, 10, 12].

The linear relation of '$U_c \approx U_s$' in the second stage (Fig. 2.4(b)) is discussed with the terminal θ, which indicates that the contact line velocity reaches the plunging speed by the capillary adjustment. As presented in Fig. 2.3(a), the contact angle reaches a terminal value as the second stage begins, similar to the case of a plunging plate [114]. For this second stage, we observed that the contact angle, θ, increases with the plunging speed, U_s (see Figure S2 of supplementary material). Hence, the capillary pressure, $\approx \sigma(\theta^2 - \theta_s^2)$, will increase and further drive the contact line faster [29]. Therefore, increasing contact angle with the plunging speed causes the contact line to spread faster over the sphere. Additionally, it is worth mentioning that the linear relation can be shown in the impact-inertial balance between the inertia ($\sim \rho_l U_c^2$) on the contact line and the impact pressure ($\sim \rho_l U_s^2$) of a sphere as well [128]. Similarly, in the case of a drop impact, the contact line velocity is observed to be the impact speed at high inertia regimes as the drop-impact pressure balances with inertia in the drop [128].

2.4.4 Reduction in data scattering from the capillary-viscous model by cutting off Weber number.

Here, we discuss the data scatteredness from the capillary-viscous model in Fig. 2.6(a). The scatteredness is presumably because the capillary-viscous scaling model of balancing two dominant forces (i.e. capillarity and viscous resistance) is not solely sufficient to explain contact line dynamics over a sinking sphere. Figure 2.6(a) shows the data with high Ohnesorge numbers (> 0.02) along with the capillary-viscous model ($\mathrm{Ca} = 0.013\theta[\theta^2 - \theta_s^2]$), which is colored by the Weber number of a sinking sphere ($\mathrm{We} = \rho_l U_s^2 l_c/\sigma$). Here, the Weber number represents a balance between capillarity (σ) and impact-pressure ($\rho_l U_s^2 l_c$) [128].

Figure 2.6(b) shows the data scatteredness versus maximum cutoff Weber number, where the data scatteredness is estimated by adjusted R^2 values. For example, if the maximum

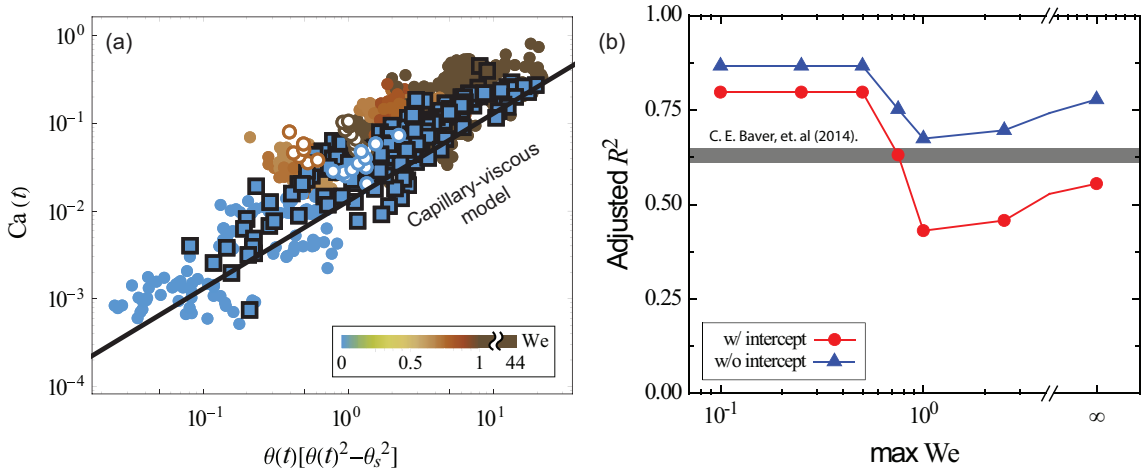

Fig. 2.6 (a) Instantaneous $\mathrm{Ca}(t)(=\mu U_c(t)/\sigma)$ versus instantaneous $\theta(t)[\theta(t)^2-\theta_s^2)]$ for the data with high Ohnesorge number (>0.02). Data are colored by Weber number ($\mathrm{We}=\rho_l U_s^2 l_c/\sigma$). Here, symbols indicate different spreading stages as in Fig. 2.4(a): squares with a black edge (■) denote the first stage data, filled circles (●) denote the second stage data, and open circles (○) denote the third stage data. (b) Data scatteredness is estimated by adjusted R^2 values with varying maximum cutoff We. Adjusted R^2 values are calculated by linearly regressing the data with $y=ax+b$ (with y-intercept) and $y=ax$ (without y-intercept). Each values are estimated by cutting the data with corresponding maximum We. Gray background region indicates the adjusted R^2 range (0.61–0.65) reported in the previous literature[9].

cutoff Weber number is chosen to 1, then we include all the data points with Weber number less than 1 to calculate a adjusted R^2 value. Here, adjusted R^2 values were calculated by linearly regressing experimental data with $y=ax+b$ (with y-intercept) and $y=ax$ (without y-intercept). This linear regression analysis was performed using SPSS (IBM). A stripe with a gray color indicates adjusted R^2 range (0.61–0.65) reported in the previous literature on a liquid spreading in rectangular capillary tubes [9]. We confirm that our adjusted R^2 values (i.e. scatteredness) are comparable with that in the previous literature. Moreover, we found that adjusted R^2 values generally decrease with the maximum cutoff We, which indicates that a simple balance between capillarity and viscous stress is not sufficient to describe the contact-line speed in the current range of Weber number from 3.8×10^{-7} to 44.

2.4.5 Contact angle adjustment by sphere-sinking speed

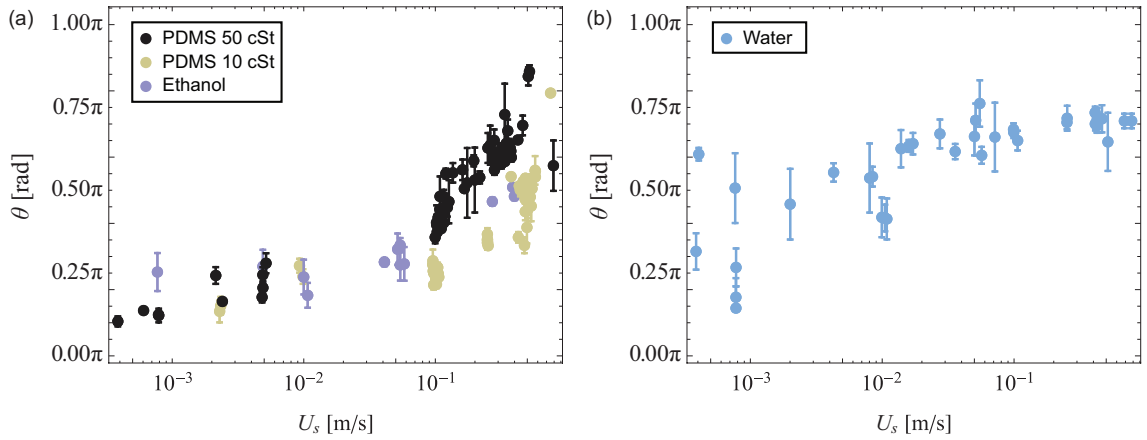

Fig. 2.7 Contact angle variation θ versus the sphere-sinking speed U_s in the second stage for (a) complete wetting liquids of the static $\theta_s \approx 0$ and (b) water of $\theta_s > 0$. Vertical errorbar is estimated as $\sqrt{\delta\theta^2 + \delta\theta_s^2}$ in each experiment.

The contact angle reaches a terminal value as the second stage begins, similar to the case of a plunging plate [114]. In our experiments, the contact angle is observed to increase with the plunging speed of U_s as shown in Fig. 2.7. Such trend is clear regardless of different liquids: both for the complete wetting liquids (Fig. 2.7(a)) and water that partially wets a solid surface (Fig. 2.7(b)). Figure 2.7(a) also presents that the dynamic contact angle of θ approaches $\theta_s \approx 0$ as $U_s \to 0$ because the static contact angle (θ_s) indicates the contact angle when the contact line is not moving, which is close to the advancing contact angle [120]. On the contrary, the case with water has high θ even for small U_s due to hydrophobicity compared to other complete wetting liquids.

2.4.6 Numerical simulation of liquid entry

Numerical simulation is carried out to see the evolution of $p(\phi)$ as a sphere enters a liquid-air interface. In order to do that, Navier-Stokes equation is numerically solved axi-symmetrically in cylindrical coordinates relying on the open-source code named as *Gerris* [117], which discretizes simulation domain based on the finite volume method [126]. In *Gerris*, a liquid-air interface is tracked by the VOF (Volume Of Fluid) scheme [57]. In the present numerical simulation, the system is viewed in the moving reference frame with the constant velocity, U_s, following the sphere. For a slip boundary condition, we employed the method using prewetted liquid layer, which has been acknowledged as an effective method to simulate contact line motion [134, 100, 101, 107]. It is based on two experimental

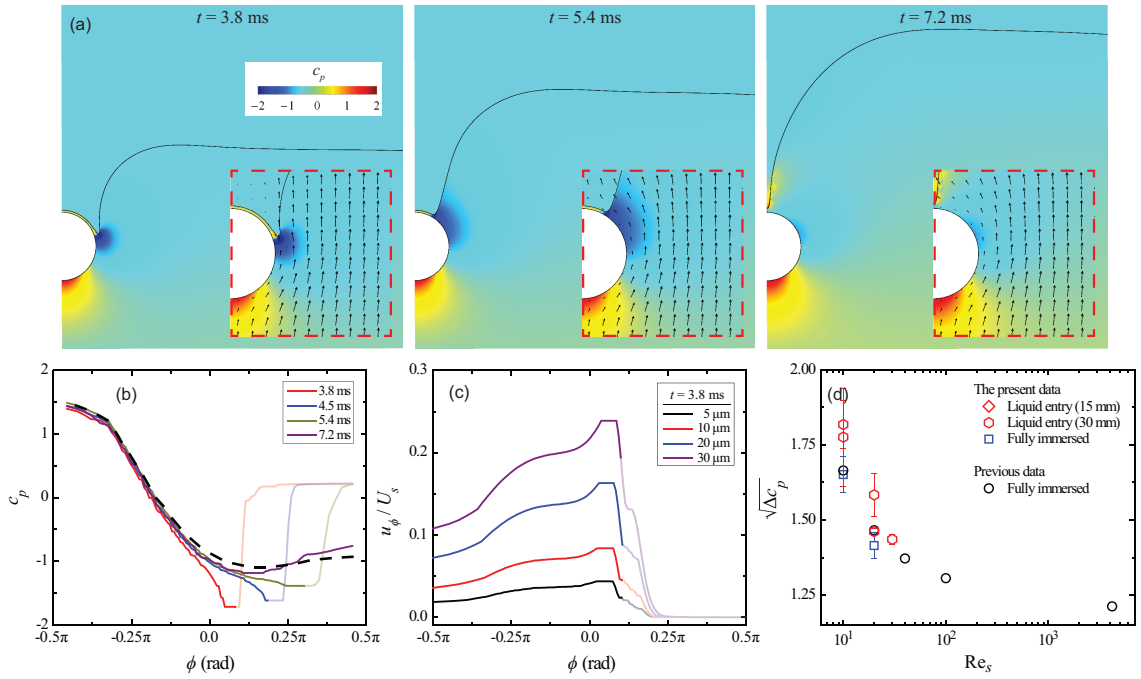

Fig. 2.8 (a-c) The numerical simulation of a sphere of $D = 1$ mm sinking with $U_s = 0.5$ m/s into the interface between PDMS 50 cSt and air, where the prewetted film is employed as slip boundary condition. (a) Time evolution of the pressure coefficient, $c_p = p/(\frac{1}{2}\rho_l U_s^2)$, and velocity (inset) distribution viewed in the moving reference frame following the sphere. The spreading speed of contact line is calculated to be ≈ 0.21 m/s on average. (b) Time evolution of c_p curve versus ϕ at the sphere surface. Black dashed curve is the simulation data of fully immersed case. (c) Normalized polar velocity, u_ϕ/U_s, distribution for different heights from the solid surface at $t = 3.8$ ms. In (b-c), the dim part of the curves indicates the data obtained beyond the contact line location. (d) $\sqrt{\Delta c_p}$ versus Re_s of the present simulation data for the liquid entry using the pre-wetted film thicknesses of 15 and 30 μm and fully immersed cases compared to the previous data for the fully immersed sphere.

backgrounds. First it has the experimental background of the existence of the precursor layer [116]. When a liquid starts to spread on a wettable solid surface, a thin liquid layer called 'precursor layer' is known to proceed faster than the motion of liquid bulk. The other experimental background lies on the finding that the spreading dynamics of a liquid on the surface prewetted by the same liquid is identical with that of the liquid spreading on a dry surface if the prewetted thickness is thin enough compared to the liquid bulk thickness [25]. We have carried out the numerical simulation using the pre-wetted film thicknesses of 15 and 30 μm with applying the no-slip condition. Fig. 2.8(a) shows the time evolution of $c_p(= p/(\frac{1}{2}\rho_l U_s^2))$ and velocity (inset) distribution while the sphere of $D = 1$ mm, which is covered by the pre-wetted film of 30 μm, is sinking with $U_s = 0.5$ m/s toward PDMS 50 cSt, where smallest mesh of 4.9 μm is used. It is found that the highest pressure forms at the stagnation location ($\phi = -0.5\pi$) and the lowest pressure occurs near the contact line or after around the the equator as $\phi > 0$, which is similarly observed in the fully immersed case as stated before. Moreover, the averaged speed of contact line is calculated to be ≈ 0.21 m/s through the entire spreading stages, which shows $U_c/U_s \approx 0.43$. Fig. 2.8(b) plots the time evolution of c_p at the sphere surface, which develops similar to the fully immersed case as t goes. Also, it is noticeable that liquid is found to flow following the direction toward negative pressure gradient as shown in the inset of Fig. 2.8(a). When the normalized polar velocity (u_ϕ/U_s) is plotted for different heights from the solid surface as in Fig. 2.8(c), the velocity is found to accelerate up to the contact line location presumably due to the negative pressure gradient around the sphere. When $\sqrt{\Delta c_p}$ is plotted versus Re_s, $\sqrt{\Delta c_p}$ is calculated to stay as similar value when compared with the previous data in the black circle symbol of the fully immersed case [30, 75, 88] shown in Fig. 2.8(d), where the blue square data indicates the present simulation data for the fully immersed case performed in order to check the validity of *Gerris*, showing the great agreement with the previous fully immersed data [30, 75, 88]. Even though the numerical simulation is not a major stuff in the present report, it gives the idea supporting the hydrodynamics-driven mechanism by revealing the similar pressure distribution with the fully immersed case as well as the acceleration of polar liquid velocity in direction toward the negative pressure gradient. As a future work, it is planned to perform more systematic numerical study with various parameters.

2.5 Supplemental information

2.5.1 Sub-plots for different liquids and solid materials

Figure 2.9 shows Ca-θ plots for different fluids and solids along with the capillary-viscous model. Here, different colors indicate different liquids (PDMS 10 cSt, 50 cSt, Ethanol and Water). Four plots are with different solid materials of (a) steel, (b) glass, (c) polymer, and (d) glass treated by air-plasma. Experiments with glass spheres treated by air-plasma were done only with water because other liquids wet the glass spheres perfectly ($\theta_s \approx 0$) even without the surface treatment. And Fig. 2.10 presents the U_c-U_s relation with different liquids and solids.

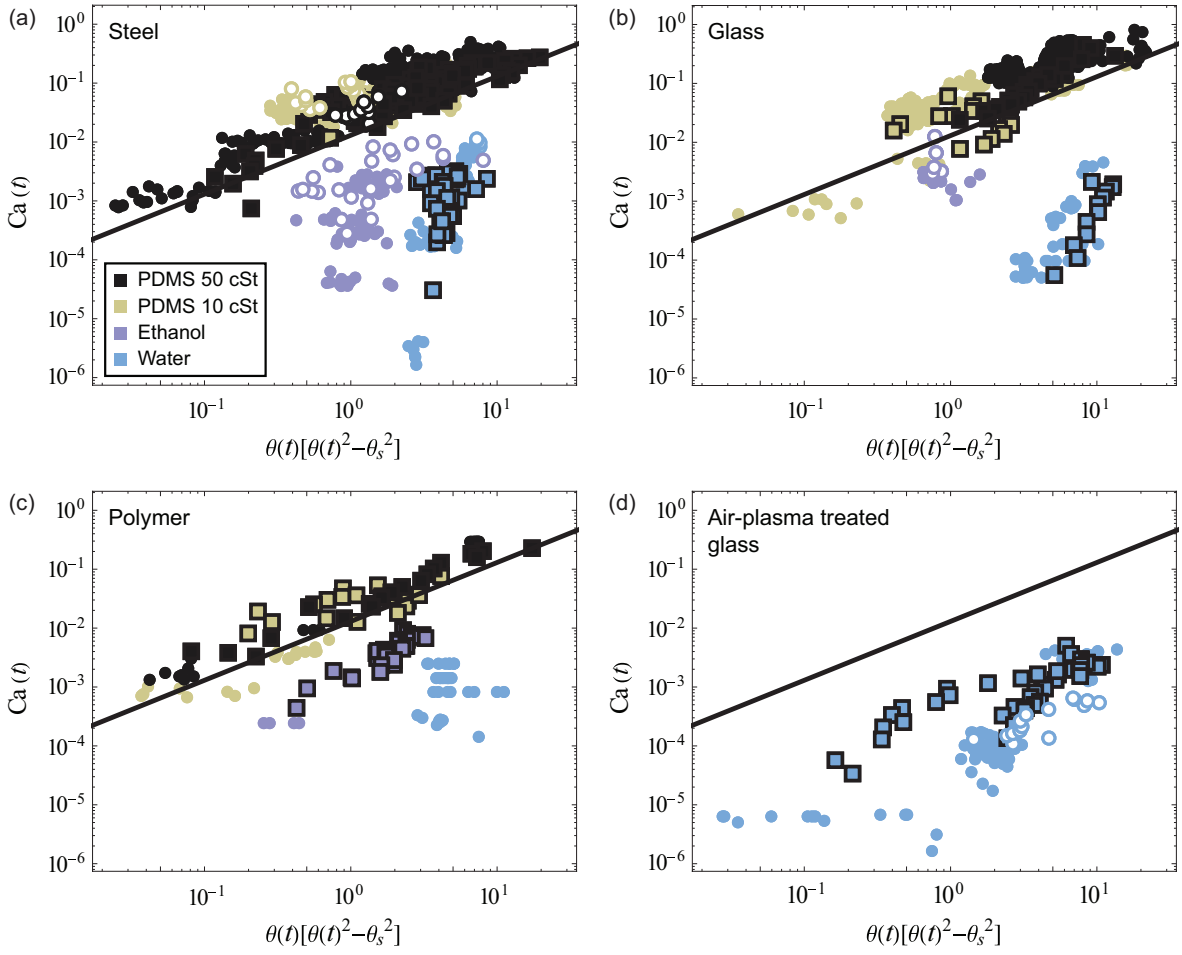

Fig. 2.9 Instantaneous $\mathrm{Ca}(t)(=\mu U_c(t)/\sigma)$ versus instantaneous $\theta(t)[\theta(t)^2-\theta_s^2)]$ for different liquids as the color legend indicates and different solids of (a) steel, (b) glass, (c) polymer, and (d) glass treated by air-plasma. Symbols indicate different spreading stages as explained in Fig. 2.6

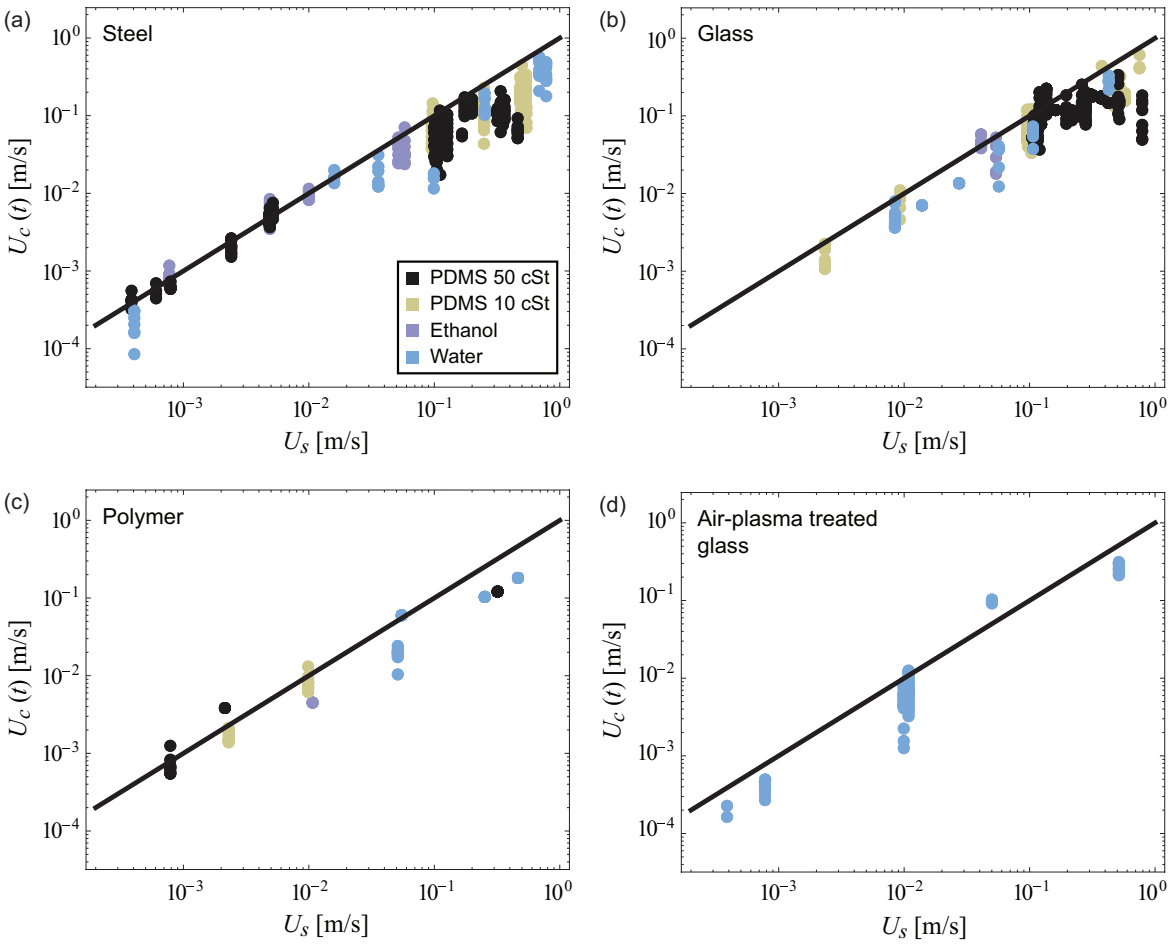

Fig. 2.10 (b) Instantaneous U_c versus U_s in the second stage. The black line is that $U_c = U_s$ as the contact line velocity equals to the plunging speed. Colors indicate different liquids on different solids of (a) steel, (b) glass, (c) polymer, and (d) glass treated by air-plasma.

2.5.2 Capillary-viscous model with Bond number

In the present study, we chose l_c as a characteristic length scale since the contact line dynamics are a local behavior near the triple line [42]. Also, it has been shown that the sphere diameter does not significantly affect the contact line dynamics on a sinking sphere[33]. The relative importance of the sphere diameter over the capillary length can be estimated by Bond number ($= (D/l_c)^2$). Fig. 2.11 is plotted with symbols colored by Bond numbers. However, we does not identify prominent systematic deviations depending on the Bond number. Moreover, it is likely observed that the data with higher Bo numbers scatter less than the data with lower Bo numbers.

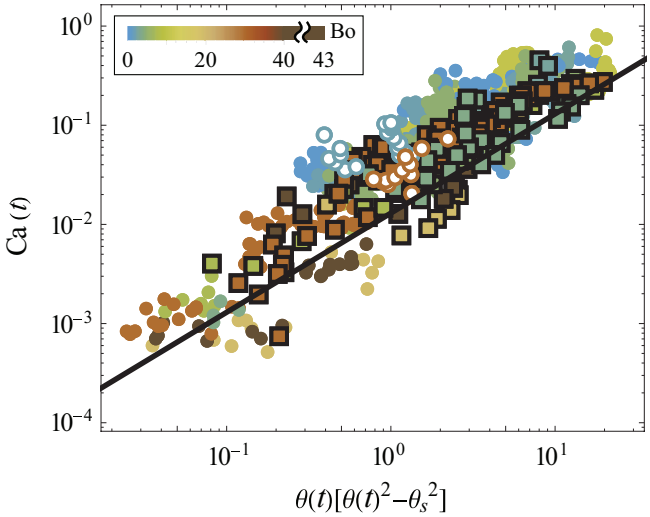

Fig. 2.11 Instantaneous $\mathrm{Ca}(t)(= \mu U_c(t)/\sigma)$ versus instantaneous $\theta(t)[\theta(t)^2 - \theta_s^2)]$ for the data with high Ohnesorge number (> 0.02). Data are colored by Bond number ($= (D/l_c)^2$) and symbols indicate different spreading stages as explained in Fig. 2.6.

2.6 Conclusion

In this study, we investigated the dynamics of the contact line on a sphere as it penetrates through the liquid/air interface. From experiments using optical and x-ray light sources, three distinct spreading stages were identified. In the very beginning, just after the meniscus rises, the capillary-inertial velocity is observed, which is independent of the sphere-velocity. Then, the contact line speed decreases and reaches a terminal velocity. This terminal velocity is set by the plunging speed of the sphere. When the Ohnesorge number is higher than 0.02, the contact line velocity and angle follow the capillary-viscous model as a balance between capillary and viscous stresses. However, with $\mathrm{Oh} < 0.02$, the contact line velocity gets smaller than the velocity predicted in the capillary-viscous model as inertia plays a role.

2.7 Acknowledgement

I would like to thank Dr. S. Gart, Dr. P. Zhang, Dr. J. Boreyko, B. Chang, S. Poulain, Z. Zhang, and A. Deriy for help on the present work. This work was supported from the National Science Foundation (CBET-1336038 & CBET-1604424). This research used resources of the Advanced Photon Source, a U.S. Department of Energy (DOE) Office of Science User Facility operated for the DOE Office of Science by Argonne National Laboratory under Contract No. DE-AC02-06CH11357.

2.8 *Gerris* source code

Solid sphere impacting with constant velocity of 5 m/s with prewetted in 15 μm on PDMS 50 cSt

```
# In the physical unit system of m, s, kg

# One box length (m)
Define DimensionL 5e-3

# Sphere radius (m) and falling velocity (m/s)
Define SphereRadius 5e-4
Define SphereV 0.5

# Setting the resolution
Define LowResol 6
Define HighResol 10
Define HighResolInterface 8
Define MoreResol 0.0
Define CFLCondition 0.1

# Precursor layer thickness (m)
Define PrecursorThick 15.0e-6

# SphereLocations (m)
Define SphereVertLocation 1.0e-3
Define SphereHoriLocation 0.0

# Setting the location of interface (m)
# 0 <=InterfacialDeviation<= 0.30, at 0.25, first contact with the interface.
Define InterfacialDeviation 6.0e-4

# Densities (kg/m^3)
Define Rho_l 965
Define Rho_a 1.2255
```

```
# Viscosities (kg/m·s)
Define Viscosity_l 0.04825
Define Viscosity_a 1.85e-5

# Surface tension coefficient (kg/s^2)
Define Sigma 0.02

# Max time step (s)
Define TimeStepMax 5.0e-5

# How frequenty export the outputs
Define OutputPerNumber 500
Define GfsOutputPerNumber 1000
Define TotalOutputPerNumber 10

# Setting related to movie
Define MovieStep 5.0e-5
Define MovieQuality 10

# Defining the function of VAR to export the viscosity and density as a function of T.
# For VAR, CLAMP function is used to make sure T being in the range of 0 and 1.
Define VAR(T,min,max) ((min-max)*(CLAMP(T,0.,1.)-1.0)/(0.0-1.0)+max)
Define Rho(T) VAR(T,Rho_a,Rho_l)
Define Mu(T) VAR(T,Viscosity_a,Viscosity_l)

#————————————————————————————————————————

2 1 GfsAxi GfsBox GfsGEdge {} {

Time { end = 8.0e-2 dtmax = TimeStepMax }
Solid (ellipse (SphereVertLocation, 0., SphereRadius, SphereRadius))
SurfaceBc U Dirichlet 0
SurfaceBc V Dirichlet 0
```

```
# Generating interface
VariableTracerVOFHeight T
VariableFiltered TF T 1

# Setting surface tension
VariableCurvature K T
SourceTension T Sigma K

# Below (surface position functions) in the parenthesis should be the same
InitFraction T ({if (x < (SphereVertLocation+InterfacialDeviation))
return (SphereRadius+PrecursorThick)*(SphereRadius+PrecursorThick)-(x-SphereVertLocation)
(x-SphereVertLocation)-y*y;
return x-SphereVertLocation-InterfacialDeviation;})

#InitFraction T (x-SphereVertLocation-InterfacialDeviation)
RefineSurface { return HighResolInterface; } (x-SphereVertLocation-InterfacialDeviation)

#————————————————————————————————————————

# Initial refinement
RefineSolid HighResol

# Adapting function
AdaptVorticity { istep = 1 } { maxlevel = HighResol minlevel = LowResol cmax = 1e-2
cfactor = 8 }
AdaptGradient { istep = 1 } { maxlevel = HighResolInterface minlevel = LowResol cmax =
1e-6 cfactor = 8 } T

# Setting viscosity, densities, and box length
SourceViscosity Mu(TF)
PhysicalParams {
L = DimensionL
alpha = (1./Rho(TF))
}
```

```
# Removing small droplets and bubbles
RemoveDroplets { istep = 1 } T 200 (1-T) 1 # Remove small bubbles
RemoveDroplets { istep = 1 } T 200 # Remove small droplets

# Setting gravity
Source {} U 9.81

# Setting accuracy of the calculation
GfsAdvectionParams { cfl = CFLCondition }
ApproxProjectionParams { tolerance = 1e-7 }
ProjectionParams { tolerance = 1e-7 }

# Displaying the simulation sequence by time
OutputTime { istep = 10 } stderr

# Calculating the following variables for each designated step
Init { istep = OutputPerNumber } {
dUdx = dx("U")
dUdy = dy("U")
dVdx = dx("V")
dVdy = dy("V")
ViscousDissipation = (Mu(TF) * ( 2*(dVdy*dVdy+dUdx*dUdx) + (dVdx+dUdy)
(dVdx+dUdy) ))
d2Udx2 = dx2("U")
d2Udy2 = dy2("U")
d2Vdx2 = dx2("V")
d2Vdy2 = dy2("V")
ViscousLaplacianU = 0
ViscousLaplacianV = 0
DensityCheck = Rho(TF)
ViscosityCheck = Mu(TF)
UinMovingFrame = U + SphereV
VelocitySquareinMovingFrame = (U + SphereV)*(U + SphereV)+V*V
}
```

```
# Calculating the following variables between the designated step
Init { start = 0 } {
DimensionOfL = DimensionL
RealSphereRadius = SphereRadius
SphereFallingSpeed = SphereV
SphereCenterXPosition = 0.
SphereCenterYPosition = SphereVertLocation
LiquidViscosity = Viscosity_l
AirViscosity = Viscosity_a
LiquidDensity = Rho_l
AirDensity = Rho_a
SurfaceTensionCoefficient = Sigma
}

# Exporting initial setting
OutputSimulation { start = 0 } StartConfiguration-Refine-HighResol-CFL-CFLCondition.gfs
OutputSimulation { start = 0 } StartConfiguration-Refine-HighResol-CFL-CFLCondition.txt
{ format = text }

# Exporting gfs files
OutputSimulation { istart = GfsOutputPerNumber istep = GfsOutputPerNumber } GfsOutput-
Refine-HighResol-CFL-CFLCondition-%ld.gfs

# Exporting main outputs
OutputSimulation { istart = OutputPerNumber istep = OutputPerNumber } SimuOutput-
Refine-HighResol-CFL-CFLCondition-%ld.txt { format = text variables = P,U,V,T,dUdx,dUdy
,dVdx,dVdy,ViscousDissipation,d2Udx2,d2Udy2,d2Vdx2,d2Vdy2,ViscousLaplacianU,ViscousLaplacianV
}

OutputLocation { istep = TotalOutputPerNumber } LocaOutput-%ld.txt LocationZRTheta100.txt
OutputLocation { istep = TotalOutputPerNumber } LocaOutputSpecified_2.5MicroMeter-
%ld.txt LocationZRThetaBySpecifiedThick100_2.5MicroMeter.txt
OutputLocation { istep = TotalOutputPerNumber } LocaOutputSpecified_5MicroMeter-
%ld.txt LocationZRThetaBySpecifiedThick100_5MicroMeter.txt
OutputLocation { istep = TotalOutputPerNumber } LocaOutputSpecified_7.5MicroMeter-
```

```
%ld.txt LocationZRThetaBySpecifiedThick100_7.5MicroMeter.txt
OutputLocation { istep = TotalOutputPerNumber } LocaOutputSpecified_10MicroMeter-
%ld.txt LocationZRThetaBySpecifiedThick100_10MicroMeter.txt
OutputLocation { istep = TotalOutputPerNumber } LocaOutputSpecified_12.5MicroMeter-
%ld.txt LocationZRThetaBySpecifiedThick100_12.5MicroMeter.txt
OutputLocation { istep = TotalOutputPerNumber } LocaOutputSpecified_15MicroMeter-
%ld.txt LocationZRThetaBySpecifiedThick100_15MicroMeter.txt
OutputLocation { istep = TotalOutputPerNumber } LocaOutputSpecified_17.5MicroMeter-
%ld.txt LocationZRThetaBySpecifiedThick100_17.5MicroMeter.txt

# Making movies
OutputPPM { step = MovieStep } { ppm2mpeg > vort.mpg } {
min = -10*SphereV max = 10*SphereV v = Vorticity maxlevel = MovieQuality }
OutputPPM { step = MovieStep } { ppm2mpeg > velo.mpg } { min = 0 max = 1.5*SphereV
v = Velocity maxlevel = MovieQuality }
OutputPPM { step = MovieStep } { ppm2mpeg > Interface.mpg } {
min = 0 max = 1 v = T maxlevel = MovieQuality }
}
# Boundary conditions
#1
GfsBox {
right = Boundary { BcDirichlet U (-SphereV)
BcNeumann V 0}
top = Boundary { BcDirichlet U (-SphereV)
BcDirichlet V 0}
bottom = Boundary { BcNeumann U 0
BcDirichlet V 0}
}
#2
GfsBox {
left = Boundary { BcDirichlet U (-SphereV)
BcNeumann V 0}
top = Boundary { BcDirichlet U (-SphereV)
BcDirichlet V 0}
bottom = Boundary { BcNeumann U 0
```

```
BcDirichlet V 0}
}
1 2 left
```

Chapter 3

Dynamic criteria of plankton jumping out of water

3.1 Abstract

In nature, jumping out of water is a behavior commonly observed in aquatic species to either escape from predators or hunt prey. However, not all aquatic species are capable of jumping out, especially small organisms whose length scales are comparable to the capillary length (~ 2.7 mm for water). Some aquatic animals smaller than the capillary length are able to jump out while others are not, as observed in some marine copepods. To understand the dynamics of jumping out of the water-air interface, we perform physical experiments by shooting a spherical particle toward the liquid-air interface from below. Experimental results show that the particle either penetrates or bounces back from the interface, depending on the particle and fluid properties, and the impact velocity. The transition from bouncing to penetration regimes, which is theoretically predicted based on a particle force balance, is in good agreement with both physical experiments and plankton behavioral data.

Related article

S. J. Kim, J. Hasanyan, B. J. Gemmell, S. Lee, and S. Jung, “Dynamic criteria of plankton jumping out of water," *J. R. Soc. Interface* **12**, 20150582 (2015).

3.2 Introduction

A number of aquatic species across a broad range of taxonomic groups can be commonly observed 'jumping' through the water surface for different hypothetical reasons.[27, 16] For example, salmonid fish leap out of the river occasionally when they encounter obstacles during upstream spawning migrations. [84] Humpback whales (*Megaptera novaeangliae*), spinner dolphins (*Stenella longirostris*), and gulf sturgeons (*Acipenser oxyrinchus desotoi*) also jump out of the water presumably in order to communicate within the group by creating sounds at the moment of impact. [135, 64, 99] Some other aquatic species break through the water surface to evade predators or to capture prey.[27, 110] Some predators, such as dolphinfish (*Coryphaena*) and arowana (*Osteoglossum bicirrhosum*) jump to catch prey above the surface of the water.[110, 97] On the other hand, jumping prey take advantage of the fact that predators can lose visual contact and are thus unable to predict the re-entry position due to light refraction across the water-air interface.[27]

The aforementioned examples of aquatic species have relatively large characteristic length scales varying from several centimeters to several meters. In contrast to these large animals, a few planktonic species (i.e. copepods) less than three millimeters in length have been observed to successfully jump to avoid predatory fish. [53] The primary benefit of jumping is a reduced drag force in air relative to water. Lower drag allows plankton to temporarily achieve greater velocities and cover longer distances.[53] This is important to minimize the chance of remaining in the predator's perceptive field upon re-entry into the water. Unlike larger animals whose inertia and gravity are large enough to neglect the surface tension, plankton need to overcome the surface tension of water-air interface to break through.[53] While detailed observations of this behavior have been made, the question of whether observed escape speeds alone are sufficient to break the surface remains unresolved. 0 Surface tension force is proportional to the characteristic body length (l), while gravity is proportional to its volume ($\sim l^3$). The capillary length is defined as the resultant lengthscale from balancing these two forces ($l_c = \sqrt{\sigma/(\rho_l g)} \sim 2.7$ mm). Here, ρ_l and σ are the density and the surface tension coefficient of water, respectively. For animals larger than l_c, gravity is the only important barrier that must be overcome in order to make an aerial jump.[7] However, for smaller organisms like plankton with $l \leq l_c$, the surface tension force becomes a critical factor in breaking the water surface. To overcome the surface tension force, animals should generate high enough jumping speeds or inertia. For example, *Labidocera aestiva* with $l \sim 3$ mm is able to jump out of the water with high speeds, ~ 1 m/s, whereas *Daphnia magna* having similar size cannot break the water surface when moving at low speeds, ~ 0.1 m/s

(see electronic supplementary material, movie S1). Despite a number of studies describing animals interacting with and breaking through the water-air interface, the underlying fluid mechanics needs to be better resolved to rationalize the dynamical and critical behavior between jumping and non-jumping plankton.

Moreover, even though the present study is motivated by biological questions, the dynamics of a particle penetrating a fluid interface shares a common framework with multiphase separation processes present in the oil industry.[4] For example, a technique called 'flotation' employs air bubbles to extract oil or valuable ores from oil shale or raw minerals [4, 3, 138]. A underlying mechanism in the flotation processes is interaction and subsequent attachment of a particle on either a liquid-liquid or a liquid-air interface, which share similar physical ingredients with the present study.[127]

In this present study, we investigate the minimum inertia required for an object to jump out of water against gravity and surface tension. First, we have designed and performed physical experiments of shooting spherical particles toward the liquid surface to mimic planktonic copepods jumping as described in Section B.2. In Section 3.4.1, we have developed a simple theoretical model using a force balance that describes the instant at which the particle impacts the interface. This model allows us to estimate the critical impact velocity in Section 3.4.2. Section 3.4.2 shows that dynamic criteria from our model are in good agreement with the particle shooting experiments as well as the existing plankton jumping data. The summary and future direction are included in Section 3.5.

3.3 Material and Methods

3.3.1 Materials

Physical experiments have been executed using spherical particles to represent plankton as depicted in Fig. 3.1(*c*-*e*). We use three different types of particles, purchased from McMaster-Carr, consisting of polymer, steel, and tungsten, with densities, ρ_s, of 1336, 7935, and 19250 kg/m^3, respectively. The sphere diameters, (D), are 1.6, 2.0, 2.1, 2.2, 2.4, 2.8, 3.2, 3.6, 4.0, 4.8, 5.6, and 6.4 mm. Furthermore, two different liquids, distilled water and ethanol, are used to study the effect of liquid-air surface tension, σ, of 0.073 and 0.022 N/m, respectively.

The jumping plankton of *L. aestiva* and the non-jumping plankton of *D. magna*, *P. salina*, and *A. tonsa* are also used in the experiments. Data for *L. aestiva*[53] and *A. tonsa*[18] are re-collected from the published papers. *D. magna* and *P. salina* have been obtained from

Carolina Biological and AlgaGen L.L.C. respectively, and their behaviors are recorded in the laboratory using a high-speed camera (MotionXtra N3/Integrated Design Tools, Inc.) at a frame rate up to 500 Hz. For the plankton data, the diameter scale of D is estimated as the mean value of major and minor lengths of the elliptic body, and the body density is approximated to the density of seawater, $\rho_l = 1027$ kg/m^3, and the surface tension of air-seawater is given by $\sigma = 0.075$ N/m.[53, 83]

3.3.2 Experimental set-up and method

To shoot the particles, a spring system is designed, a schematic of which is shown in Fig. 3.1(b). Another set of experiments has been performed to quantify surface deformations. In the latter experiments, a linear stage (BiSlide MB10-0150/Velmex, Inc.) is used to move the particles with constant speed as shown in Fig. 3.2(a). In our experiments, the impact velocity, V_{im}, on the liquid-air interface is controlled to be in the range of $0.074-1.8$ m/s by adjusting the compressed length of the spring or the input of the linear stage. Corresponding Reynolds number of $\mathrm{Re} = \rho_l V_{im} D/\mu$ ranges from 240 to 4950 in the experiment and the impact angle of α is controlled up to 36° by tilting the spring shooter and the liquid tank. As each particle is set in motion, the position (y) of the particle and the deformation of the liquid-air interface are recorded with a high-speed camera at a frame rate up to 3000 Hz. Then, the position of a particle and the interfacial deformation are tracked and estimated with an in-house Mathematica code. Fig. 3.1(c-d) shows the representative image sequences of shooting experiments with $\alpha = 0°$ for (c) the penetration case, in which the particle exhibits the '*jumping-out*' behavior, and (d) the bouncing case, which is representative of '*non-jumping*' plankton. Fig. 3.1(e) shows the penetration case of steel particle with $D = 2.8$ mm and $V_{im} = 0.49$ m/s impacting the water-air interface with $\alpha = 36°$. For the biological experiments, in order to stimulate a plankton to jump out of water, a photic startle response has been performed by a rapid change in light intensity.[18]

3.4 Results

3.4.1 Governing equation of motion

A particle impacting a liquid-air interface can be described by the following equation of motion along the vertical direction as a function of its vertical position, y,

$$[m_s + m_a]\, a(y) = [m_l - m_s]\, g + F_s(y) + F_d(y)\,, \tag{3.1}$$

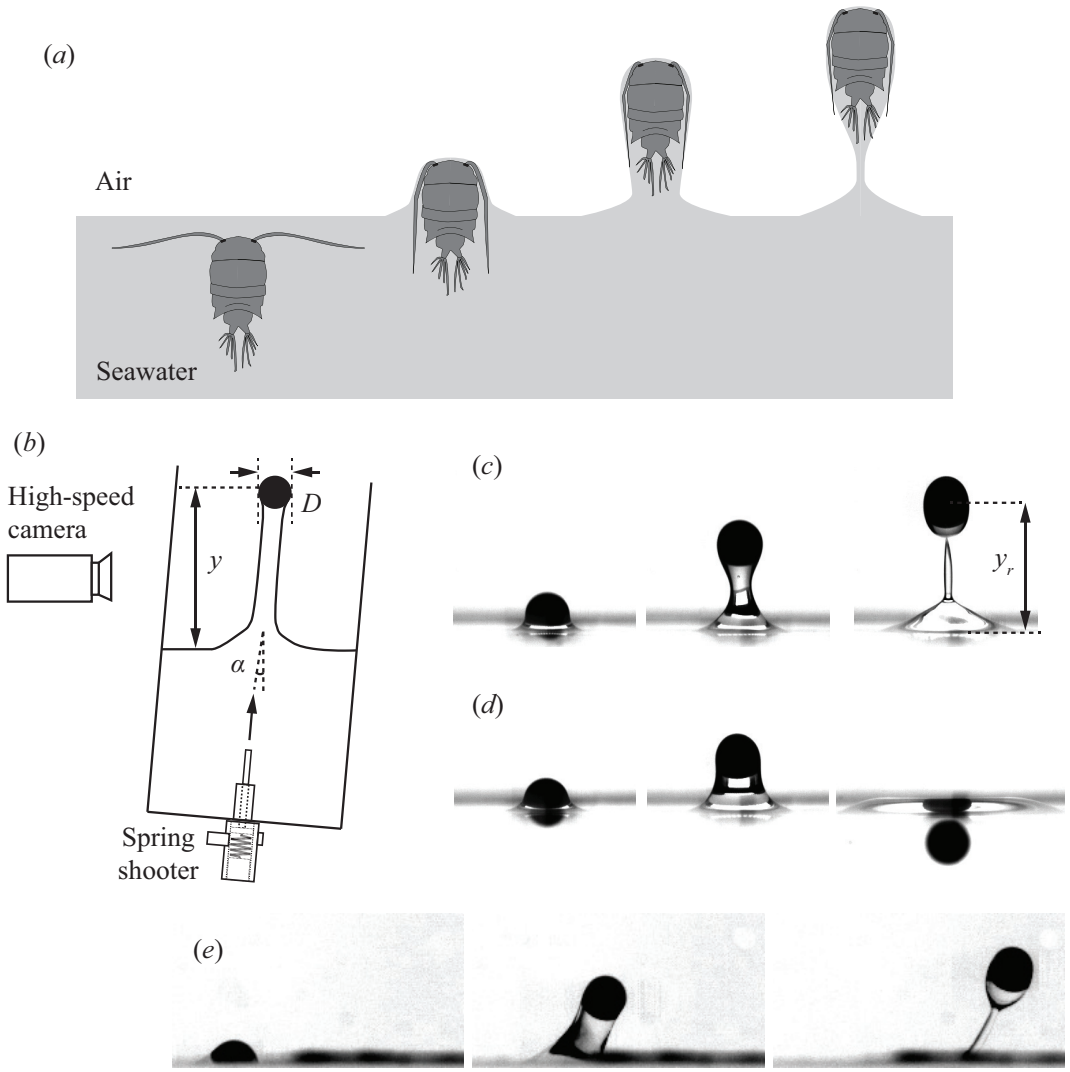

Fig. 3.1 (*a*) Schematic of a plankton jumping out of seawater (*b*) Schematic of physical experiments. (*c-d*) Sequential experimental images of shooting experiments of the polymer sphere with $D = 2.4$ mm impacting the water-air interface with $\alpha = 0^\circ$ which show qualitatively different behaviors of (*c*) penetration through the interface when $V_{im} = 0.77$ m/s and (*d*) bouncing-off when $V_{im} = 0.60$ m/s. (see electronic supplementary material, movie S1). (*e*) The penetration of a steel sphere with $D = 2.8$ mm, $\alpha = 36^\circ$ and $V_{im} = 0.49$ m/s.

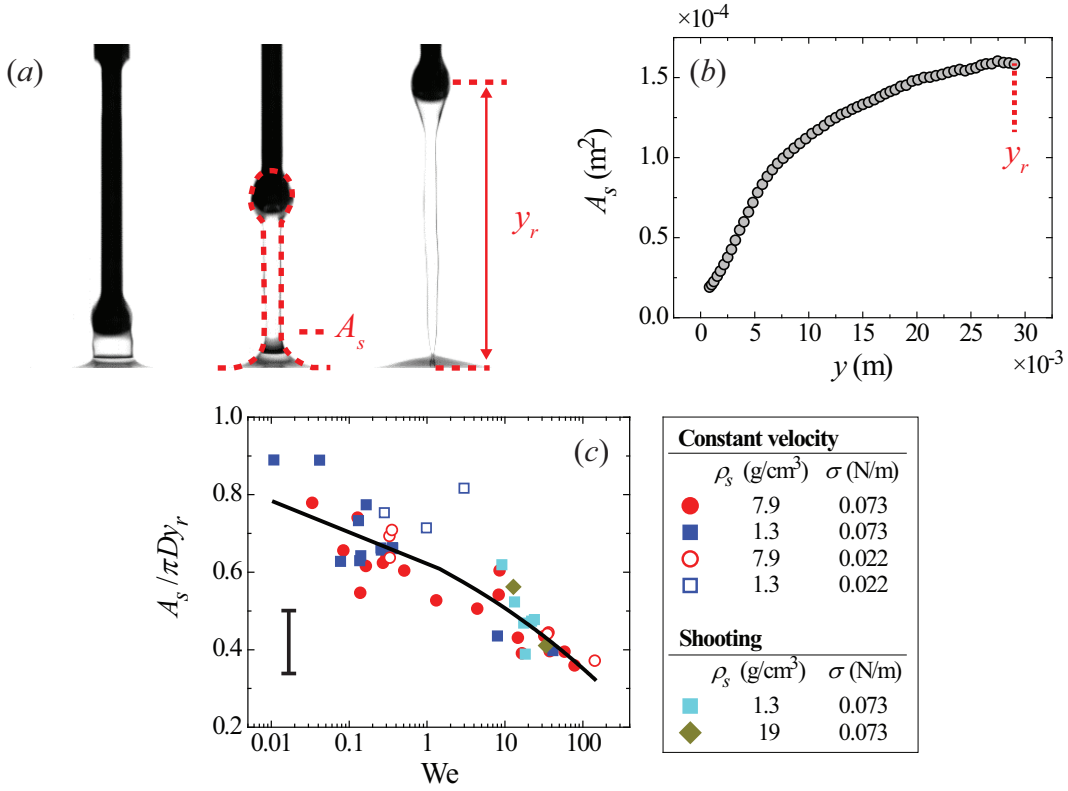

Fig. 3.2 Linear stage experiment pulling up the attached particle with constant speed. (*a*) Experimental images, where red dotted line in the middle image indicates the interfacial area of A_s and y_r in the right image is the rupturing position. (*b*) The typical spatial evolution of surface deformation up to y_r, where the steel particle of $D = 4.0$ mm impacts the water-air interface with $V_{im} = 1.0$ m/s. (*c*) Normalized surface deformation rate as the function of single dimensionless variable of We. The characteristic errorbar is estimated based on experimental errors due to optical distortions near the free surface.

where m_s is the particle mass, m_l is the liquid mass displaced by the particle, and a is the particle acceleration. Forcing terms consist of the surface tension force, F_s, and the drag force acting on the particle, F_d. The added mass effect arises when the surrounding fluid is accelerated as a consequence of the acceleration of the solid particle. In this study, the added mass for spherical particle, m_a, is assumed to be given as $m_a = 0.5\,m_l$, which has been previously used in fully immersed cases.[86] It should be noted that m_a is presumably a decreasing function of time, t, due to the combined effects of the interface and gravity. However, despite its dependency on t, the leading order estimate of $m_a = 0.5\,m_l$ does not appear to affect the overall result analogous to the water entry problem.[5]

The surface tension force, F_s, resists the deformation of the liquid-air interface. Note that the apparent contact line on the particle is *not* observed in the present experiments.

Therefore, we cannot use the uncompensated Young's force to calculate the surface tension force, as it has been done in examples of falling particles with a manifest liquid-air interface.[87] Moreover, compared to the similar examples of water-entry problem which has been analytically solved by virtue of the radial flow approximation with well-posed boundary conditions,[5, 36] the present water-exit system is hard to analytically estimate the liquid column deformation entrained by a sphere due to an unknown boundary condition at the bottom of the column. Therefore, we attempt to estimate F_s based on the gradient in surface energy, namely $F_s = -dE_s/dy = -\sigma dA_s/dy$, where E_s is the surface energy and A_s is the liquid-air interfacial area. A_s is calculated by assuming that the deformed interface is axis-symmetric along the vertical axis. The liquid-air area is expressed as $A_s(y) = 2\pi \int_0^y r\sqrt{1+(dr/d\zeta)^2}d\zeta + \frac{1}{2}\pi D^2$, where r and ζ are the radial and vertical coordinates of the interface, respectively. Figure 3.2(b) shows the plot A_s as a function of y, to illustrate the typical evolution of an deforming interface during impact; its slope ($\partial A_s/\partial y$), is the direct measure of F_s when multiplied by σ. It is observed that, for small y, A_s increases quadratically with y, as a similar behavior has been observed in the deformation of a soap film impacted by a liquid droplet.[54] However, as the particle moves up further ($y \gtrsim 2D$ as in Fig. 3.2(b)), the non-linear behavior of A_s takes place presumably due to the liquid column drainage, resulting in a decreasing value of $\partial A_s/\partial y$.

To simplify the problem, we average the gradient of interfacial area up to the rupturing position, y_r, as $\Delta A_s/y_r \equiv [\int_0^{y_r}(\partial A_s/\partial y)dy]/y_r$, which leads to $F_s \approx -\sigma \Delta A_s/y_r$. Then, based on the dimensionless analysis with constant speed, $\Delta A_s/\pi D y_r$ can be correlated to two dimensionless parameters from the five experimental parameters ρ_l, σ, V_{im},D, and g. The first is the Weber number, $\mathrm{We} = \rho_l V_{im}^2 D/\sigma$, and the second is the Froude number, $\mathrm{Fr} = V_{im}/\sqrt{gD}$. The Weber number quantifies the relative magnitude of inertia over surface tension while Froude number represents the relative magnitude of inertia over gravity. In our experiments, the range of particle size (1.6 – 6.4 mm) is chosen to be on the same order of magnitude as zooplankton (0.78 – 3.3 mm). This small range of particle size around the capillary length ($D \sim l_c$) yields $\mathrm{We} \sim \mathrm{Fr}^2$ due to the lack of size dependency. Therefore, we may eliminate one of the two dimensionless parameters and use only We as the primary dimensionless variable in the analysis to follow. Then, we can empirically find the mean interfacial deformation rate ($\Delta A_s/y_r$) as a function of We, after normalizing by πD:

$$\frac{1}{\pi D}\left(\frac{\Delta A_s}{y_r}\right) = 1 - k_{s1}\mathrm{We}^{k_{s2}}, \tag{3.2}$$

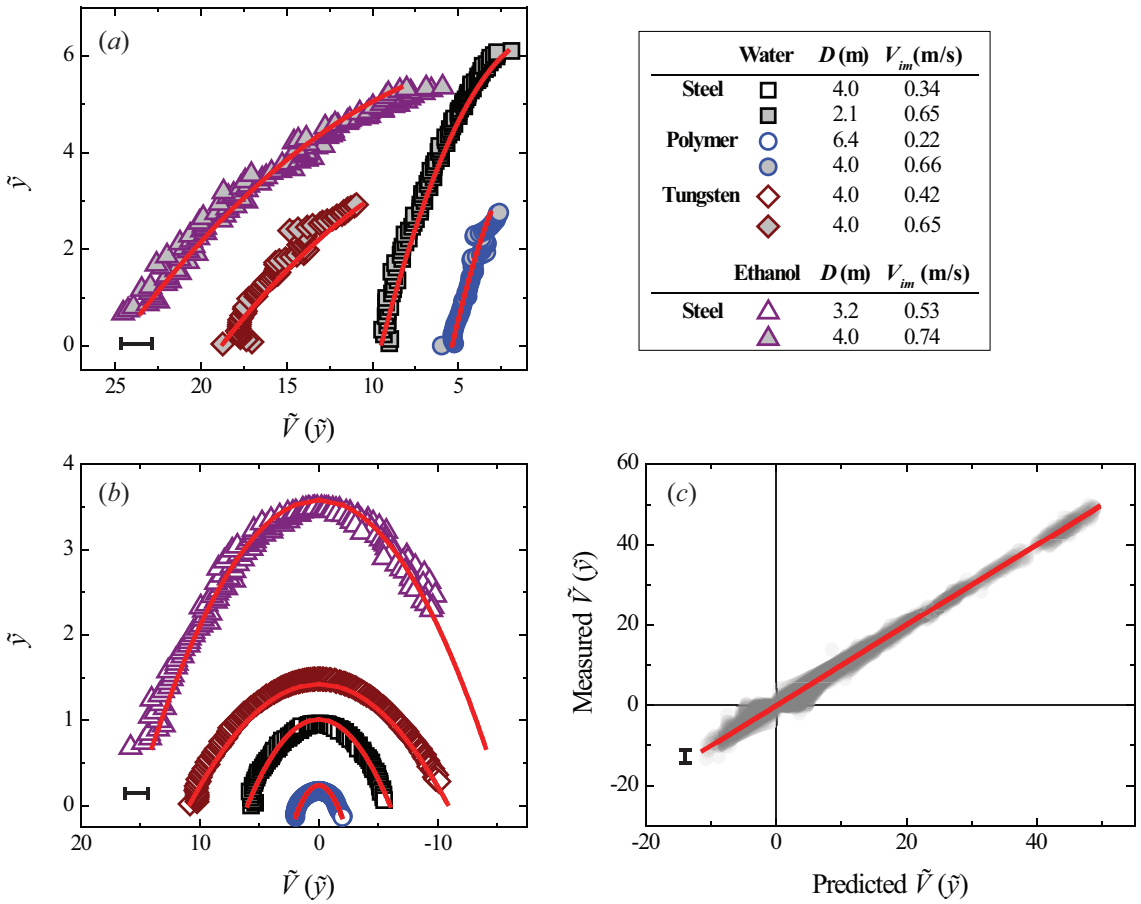

Fig. 3.3 (*a-b*) Plots of representative eight cases; (*a*) four penetration cases and (*b*) four bouncing-off cases in terms of the vertical position ($\tilde{y}$) and the vertical speed $\tilde{V}(\tilde{y})$. Symbols were experimentally measured values. Red curves indicates the theoretical predictions based on Eq. (3.5). (*c*) Comparison of experimentally measured $\tilde{V}(\tilde{y})$ and predicted $\tilde{V}(\tilde{y})$ by Eq. (3.5) over 102 different experiments. The red straight line indicates the perfect matching with the prediction. The characteristic errorbars are estimated based on experimental errors due to optical distortions near the free surface.

where k_{s1} and k_{s2} are determined to be 0.38 and 0.12 respectively from the best fit in Fig. 3.2(c). The empirical relation above states that the surface tension force increases with D and inversely with the Weber number. As We increases, the second term in Eq. (3.2) captures the gradual reduction of the column diameter with an increase of We due to the gravitational and capillary drainage. The scatter in Fig. 3.2(c) is attributed to experimental errors in estimating A_s due to optical distortions near the free surface, especially in the small Weber number limit.

In addition to the interfacial resistance from above, the surrounding fluid near the particle provides a drag force, F_d. In general, drag force is estimated using the empirical relation, $F_d = 0.5\rho V^2 C_d A_c$, where C_d is the drag coefficient and A_c is the projected cross-sectional area normal to the direction of motion. Our present situation is further complicated by the fact that the particle is impacting the liquid-air interface. In this study, the drag is assumed to be $F_d \approx 0.5\rho_a V^2 C_d A$, where ρ_a is the air density. The experimental results in the next section will show the validation of this drag assumption. Then, according to characteristic experimental parameters, F_d is estimated to be at least two orders of magnitudes smaller than the other resistances and is, hence, neglected.

Therefore, Eq. (3.1) can be rewritten as

$$\left(m_s + \frac{1}{2}m_l\right) a(y) = -\left(m_s - m_l\right) g - \left(1 - k_{s1}\mathrm{We}^{k_{s2}}\right)\pi D\sigma. \tag{3.3}$$

This equation will be non-dimensionalized with $\tilde{y} = y/D$ and $\tilde{t} = t/\sqrt{(\rho_s + 0.5\rho_l)D^3/\sigma}$, where the tilde indicates the dimensionless quantity. With $\tilde{a}(\tilde{y}) = \tilde{V}(\tilde{y})d\tilde{V}(\tilde{y})/d\tilde{y}$ based on the chain rule, Eq. (3.3) becomes a simple first-order differential equation for the solid velocity, $\tilde{V}(\tilde{y})$:

$$\frac{1}{6}\tilde{V}\frac{d\tilde{V}}{d\tilde{y}} = -\frac{1}{6}\mathrm{Bo} - \left(1 - k_{s1}\mathrm{We}^{k_{s2}}\right), \tag{3.4}$$

where Bond number, $\mathrm{Bo} = (\rho_s - \rho_l)gD^2/\sigma$, represents the ratio of gravity over surface tension force. By noting $\tilde{V}d\tilde{V}/d\tilde{y} = 0.5d(\tilde{V}^2)/d\tilde{y}$, Eq. (3.4) states that the spatial rate of change in the kinetic energy of a particle is given by the change in the gravitational and capillary potential energies. Eq. (3.4) with the initial condition, $\tilde{V}|_{\tilde{y}=-0.5} = \tilde{V}_{im}$ yields the following solution;

$$\tilde{V}(\tilde{y}) = \pm\sqrt{\tilde{V}_{im}^2 - K(1 + 2\tilde{y})}, \tag{3.5}$$

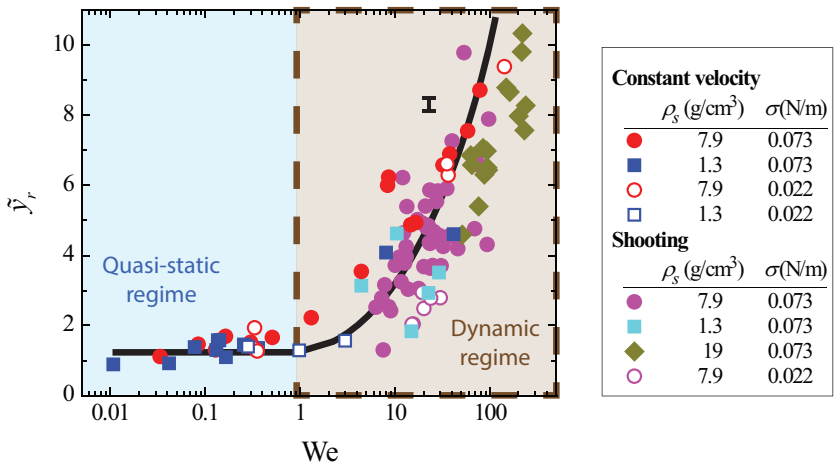

Fig. 3.4 The ruptured position data for shooting and linear stage experiments with constant rise velocity. Two different regimes of quasi-static and dynamic rupture depending on We. The characteristic errorbar is estimated based on experimental errors due to optical distortions near the free surface.

where $K = 6\left(1 - k_{s1}\mathrm{We}^{k_{s2}}\right) + \mathrm{Bo}$. Here, K can be interpreted as the estimate of resistance to the upward motion of the sphere, which decreases with We but increases with Bo. Also, the $\pm$ sign indicates the solutions that describe the velocity of either a rising or falling particle.

The particle shooting experiments have been performed to verify the solution of Eq. (3.5). Figure 3.3(a) shows the plot of the particle position ($\tilde{y}$) versus its corresponding vertical speed ($\tilde{V}(\tilde{y})$) of eight representative cases: four penetration and four bouncing-off cases. Here, the red curves are from the predicted $\tilde{V}(\tilde{y})$ as in Eq. (3.5). All experimental velocities (N=102) are presented with respect to predicted velocities from Eq. (3.5) in Fig. 3.3(b), which shows good agreement. This implies that our assumptions of neglecting drag and using the averaged interfacial area are able to capture the particle dynamics for both penetration and bouncing cases.

3.4.2 Critical impact velocity

Two states of particular interest are penetration (or *jumping-out*) and bouncing-off (or *non-jumping*). Eq. (3.5) is rearranged to estimate the maximum height reached by the particle as

$$\tilde{y}|_{\tilde{V}=0} = \frac{1}{2}\left(\frac{\tilde{V}_{im}^2}{K} - 1\right). \tag{3.6}$$

The penetration regime corresponds to the case in which the rupturing height of the liquid column must be less than the maximum height reached by the particle, thereby yielding

$\tilde{y}_r < \tilde{y}|_{\tilde{V}=0}$. For bouncing-off case, $\tilde{y}_r > \tilde{y}|_{\tilde{V}=0}$. To explicitly express the transition from bouncing-off to penetration, the rupturing height $\tilde{y}_r$ needs to be determined.

To further investigate the rupturing height in different regimes, we experimentally pull up a particle at constant speed using the linear stage: quasi-static regime when We < 1 and dynamic regime when We > 1. Rupture in the quasi-static regime is primarily driven by the capillary force,[91, 155] which shows $y_r \sim D$ and independent of We (see Fig. 3.4(a)).

When We > 1, the rupturing position varies with inertia. To understand $\tilde{y}_r$ in the regime of We > 1, two different time scales are considered: The rising time scale, y_r/V_{im}, and the pinch-off capillary time scale, $\sqrt{\rho_l D^3/\sigma}$.[14] When the two timescales are balanced, the dimensionless rupturing height becomes $y_r/D \sim V_{im}(\rho_l D/\sigma)^{1/2} \sim \mathrm{We}^{1/2}$. Therefore, the rupturing position can be expressed in a simple form with a prefactor, k_r,

$$\tilde{y}_r = k_r \mathrm{We}^{1/2}. \tag{3.7}$$

Experiments with a constant rising velocity yield $k_r = 1.01$, or close to unity, with a moderate adjusted $R^2 = 0.39$. All experiments of penetrating shooting particles belong to the dynamic regime, or We > 1, as shown in Fig. 3.4. The scatter in the particle shooting data might be due to the particle deceleration which is not accounted for in Eq. (3.7).

Combining Eq. (3.7) and Eq. (3.6), the critical impact velocity can be computed by solving

$$\frac{1}{2}\left(\frac{\tilde{V}_c^2}{K} - 1\right) = k_r \mathrm{We}^{1/2}. \tag{3.8}$$

Please note that both K and We are also functions of $\tilde{V}_c$ as $K = 6(1 - k_{s1}\mathrm{We}^{k_{s2}}) + \mathrm{Bo}$ and $\mathrm{We} = V_c^2(\rho_l D/\sigma) = \tilde{V}_c^2[\rho_l/(\rho_s + 0.5\rho_l)]$, with $\tilde{V}_{im} = \tilde{V}_c$ at the critical condition. This allows us to construct a phase diagram that categorizes the penetration (light blue area) and the bouncing-off cases (light red area) of the particle, as well as the jumping plankton (*L. aestiva*) and the non-jumping plankton (*D. magna*, *P. salina*, and *A. tonsa*) as shown in Fig. 3.5(a). Different plankton regions are highlighted by ellipses with different colors (blue for the jumping and red for the non-jumping). The physical data of the plankton is listed in Table 3.1. The phase diagram shows reasonable agreement with the theoretical prediction. Furthermore, the ratio of the impact velocity to the critical velocity is plotted against an impact angle (α) from the vertical axis in Fig. 3.5(b). Experimental results show that our model predicts the transition well regardless of α in the range of $|\alpha| < 36^\circ$. It indicates that the vertical force balance we have developed here is valid, independent of the horizontal force balance.

Eq. (3.8) shows the dependency of $\tilde{V}_c$ on the two dimensionless quantities of DR and Bo, where DR is the density ratio of ρ_l/ρ_s. When DR is fixed as constant, $\tilde{V}_c$ becomes to be dependent on Bo only. For the specific case of DR=0.13 being the case of the steel particle, $\tilde{V}_c$ is plotted as a solid curve in the inset of Fig. 3.5(a). For Bo $\gg$ 1, Eq. (3.8) can be approximated as $\tilde{V}_c \sim \mathrm{Bo}^{1/2}$, which is illustrated as the triangular slope in the inset of Fig. 3.5(a).

Table 3.1 Physical properties of the plankton.

		Lengths (mm)		Velocity (m/s)*
		Major	Minor	
Jumping plankton	*Labidocera aestiva*	1.7 – 4.6	0.62 – 2.0	0.6 – 1.1
Non-jumping plankton	*Daphnia magna*	3.5	1.4	0.071
	Pseudodiaptomus salina	0.87 – 1.1	0.39 – 0.43	0.16 – 0.27
	Acartia tonsa	1.0	0.38	0.50

* It is estimated by the impact velocity for the jumping plankton and by the maximum swimming velocity for the non-jumping plankton.

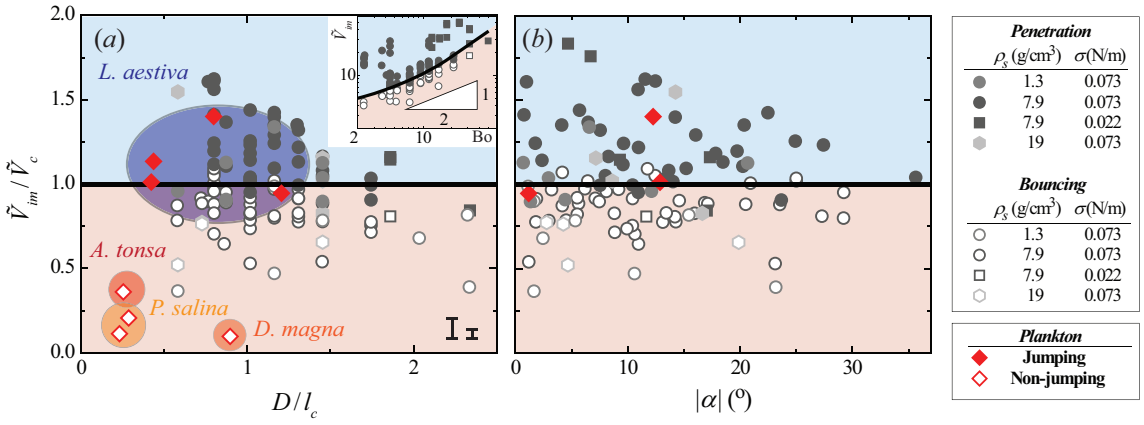

Fig. 3.5 The phase diagram of the penetration case (light blue area) through the interface and bouncing-off case (light red area) from the interface of the particles, as well as the jumping plankton (*L. aestiva*) and the non-jumping plankton (*D. magna*, *P. salina*, and *A. tonsa*), where D is scaled by the capillary length of $l_c = \sqrt{\sigma/(\rho_l g)}$. Different plankton regions are highlighted by ellipses with different colors (blue for the jumping and red for the non-jumping). The inset in (*a*) shows $\tilde{V}_{im}$ versus Bo when $\rho_l/\rho_s = 0.13$ and a solid curve for $\tilde{V}_c$. Two characteristic errorbars for $\tilde{V}_{im}/\tilde{V}_c$ are estimated based on experimental errors due to optical distortions near the free surface (left) and 50 % reduced added mass (right).

3.5 Conclusion

Physical experiments of a particle impacting the liquid-air interface have been performed to elucidate how different physical properties, such as body size and vertical velocity, affect the jumping and non-jumping plankton. The simple model derived from the force balance equation describes the particle trajectories for both penetration and bouncing-off cases. Surface tension plays a crucial role in resisting the particle's penetration by deforming the liquid-air interface. Furthermore, the scaling analysis of the rupturing position has allowed us to acquire an estimate of the critical impact velocity, which categorizes the jumping and the non-jumping plankton. The experimental results based on the shooting particle and the jumping plankton verify our predicted critical velocity ($\tilde{V}_c$) to be a reasonable estimate and provide physical basis for the plankton's minimum impact speed required to jump out of the water.

The results of these experiments may also suggest a plausible explanation as to why neustonic copepods tend to be larger than most other species of copepod. Even if moving at a similar relative speed (0.5 – 0.8 m/s), the results show that a small copepod ($\approx$ 1 mm) will not possess enough kinetic energy to break the surface tension and instead bounce back. This would be highly problematic for copepods living at the surface because not only do they

have pigmentation as protection from UV exposure,[58] which makes them more visually conspicuous to visual fish predators,[13] but escape options are limited as predators approach from below. Thus, while a larger body size may increase visual conspicuousness, it could have been positively selected for the ability to break the surface tension and make an aerial jump.

Additionally, the results suggest that it is unlikely that aerial jumping copepods require special adaptations to their body surface properties in order to make it easier for them to jump out of the water. Without properties such as super-hydrophobicity which is a well-known feature of the integument of water-walking arthropods[17] to increase the contact angle or chemicals produced by the copepods to reduce surface tension, polymer spheres that possess similar size and mass to copepods can break the surface when traveling at comparable speeds to live copepods. Even though the present work is motivated by plankton, the illustrated theoretical model is relevant across multiple disciplines, due to the fundamental interest in the particle-interface interaction and the corresponding potential engineering applications.

3.6 Acknowledgement

This work was supported by the National Science Foundation (PHY-1205642, CBET-1336038) and VT-ICTAS.

Chapter 4

Extremes of pinch-off location and time in liquid column by accelerating solid sphere

4.1 Abstract

When a solid body rises out of a liquid bath, a liquid column is formed and stretched until pinch off occurs at different locations and times. In the present paper, we studied the temporal and spatial evolution of a liquid column extracted by an accelerating sphere out of a liquid bath. For high acceleration compared to gravity, a liquid column is observed to have a shape of an upward-pointing cone, which implies that the column is stretched so quickly that the liquid could not keep up with the solid sphere. This causes the liquid column to pinch off at the upper location. On the other hand, at low accelerations, a liquid column has a uniform column diameter in the middle before pinch-off, and breaks up at the lower location. Also, the pinch-off time is observed to decrease as the acceleration increases. The shift in the pinch-off location and time is a result of the axial velocity-gradient profile in the liquid column. A linear stability analysis predicts the pinch-off time as the inverse of growth rate in the dispersion relation. Additionally, numerical results show that the gradient of axial velocity near the sphere increases when the solid sphere has a higher acceleration. As a result, for high-acceleration cases, the axial velocity-gradient is responsible for necking and pinching off the at the upper location of the liquid column. For cases with low sphere-acceleration, the column pinches off at the lower location by strong Laplace pressure due to a higher gradient of interfacial curvature between the column and bath.

4.2 Introduction

Pinch-off dynamics of a liquid column have been extensively studied due to the interesting underlying mechanics [43, 39, 38] and its relevance to many engineering applications [129, 154, 85, 50]. In 1873, Plateau first observed that a flowing water column, e.g. water running from a tap, became unstable, and the most unstable wavelength is close to three times the initial column diameter [115]. Later, Lord Rayleigh showed that the fastest growing wavelength is predicted by a dispersion relation [122], in which the capillary-inertial wave was considered. Therefore, the pinch-off time (t_p) is observed to be close to the capillary-inertial time scale, $\tau_c = \sqrt{\rho_l L^3/\sigma}$, where ρ_l is the liquid density, L the characteristic length scale (generally the initial diameter of a liquid column), and σ the surface tension. The pinch-off time is known to be approximately τ_c, unless the diameter of a liquid column is more than the so-called capillary length [103], $l_c \equiv \sqrt{\sigma/(\rho_l g)}$, where g is the gravitational acceleration. When $L > l_c$, it pinches off earlier than τ_c because gravity ($\sim \rho_l g$) overwhelms capillarity ($\sim \sigma$). Similarly, when a liquid column is significantly accelerated by a solid object, the pinch-off time is known to depend on the acceleration time scale $\tau_a (= \sqrt{L/a})$ [148, 51, 152]. This time scale was derived from considering the extracted liquid mass $\sim \sigma L/a$ by capillary adhesion, and then this liquid mass was used to replace the inertia scale $\sim \rho_l L^3$ in τ_c [148].

In addition to the pinch-off time, the spatial evolution of a liquid column has drawn much attention due to its applications in transferring a liquid volume to a solid surface, which is called liquid-bridge extension [129, 154, 85]. When a liquid column is held between two solid surfaces with different wettability, the liquid column close to a more wettable surface gets thinner faster than the other side because a larger gradient of interfacial curvature on the wettable side creates more capillary pumping [34, 157]. When both ends have the same wettability, pinch off is more likely to occur on the bottom side as gravity creates larger curvature gradient [157]. Also, a faster extensional speed of the bridge is known to delay the pinch-off behavior[157]. Moreover, when only one end of solid surface moves fast, a liquid column pinches off close to the fast-moving surface [157]. Thus, both capillary pressure and liquid inertia are key factors in determining the pinch-off location of a liquid bridge.

A solid body that exits a liquid into air, hereafter referred to as liquid-exit, also exhibits pinch-off behaviors and plays an important role in natural systems [77, 51, 123] and industrial applications [85, 129]. Interestingly, when dogs and cats drink water, they can control the acceleration of their tongues to be in the range of $1-4g$ [51] and $1-2g$ [123], respectively. While a cat drinks, the pinch-off dynamics of a liquid column are more affected by gravity than the case of dog drinking [123, 51]. From an industrial perspective, an understanding

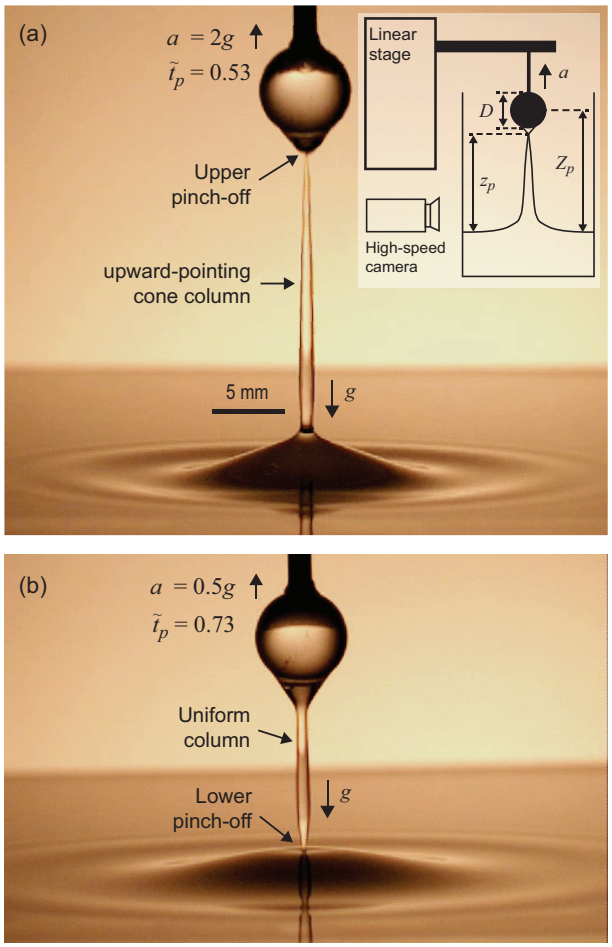

Fig. 4.1 Shapes of a liquid column; (a) an upward-pointing cone column with upper pinch-off and (b) a uniform column diameter in the middle with lower pinch-off. Here, a glass sphere of $D = 6.35$ mm was withdrawn from a water bath with constant acceleration of (a) $a = 2g$ or (b) $0.5g$. The pinch-off time was normalized by the capillary-inertial time scale ($\tau_c = \sqrt{\rho_l D^3/\sigma} = 59.2$ ms); (a) $\tilde{t}_p = t_p/\tau_c = 0.53$ and (b) 0.73. Inset in (a) illustrates the experimental schematic of ascending a solid sphere with constant acceleration that is controlled by the linear stage. z_p is the pinch-off location from free surface and Z_p is the sphere position at the pinch-off moment.

of pinch-off dynamics can give engineers better control over the amount of remnant liquid adhering to a solid body that is withdrawn from a liquid [148]: e.g. the dip-coating process [129].

Despite of the previous studies introduced so far, the picnh-off location and shape of the liquid column remains unclear when a solid body exits water. In this present paper, we studied a liquid column extended by a solid sphere rising with constant acceleration out of a liquid bath. It is found that the pinch-off location significantly depends on the acceleration of the solid sphere as axial velocity distribution changes in the liquid column. Numerical data show that the acceleration of the solid sphere increases the maximum velocity-gradient near the sphere, which contracts the liquid column due to continuity. Moreover, the maximum velocity-gradient is observed to decrease in time, which further yields a scaling relation for the pinch-off time scale.

4.3 Methods

4.3.1 Experiment

The experiment uses a linear stage (BiSlide MB10-0150/Velmex, Inc.) to withdraw a solid sphere out of a liquid bath, as illustrated in the inset of Fig. 4.1(a). A high-speed camera (SC2+/Edgertronic) simultaneously records the images with a frame rate up to 4000 frames per second. In the experiments, we used low-viscosity liquid of water with [ρ_l (kg/m^3), σ (mN/m)]=[998, 73]. The diameter of the glass spheres varies from 2.4 to 6.3 mm. The initial position of the sphere is at the free surface of the liquid, and a constant acceleration is applied on the sphere in the range of 1.4×10^{-2} to 1.5×10^{2} m/s^2. Pinch-off location (z_p) and sphere position (Z_p) at the pinch-off moment are measured from the free surface. The vertical coordinates of z and Z are positive when is above the free surface, otherwise negative. Length and time scales are non-dimensionalized by using the sphere diameter of D and $\tau_c(=\sqrt{\rho_l D^3/\sigma})$ respectively, then the superscript tilde indicates the dimensionless quantity.

4.3.2 Numerical simulation

To better understand how the acceleration of a sphere affects the pinch-off dynamics, the liquid flow for different acceleration is numerically calculated. We performed this numerical simulation by employing the open-source code named *Gerris* [117] that has been widely

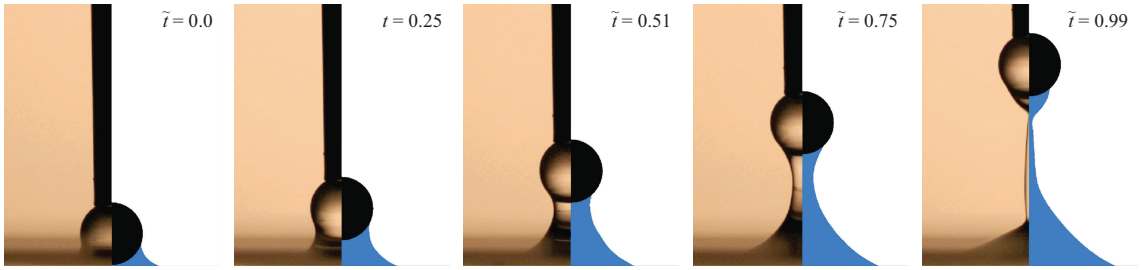

Fig. 4.2 Temporal evolution of the water-air interface while a glass sphere rises up at $a = 2g$. Experimental images and numerical results from *Gerris* are compared side-to-side at different times; $\tilde{t} = 0, 0.25, 0.51, 0.75$, and 0.99.

used among the academic community for effectively simulating interfacial behaviors [118]. In the simulation, the temporal evolution of axial velocity distribution inside a liquid column is investigated with different sphere accelerations. In *Gerris*, the Navier-Stokes equation is solved asymmetrically in cylindrical coordinates by using the volume of fluid method to track the liquid-air interface [67]:

$$\rho \frac{D\underline{u}}{Dt} = -\nabla p + \nabla \cdot \left[\mu(\nabla \underline{u} + \nabla \underline{u}^T)\right] + \sigma \kappa \delta_s \underline{n} + \rho_l \underline{g}, \tag{4.1}$$

where $\underline{u}$ is the fluid velocity vector, p the pressure, κ the interface curvature, δ_s the Dirac delta function of the interface being unity at the location of the interface, $\underline{n}$ the unit normal vector to the interface, and $\underline{g}$ the gravitational acceleration vector. Then, the numerical results of $\underline{u}(t,z)$ and interfacial coordinates are post-processed using an in-house Mathematica code.

The temporal evolution of the interfacial shape is compared between experiments and simulations, as shown in Fig. 4.2. For both experiment and simulation, a sphere of $D = 3.2$ mm rises up with $a = 2g$ out of water. In the simulation of Fig. 4.2, the smallest mesh size of 6.3 μm and the air density of 1.2 kg/m^3 are used. Dimensionless pinch-off time ($\tilde{t_p}$) and location ($z_p/(Z_p - 0.5D)$) are calculated to be 1.04 and 0.89, which are close to the experimental measurements of 1.00 and 0.90, respectively. Here, the pinch-off location is normalized by the distance between the free surface and the bottom of the sphere, so that a value close to unity indicates an upper pinch-off. Otherwise, a normalized pinch-off location that gets close to zero indicates a lower pinch-off.

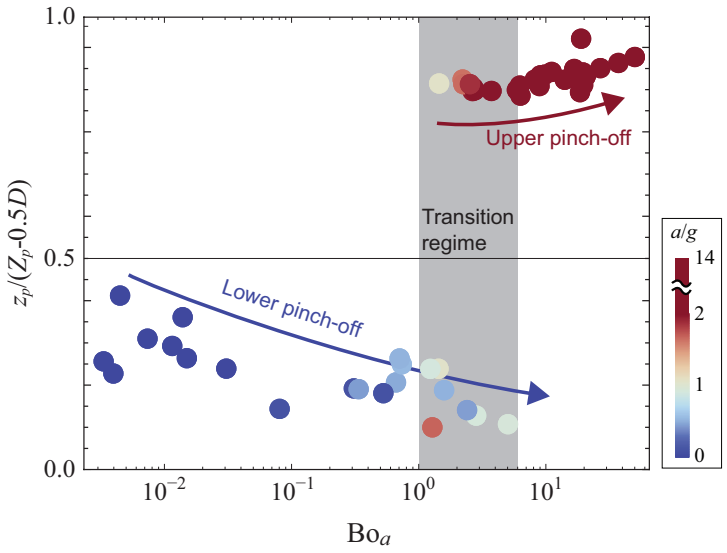

Fig. 4.3 Normalized pinch-off location, $z_p/(Z_p - 0.5D)$, versus the acceleration-based Bond number ($\mathrm{Bo}_a = \rho_l a D^2/\sigma$). The data are colored by the acceleration of a solid sphere normalized by gravitational acceleration (a/g).

4.4 Result and discussion

4.4.1 Column evolution with different sphere-acceleration

Figure 4.1(a–b) show two representative cases of a sphere ($D = 6.35$ mm) being accelerated at $a = 2g$ and $0.5g$, respectively. The pinch-off location is found to dramatically shift from upper (Fig. 4.1a) to lower (Fig. 4.1b) locations. Also, the column shape is close to an upward-pointing cone at a high acceleration (Fig. 4.1(a)), but has a uniform diameter in the middle at a low acceleration (Fig. 4.1(b)). The upward-pointing cone shape implies that the liquid column is stretched, but the liquid cannot keep up with the solid sphere. Therefore, the column likely pinches off closer to the sphere. A similar up-triangular column was also experimentally [123, 51] and numerically [157] observed in previous literature too.

On the other hand, a uniform column is observed when a sphere rises up at low acceleration or almost constant speeds [103]. The fast-moving sphere stretches the liquid column into a thin ligament with a small variation in curvature [103]. In this case, a lower pinch-off location is more likely to occur due to a high curvature gradient, which creates stronger capillary pumping back to the bath. From this point, the lower location is the most probable place to pinch off because a higher curvature gradient is consistently observed near the free surface in the present experiments.

Figure 4.3 shows the pinch-off location versus the acceleration-based Bond number ($\mathrm{Bo}_a = \rho_l a D^2/\sigma$) [148]. Pinch-off near the middle (slightly lower than the middle location) occurs only when a liquid column extends quasi-statically as $\mathrm{Bo}_a \to 0$ [77]. And as Bo_a increases, the pinch-off location moves to a liquid bath. As mentioned before, when acceleration a is lower than g (or $a/g < 1$), the liquid column more likely pinches off in the lower location. Otherwise, pinch-off occurs in the upper location when $a/g > 1$ as shown in Fig. 4.3. It is noticeable that the pinch-off location gradually decreases down to around zero as Bo_a increases when $a/g < 1$. Similarly, for the upper pinch-off cases ($a/g > 1$), the normalized pinch-off location also increases up to unity (close to the sphere) as Bo_a increases. Please note that the gray highlighted region ($1 \lesssim \mathrm{Bo}_a \lesssim 6$) indicates a transition regime, in which both lower and upper pinch-off's co-exist. Interestingly, this regime overlaps with the moment that the sphere-acceleration crosses over the gravitational acceleration (see the colorbar of Fig. 4.3). In this transition regime, the liquid column pinches off at both lower and upper locations almost simultaneously or within a short time interval less than one millisecond. This concurrent pinch-off can be rationalized by the fact that effects of both capillary pumping and column-stretching are on the same order of magnitude as similarly discussed in the previous literature [148].

4.4.2 Temporal evolution of axial velocity in the liquid column

Figure 4.4 presents numerical results of the temporal evolution of axial velocity $\tilde{u}_z(\tilde{t},\tilde{z})$ for different acceleration of $0.5g$ and $2g$. The axial velocity is radially averaged in a liquid column, and the horizontal errorbars indicate standard deviations at each vertical location ($\tilde{z}$). $\tilde{u}_z$ is non-dimensionalized by D and τ as $\tilde{u}_z = u_z/u_c$, where $u_c = \sqrt{\sigma/(\rho_l D)}$ is the capillary-inertial velocity [128]. The radial velocity $\tilde{u}_r$ is observed to be negligible compared to $\tilde{u}_z$ except very early in time. For each time step ($\tilde{t}$), the averaged axial velocity is presented in the range of $0 \le \tilde{z} \le \tilde{Z}(\tilde{t}) - 0.5$, where $\tilde{Z}(\tilde{t}) - 0.5$ is at the bottom of a sphere. In all simulations in Fig. 4.4, solid and fluid conditions are the same as $D = 3$ mm, $\rho_l = 10^3$ kg/m^3, and $\sigma = 0.073$ N/m. An interesting observation is that the velocity gradient $\partial\tilde{u}/\partial\tilde{z}$ near a sphere increases with acceleration. Such a high gradient in the axial velocity escalates the column-necking behavior near a sphere since the radial velocity is proportional to the gradient in the axial velocity as the fluid continuity; $\partial\tilde{r}(\tilde{t},\tilde{z})/\partial\tilde{t} = -0.5\tilde{r}\partial\tilde{u}_z(\tilde{t},\tilde{z})/\partial\tilde{z}$, where $\tilde{r}(\tilde{t},\tilde{z})$ is the column radius. Then, the narrowing column pumps out the liquid towards the sphere due to a pressure gradient induced by a high curvature gradient. Accordingly, the upward suction becomes even faster than the velocity of the sphere, thereby causing the

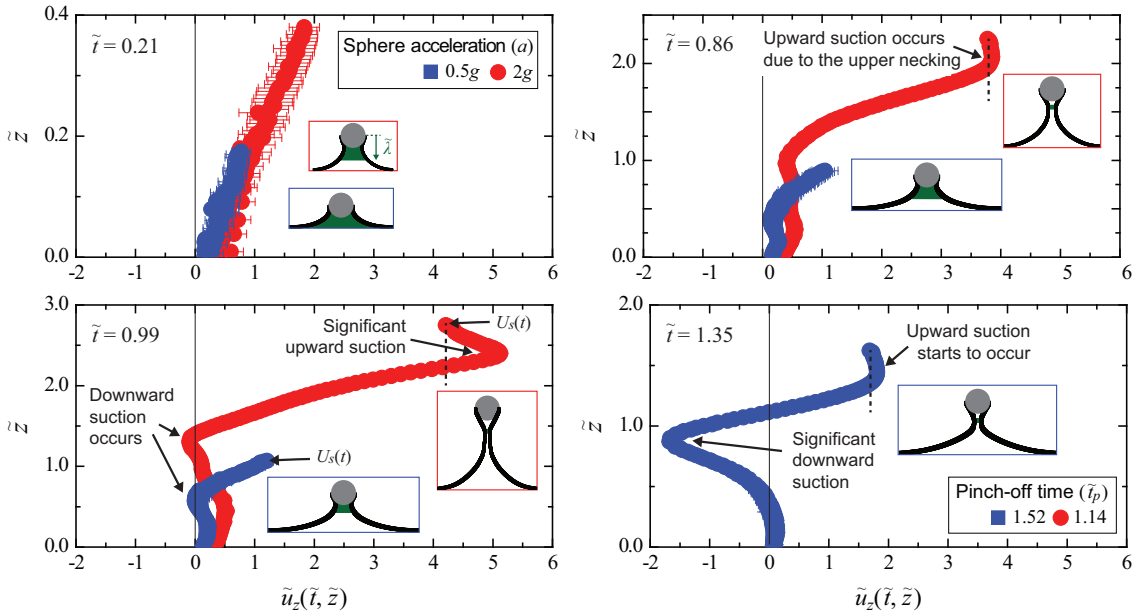

Fig. 4.4 Temporal and spatial evolution of the axial velocity that is radially averaged in a liquid column formed by a solid sphere rising with different acceleration of $0.5g$ (blue) and $2g$ (red). The axial velocity at the highest $\tilde{z}$ equals to the instantaneous velocity of an accelerating sphere $U_s(t)$ as denoted in the subplot at $\tilde{t} = 0.99$. The axial velocity is numerically calculated using the open-source code named *Gerris* [117]. Shapes of a liquid-air interface are presented in the insets with blue and red borders for $a = 0.5g$ and $2g$ respectively. Dark green regions indicate the decaying length defined in 4.4.4. For simulations, initial and boundary conditions are kept same with $D = 3$ mm, $\rho_l = 10^3$ kg/m^3, and $\sigma = 0.073$ N/m except the acceleration of the sphere.

upper pinch-off for higher acceleration. This suction speed increases significantly as the column gets narrower in time. On the other hand, at $\tilde{t} = 0.99$ just before pinch-off, it is noticeable that a downward suction start to develop close to the free surface (see the left-hand side of Fig. 4.4(c)). This downward suction further increases with $\tilde{t}$ (as shown at $\tilde{t} = 1.35$ in the Fig. 4.4). Also, the upward suction near the sphere starts to develop even for the lower acceleration case of $a = 0.5g$, however the time is definitely later compared to that when the downward velocity occurs. The data for $a = 2g$ are not presented at $\tilde{t} = 1.35$ because it pinched off at the early time of $\tilde{t}_p = 1.14$ by the upward suction close to the sphere. The liquid column for $a = 0.5g$ pinched off at a lower location by the downward velocity at $\tilde{t}_p = 1.52$. Here, we conclude that the high velocity-gradient induced by the high acceleration of a sphere causes the upper pinch-off as it yields the upward suction near the sphere faster than the downward velocity near the bath.

4.4.3 Pinch-off time

In this section, we will predict pinch-off time using a linear analysis which characterizes both temporal and spatial changes in the velocity and radius of a liquid column. To simplify the analysis, we assume that the column is axisymmetric over the course of time and the viscous effect is negligible. Then, the one-dimensional governing equations of a liquid column can be written as [41]

$$\rho\left(\frac{\partial u_z}{\partial t}+u_z\frac{\partial u_z}{\partial z}\right)=-\frac{\partial p}{\partial z}-\rho g \tag{4.2}$$

$$\frac{\partial r}{\partial t}=-u_z\frac{\partial r}{\partial z}-\frac{r}{2}\frac{\partial u_z}{\partial z}, \tag{4.3}$$

where the capillary pressure is approximated as $p\simeq\sigma[1/r-\partial^2 r/\partial z^2]$ and $r(z,t)$ is the radius of a liquid column. We assume two normal modes of the axial velocity and radius of the column as $r(z,t)=r_0(1-\varepsilon e^{\omega t+ikz})$ and $u_z(z,t)=u_{z0}(1-\varepsilon e^{\omega t+ikz})$. Here, the first order perturbation is at frequency ω and wavenumber k, r_0 is the initial radius of the liquid column, and $u_{z0}=at$ is the velocity of a sphere. Then, the above equations on the order of ε become $a+\omega(at)+ik(at)^2=(\sigma/\rho)r_0ik(1/r_0^2-k^2)$ and $\omega=-(3/2)\,ik\,(at)$. Finally, we can get a dispersion relation as

$$\omega^2=\frac{9}{2}\left[\frac{\sigma}{\rho r_0^3}(kr_0)^2\left(1-(kr_0)^2\right)+iak\right]. \tag{4.4}$$

This dispersion relation tells us how the temporal frequency, the inverse of time scale, relates to the spatial wavenumber, the inverse of length scale. So, we anticipate that a real part of the frequency, ω_r, should be related to the inverse of the pinch-off time as $\omega_r\simeq 2\pi/t_p$. On the right-hand side, two main terms appear; the first term depends on capillarity and the second one depends on acceleration.

For the cases of high acceleration ($\mathrm{Bo}_a>1$), the unsteady inertia from the acceleration of a sphere is dominant. Experimentally, we observed that the pinch-off happens right below a sphere, which suggests that the pinch-off wavenumber of interest is $k\simeq 2\pi/D$. Then, the predicted pinch-off time becomes $t_p=2\pi[(9\pi/2)(a/D)]^{-1/2}=(2/3)\sqrt{2\pi}\,\sqrt{D/a}$. In a non-dimensional form, $\tilde{t}_p=\sqrt{8\pi/9}\,\mathrm{Bo}_a^{-1/2}$. As shown in Fig. 4.6, non-dimensionalized pinch-off times are found to collapse along the predicted pinch-off time from the linear stability (a red line). Circle and square symbols indicate experimental and numerical data respectively.

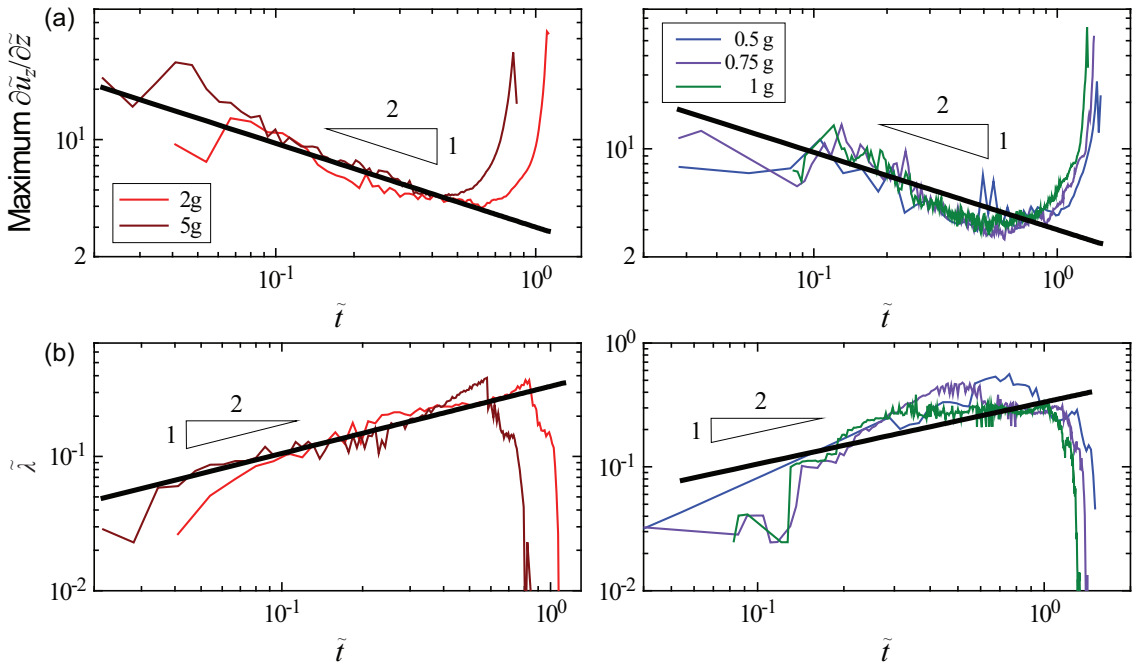

Fig. 4.5 Numerical data on temporal evolution of (a) maximum velocity-gradient and (b) decaying length for high accelerations of $2g$ and $5g$ on the left and low accelerations of $0.5g$, $0.75g$, and $1g$ on the right. Black lines indicate (a) $(\partial\tilde{u}_z/\partial\tilde{z})_{\max} = 3\tilde{t}^{-1/2}$ and (b) $\tilde{\lambda} = (1/3)\tilde{t}^{1/2}$.

4.4.4 Decaying length

Figure 4.5(a) presents the temporal evolution of maximum velocity-gradient $(\partial\tilde{u}_z/\partial\tilde{z})$ near the sphere for high acceleration of $2g$ and $5g$ on the left and low acceleration of $0.5g$, $0.75g$, and $1g$ on the right. The maximum velocity-gradient is calculated as the maximum value of the gradient of an axial velocity along the column, and then is non-dimensionalized by multiplying τ_c. We found that the maximum velocity-gradient decreases over time, following the slope of $-1/2$ in the loglog scale. The maximum velocity-gradient diverges near the pinch-off moment due to the upward suction. Also, as discussed in the previous section 4.4.2, this divergence emerges faster with the acceleration of a sphere. The previous study [35] showed that a decaying length of axial velocity grows as $\tilde{\lambda} \sim \tilde{t}^{1/2}$ for impulsively stretching liquid-column. Also, a self-similar variable as $\tilde{u} = U(\tilde{z}/\tilde{t}^{1/2})$ is known to govern universal pinch-off dynamics very near pinch-off moment [38].

To compare this result of the decay length with numerical simulations, $\tilde{\lambda}$ is estimated to be the distance from the z-location of reaching the maximum velocity of $\tilde{u}_z$ to the lower z-location in which $\tilde{u}_z$ decays by 1. This decay length from simulations is illustrated as a dark green region inside the liquid column in Fig. 4.4. Figure 4.5(b) shows the temporal evolution

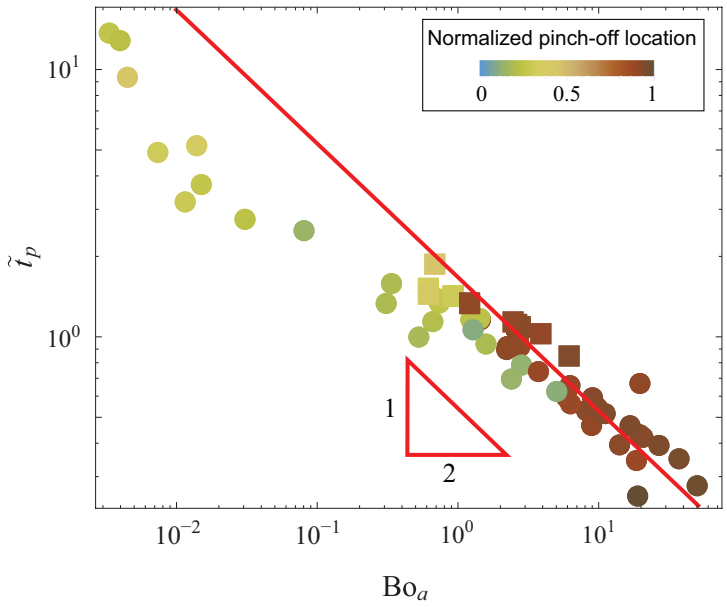

Fig. 4.6 Dimensionless pinch-off time ($\tilde{t}_p$) versus acceleration-based Bond number ($= \rho_l a D^2/\sigma$). Red line indicates the present theory of $\tilde{t}_p = \sqrt{8\pi/9}\mathrm{Bo}_a^{-1/2}$ for high acceleration of a sphere.

of $\tilde{\lambda}$ for high acceleration on the left and low acceleration on the right. We observed that $\tilde{\lambda}$ decays as $\tilde{\lambda} = (1/3)\tilde{t}^{1/2}$ as expected from the self-similar result above. Also, we remark that our measured $\tilde{\lambda}$ is approximately the inverse of maximum $\partial\tilde{u}_z/\partial\tilde{z}$. This trend becomes more clear as the acceleration of a sphere increases from $0.5g$ to $5g$ presumably because the one-dimensional approximation holds well for a slender liquid column generated by a sphere with high acceleration. Even though the values of $\tilde{\lambda}$ are similar for different acceleration, the ratio of $\tilde{\lambda}$ to the liquid column height $\tilde{Z}$ are significantly different as shown in Fig. 4.4. For low acceleration, $\tilde{\lambda}$ covers the entire or most parts of a liquid column, which indicates that the axial velocity decreases slowly along almost the entire column. However, for high acceleration, $\tilde{\lambda}$ just fills in a small portion of the upper part in a liquid column, therefore only the nearby liquid is able to follow a moving sphere in contrast to the case of low acceleration. Accordingly, a liquid volume in the upper part of the column decreases faster for higher acceleration, which causes the column-necking and further upward suction as discussed in the section 4.4.2. Thus, it is anticipated that the upper pinch-off occurs when the decay length is much smaller than the column height; $\tilde{\lambda} \ll \tilde{Z}$. Using the predicted pinch-off time in the previous section ($\tilde{t}_p = \sqrt{8\pi/9}\,\mathrm{Bo}_a^{-1/2}$), then the decay length at the moment of pinch-off will be $\tilde{\lambda} = (1/3)(8\pi/9)^{1/4}\,\mathrm{Bo}_a^{-1/4}$. For the cases of high acceleration ($\mathrm{Bo}_a > 1$), the maximum decay length is $(1/3)(8\pi/9)^{1/4} \simeq 0.43$. It means that no more than a half the diameter is a

characteristic distance in which a liquid column is affected by the acceleration and follows the moving solid. At the pinch-off, the column height is always taller than the decay length. Therefore, we anticipate that the pinch-off occurs close to a moving sphere.

4.5 Conclusion

Pinch-off locations and time are studied for the liquid column stretched by a solid sphere rising with constant acceleration. We found that the pinch-off location is substantially affected by the acceleration of the sphere. Different acceleration alters the profile of the axial velocity in the liquid column. A high velocity-gradient near the sphere creates the upper pinch-off by vertically stretching the nearby liquid column and consequently forming an up-pointing triangle. This velocity-gradient is estimated by the decaying length near the sphere from the numerical data, which shows good agreement with previous literature. On the opposite case of low acceleration, it pinches off at the lower location due to downward capillary suction induced by a Laplace pressure gradient between a high-pressure column and a low-pressure bath. Moreover, a linear stability analysis predicts the pinch-off time as $\tilde{t}_p = \sqrt{8\pi/9}\,\mathrm{Bo}_a^{-1/2}$ for high acceleration, which describes our experimental results quite well.

4.6 *Gerris* source code

Solid sphere of $D = 3$ mm accelerating with a=20m/s^2 out of water

```
# One box length (m)
Define DimensionL 6.1e-3

# Sphere radius (m) and acceleration (m/s^2)
Define SphereRadius 1.5e-3
Define Accel 20

# Setting the resolution
Define LowResol 5
Define HighResol 9
Define HighResolInterface 9
Define MoreResol 2
Define CFLCondition 0.5

# SphereLocations (m)
Define SphereVertLocation 0.0
Define SphereHoriLocation 0.0

# Setting the location of interface (m)
Define InterfacialDeviation 0.0008365125449728153

# Densities (kg/m^3)
Define Rho_l 1e3
Define Rho_a 1.2255

# Viscosities (kg/m·s)
Define Viscosity_l 1.0e-3
Define Viscosity_a 1.85e-5

# Surface tension coefficient (kg/s^2)
Define Sigma 0.073
```

```
# Max time step (s)
Define TimeStepMax 5.0e-5

# How frequenty export the outputs
Define OutputPerNumber 250
Define GfsOutputPerNumber 2000
Define TotalOutputPerNumber 100

# Setting related to movie
Define MovieStep 5.0e-5
Define MovieQuality 9

# Defining the function of VAR to export the viscosity and density as a function of T.

# For VAR, CLAMP function is used to make sure T being in the range of 0 and 1.
Define VAR(T,min,max) ((min-max)*(CLAMP(T,0.,1.)-1.0)/(0.0-1.0)+max)
Define Rho(T) VAR(T,Rho_a,Rho_l)
Define Mu(T) VAR(T,Viscosity_a,Viscosity_l)

#————————————————————————————————————

8 10 GfsAxi GfsBox GfsGEdge {} {

Time { end = 0.5 dtmax = TimeStepMax }
Solid (ellipse (-SphereVertLocation, 0., SphereRadius, SphereRadius))
SurfaceBc U Dirichlet 0
SurfaceBc V Dirichlet 0

# Generating interface
VariableTracerVOFHeight T
VariableFiltered TF T 1

# Setting surface tension
VariableCurvature K T
```

```
SourceTension T Sigma K

# Below (surface position functions) in the parenthesis should be the same
InitFraction T ({if (x < (-SphereVertLocation-InterfacialDeviation))
return (SphereRadius*SphereRadius)-(x+SphereVertLocation)*(x+SphereVertLocation)-y*y;
return x+SphereVertLocation+InterfacialDeviation;})
RefineSurface { return HighResolInterface; } (x+SphereVertLocation+InterfacialDeviation)

#————————————————————————————————————

# Initial refinement
RefineSolid (HighResol+MoreResol)

# Adapting function
AdaptVorticity { istep = 1 } { maxlevel = HighResol minlevel = LowResol cmax = 1e-2
cfactor = 8 }
AdaptGradient { istep = 1 } { maxlevel = HighResolInterface minlevel = LowResol cmax =
1e-6 cfactor = 8 } T

# Setting viscosity, densities, and box length
SourceViscosity Mu(TF)
PhysicalParams {
L = DimensionL
alpha = (1./Rho(TF))
}

# Removing small droplets and bubbles
RemoveDroplets { istep = 1 } T 200 (1-T) 1 # Remove small bubbles
RemoveDroplets { istep = 1 } T 200 # Remove small droplets

# Setting gravity
Source {} U 9.81

# Setting accuracy of the calculation
GfsAdvectionParams { cfl = CFLCondition }
```

```
ApproxProjectionParams { tolerance = 1e-7 }
ProjectionParams { tolerance = 1e-7 }

# Displaying the simulation sequence by time
OutputTime { istep = 10 } stderr

# Calculating the following variables for each designated step
Init { istep = OutputPerNumber } {
dUdx = dx("U")
dUdy = dy("U")
dVdx = dx("V")
dVdy = dy("V")
ViscousDissipation = (Mu(TF) * ( 2*(dVdy*dVdy+dUdx*dUdx) + (dVdx+dUdy)*(dVdx+dUdy)
))
d2Udx2 = dx2("U")
d2Udy2 = dy2("U")
d2Vdx2 = dx2("V")
d2Vdy2 = dy2("V")
ViscousLaplacianU = 0
ViscousLaplacianV = 0
DensityCheck = Rho(TF)
ViscosityCheck = Mu(TF)
UinAbsFrame = U - (Accel*t)
VelocitySquareinMovingFrame = (U - (Accel*t))*(U - (Accel*t))+V*V
}

# Calculating the following variables at start time
Init { start = 0 } {
DimensionOfL = DimensionL
RealSphereRadius = SphereRadius
SphereCenterXPosition = 0.
SphereCenterYPosition = SphereVertLocation
LiquidViscosity = Viscosity_l
AirViscosity = Viscosity_a
LiquidDensity = Rho_l
```

```
AirDensity = Rho_a
SurfaceTensionCoefficient = Sigma
}

# Exporting initial setting
OutputSimulation { start = 0 } StartConfiguration-Refine-HighResol-CFL-CFLCondition.gfs
OutputSimulation { start = 0 } StartConfiguration-Refine-HighResol-CFL-CFLCondition.txt
{ format = text }

# Exporting gfs files
OutputSimulation { istart = GfsOutputPerNumber istep = GfsOutputPerNumber } GfsOutput-
Refine-HighResol-CFL-CFLCondition-%ld.gfs

# Exporting main outputs
OutputSimulation { istart = OutputPerNumber istep = OutputPerNumber } SimuOutput-
Refine-HighResol-CFL-CFLCondition-%ld.txt { format = text variables = P,U,V,T,dUdx,dUdy
,dVdx,dVdy,ViscousDissipation,d2Udx2,d2Udy2,d2Vdx2,d2Vdy2,ViscousLaplacianU,
ViscousLaplacianV }

# Making movies
OutputPPM { step = MovieStep } { ppm2mpeg > Interface.mpg } {
min = 0 max = 1 v = T maxlevel = MovieQuality }
}
# Boundary conditions
# 1
GfsBox { left = Boundary { BcDirichlet U (Accel * t)
BcNeumann V 0}
bottom = Boundary { BcNeumann U 0
BcDirichlet V 0}
}
# 2
GfsBox {
left = Boundary { BcDirichlet U (Accel * t)
BcNeumann V 0}
top = Boundary { BcDirichlet U (Accel * t)
```

```
BcDirichlet V 0}
}
# 3
GfsBox {
bottom = Boundary { BcNeumann U 0
BcDirichlet V 0}
}
# 4
GfsBox {
top = Boundary { BcDirichlet U (Accel * t)
BcDirichlet V 0}
}
# 5
GfsBox {
bottom = Boundary { BcNeumann U 0
BcDirichlet V 0}
}
# 6
GfsBox {
top = Boundary { BcDirichlet U (Accel * t)
BcDirichlet V 0}
}
# 7
GfsBox {
right = Boundary { BcDirichlet U (Accel * t)
BcNeumann V 0}
bottom = Boundary { BcNeumann U 0
BcDirichlet V 0}
}
# 8
GfsBox {
right = Boundary { BcDirichlet U (Accel * t)
BcNeumann V 0}
top = Boundary { BcDirichlet U (Accel * t)
BcDirichlet V 0}
```

```
}
1 2 top
1 3 right
3 4 top
2 4 right
3 5 right
4 6 right
5 6 top
5 7 right
6 8 right
7 8 top
```

Appendix A

Emerging string of fluid pearls

A.1 Abstract

How does a humidifier work? An ultrasonic humidifier makes our room humid by emitting mist through a cavitation process generated by a submerged piezoelectric transducer. When the humidifier is turned on, a rising fluid column appears and forms a string of fluid pearls as shown in Fig. A.1(a). A similar phenomenon has been first reported by Rozenberg in 1973 [125]. Clear visualizations of the fluid-pearl shape are captured in high resolution by the digital single-lens reflex camera (D810, Nikon Corp.) as shown in Fig. A.1(a,b,c). The periodic fluid fountain in drop-chain shape with ~ 1 mm wavelength is formed due to the pressure wave, which is generated by ultrasonic vibration of 2.8 MHz of piezoelectric transducer. The experimental setup is schematically shown in the inset of Fig. A.1(a). As the fluid decelerates due to gravity, it accumulates at the apex of the fluid column as in Fig. A.1(b). While continuing to form a fluid fountain, the cavitation process emits clouds of very fine droplets as in Fig. A.1(c), which makes air humid. Time evolution of the same experiment is also recorded using the high-speed camera (Fastcam Mini 800K-M, Photron Inc.) at 10,000 fps. Fig. A.1(d) shows the sequential images from the moment that a fluid hill first forms at $t = t_0$, and then as a fountain of water pearls develops, and further accumulates on the top.

Related article

S. J. Kim, M. Jang, S. H. Um, and S. Jung, “Emerging string of fluid pearls," *Phys. Rev. Fluids* **1**, 050502 (2016).

A.2 Technical background on cavitation

The research on cavitation traditionally departed from the effort to reduce deleterious effects by the cavitation such as performance breakdown, noise, and vibration in fluid machinery [6]. Nowadays, the work in order to employ the beneficial effects by intentionally inducing cavitation from the ultrasonic acoustic wave, usually referred to as acoustic cavitation, has been widely studied, motivated by engineering and medical needs related to the applications such as the humidifier, nebulizer, cleaner and sonochemistry [130, 136, 133, 98, 23]. When ultrasonic pressure wave is introduced in liquid, cavities composed of air and liquid vapor become formed, vibrated, and further collapsed [112]. After collapsing, four different phenomena are known to take place of the symmetric re-bounce, the liquid-jet shooting toward the direction of negative pressure gradient, the shock-wave caused by the liquid compression, and thermal effects of heating/cooling and luminescence [112]. The violent motion of

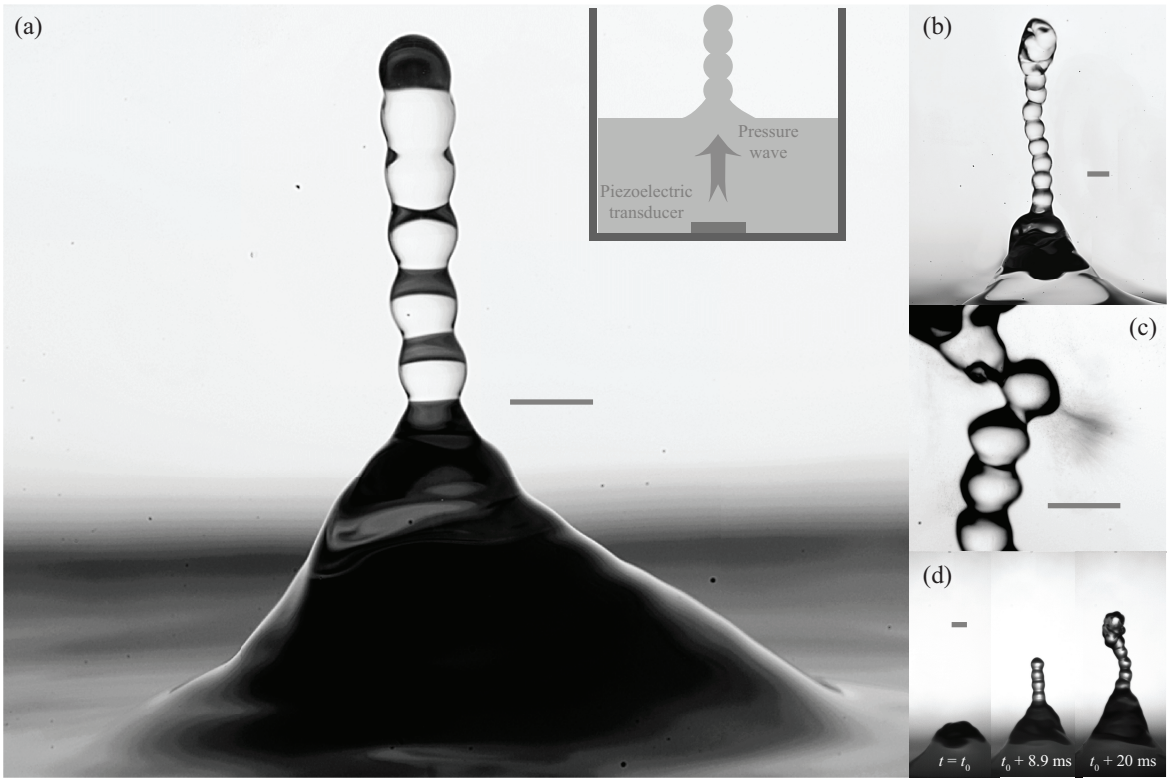

Fig. A.1 (a) Emerging string of water pearls generated by a piezoelectric transducer submerged on the bottom of a water container as schematically shown in the inset. (b) Water becomes accumulated on the top as it reaches the maximum height. (c) Mist cloud being emitted into the air from the string of water pearls. (d) Sequential images of a developing fountain of water pearls. All the scale bars indicate 1 mm.

cavitation bubbles caused by these post-collapse process [98, 113] has been employed to clean textiles or semiconductors [23, 82], while the shock-wave and liquid-jet toward the solid wall due to the boundary effect may cause the harmful damage on the nano-structure on solid surface [82, 80]. The concentrated energy release by the shock-wave and local heating could be beneficial to boosting chemical reaction, which is usually named as sonochemistry [98]. When the cavitation bubble moves near the liquid-air interface, the oscillation of the cavitation bubbles is believed to play a key role in the liquid atomization [125], which forms the basic mechanism for the humidifier and nebulizer [136, 133]. The recent work carried out onboard the parabolic flight has revealed that the post-collapse behavior could be different showing the symmetric re-bounce, rather than shooting liquid jet, due to symmetric collapse in the zero-gravity environment [112, 111]. While asymmetric collapse of cavitation bubble creates the liquid jet toward the solid wall which is known to cause the erosion on the solid [6, 44], the symmetric collapse in the weak pressure gradient field by zero-gravity might not yield the liquid jet [111]. So far there have been theoretical efforts to explain the acoustic cavitation and related phenomena, however it still requires the further study on the detailed mechanism due to its multidisciplinary complexity [130, 113, 96]. When it comes to the applications such as humidifier and nebulizer which will be used for astronauts in space shuttle, more theoretical and experimental consideration should be made for the understanding in the modified pressure gradient field.

Appendix B

Bat drinking on the wing

B.1 Introduction

Most terrestrial and aerial animals drink water while standing, sitting, or kneeling, and use different drinking strategies depending on their body size and mouth morphology [51, 123, 81, 49]. For example, some terrestrial carnivores like dogs and cats drink water by biting down to capture a water column created by a fast moving tongue [51, 123]. Drinking behaviors of aerial animals (Aves) can be classified by the orientation of a beak tip. Zebra finch (*Poephila guttata*) keeps submerging its beak tip down while ladling water to the mouth using its tongue [63, 81]. On the other hand, bengalese finch (*Lonchura striata*) drinks water using gravity as the bird tilts up its beak tip. Interestingly, phalaropes and several other shorebirds are known to drink water by virtue of contact angle hysteresis with repeatedly opening and closing their beak like a tweezering motion [119]. On the contrary, some species of birds such as the common swift (*Apus apus*) [94], the barn swallow (*Hirundo rustica*) [15], the spotted nightjar (*Eurostopodus guttatus*) [28], and the magnificent frigatebird (*Fregata magnificens*) [145], and many species of bats [55, 52] are observed to drink water on the wing. Particularly, bats fly low and skim over the water surface with opening their mouths. Such drinking behaviors could be very dangerous as the bats might tumble into the water even with small mistakes in flight control. However, we have not observed such catastrophic events in the field or lab settings [52]. Presumably, the bats have developed accurate maneuvering techniques to stably fly parallel along the water surface not to wet their face and wings unnecessarily. Similarly, the hovering behavior of hummingbirds has drawn a lot of attention due to its unique aerodynamic characteristics [151, 62] and the potential development of micro air vehicles [74].

Among in-flight drinkers, bats are the only mammals that are able to fly using their membrane wings controlled by skeletal muscles [21, 150]. Their special skeletal structure on the wing enables to flap with higher degree of freedom (> 40) [150, 121], which makes themselves more maneuverable than birds [60]. Together with their unique morphing wings [21, 121], the flapping characteristics of bats have been extensively studied [22, 59, 106]. A wingbeat cycle consists of upstroke and downstroke: during the upstroke, a bat moves both left and right forelimbs upward and backward relative to the body. Then, during the downstroke, the bat brings the forelimbs downward and forward after initially expanding the forelimbs sideways [121]. Even with the underlying complicated aerodynamics in the flapping wings of a bat, the flapping dynamics can be roughly stated in a non-dimensional point of view with three representative dimensionless quantities: Reynolds number (*Re*), an advance ratio (J), and Rossby number (*Ro*) [22, 89]. Reynolds number is defined as $Re = U_f c/\nu$ where U_f is the forward flying speed, c the chord length, and ν the kinematic viscosity of air. The Reynold number indicates the level of turbulent flows around flapping wings. Beyond $Re \sim 10^4$ where most birds and bats fly [90], turbulent flow is known to govern the flapping aerodynamics of animals[22]. Like any other birds and insects [22, 45], bats also employ leading edge vortex (LEV) during the downstroke in order to avoid stall while flying at a slow speed [22, 106]. The formation and stability of the LEV can be estimated by advance ratio and Rossby number respectively. Here, the advance ratio is defined as $J = U_f/U_w = U_f/(2Af)$, where U_w is the flapping wing speed in the stoke plane, A the flapping amplitude, and f the flapping frequency. So, J is often used to indicate the propulsion efficiency of a flapping wing. If one assumes that the flapping frequency is identical to the vortex shedding frequency, then J is equivalent to a half the inverse of Strouhal number. In this way, J also represents the propulsion efficiency by the vortex growth [22]. While J is known to vary between 0 and 5, the optimal propulsive efficiency is known to exist in a range of $J \approx 1-2$.[140] Please note that J is zero for the hovering flight ($U_f = 0$) and is a positive value for the forward flight ($U_f > 0$). Rossby number is used to characterize the revolving wing motion about its shoulder joint by describing the ratio of inertial to Coriolis forces, which can be expressed in terms of the advance ratio as $Ro = (R/c)\sqrt{J^2+1}$, where R is the wing radius [22]. While *Re* is remarkably different from $\mathcal{O}(1)$ for small insects to $\mathcal{O}(10^6)$ for the peregrine falcon (*Falco peregrinus*), J and *Ro* are known to be on a similar order of magnitude for different species of aerial animals [137, 22].

Details in flying characteristics presumably depend on flying tasks (e.g. straight flight [142] and slow turn maneuvering[71]). However, even though many articles qualitatively described the in-flight drinking behavior of bats [55, 56, 108, 52], wing-flapping kinematics

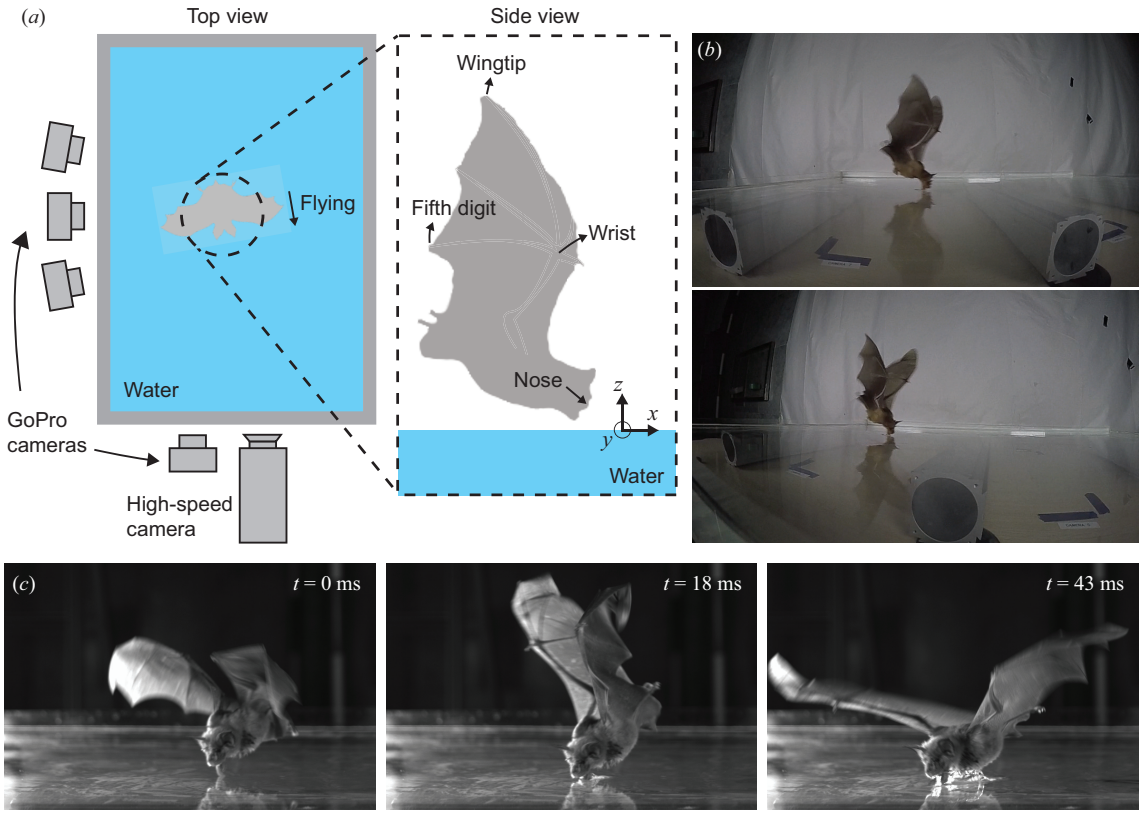

Fig. B.1 (*a*) Schematics of the experiment setup to record the in-flight drinking of bats using multiple GoPro cameras and high speed camera located beside a water container. Anatomical landmarks of wrist, wingtip, fifth digit, and nose are schematically presented on the side view. x and y are the coordinates parallel and perpendicular to the flying direction respectively, however both are parallel to water surface. z is the vertical coordinate above water surface. (*b*) Representative GoPro images captured at the same time for a bat (*Rhinolophus ferrumequinum*) drinking water on the wing. (*c*) Sequential images of in-flight drinking of the bat recored by high-speed camera. The bat starts to dip its tongue on the water surface at $t = 0$, and then scoops water with submerged lower jaw.

in the in-flight drinking have not been studied extensively yet. In the present study, the flapping behavior during the in-flight drinking will be investigated for three different species of bats: greater horseshoe bat (*Rhinolophus ferrumequinum*; weight $\approx$ 25 g), great roundleaf bat (*Hipposideros armiger*; $\approx$ 40 g), and pratt's roundleaf bat (*Hipposideros pratti* $\approx$ 50 g). Three dimensional positions of a bat's nose, wrist, fifth digit, and wingtip are tracked using synchronized multiple cameras. By comparing the flapping kinematics between normal forward flight and drinking flight, we observed statistically significant differences in flapping frequency, amplitude, as well as range-of-motion. From these statistics, we conclude that bats maneuver precisely while drinking, presumably not to wet their eye and nose that emits sonar signals. Despite such highly controlled flapping behaviors, the propulsion efficiency J is observed to show no statistically significant difference. It implies that bats still fly efficiently even with slowing down their flying speed while drinking water.

B.2 Material and Methods

The bat-drinking experiments were conducted at the Virginia Tech–Shandong University International laboratory in Jinan, China. A water container with dimensions of 1 m (length) $\times$ 0.8 m (width) $\times$ 4 cm (height) is placed in the middle of the bat aviary with dimensions of 4 m (length) $\times$ 1.25 m (width) $\times$ 3 m (height). Because the width of the bat aviary is narrow, bats are restricted to fly and drink water along the longer direction of the water container as shown in Fig. B.1(a). To capture the in-flight drinking behaviors of bats, multiple GoPro cameras (GoPro Hero 4, GoPro) and a high-speed camera (Phantom V711, Vision Research) were installed next to the water container. The GoPro cameras were used to record the bats' behavior up to 240 hz during long duration of approximately 1 hour in order to wait for the bats to voluntarily drink water. Before each experiment, we emptied the water in a container to let the bats thirsty for about six hours. All the GoPro cameras were synchronized by virtue of MewPro (Iliad/Orangkucing Lab), whose images were shown in Fig. B.1(b). A high-speed camera is subsidiarily used to capture the drinking events at a higher spatial resolution and at 600 hz as sequentially presented in Fig. B.1(c). To illuminate the experiment spot, white light-emitting diode was used for a bat species (*Rhinolophus ferrumequinum*), however a red light source was used for the experiments with the other species (*Hipposideros armiger* and *Hipposideros pratti*) because they do not prefer to drink water when a white light is illuminated. For comparison, experiments for straight flight were performed using the same setup without the water container. After recording videos, the anatomical landmarks of the wrist, wingtip, fifth digit, and nose were tracked and

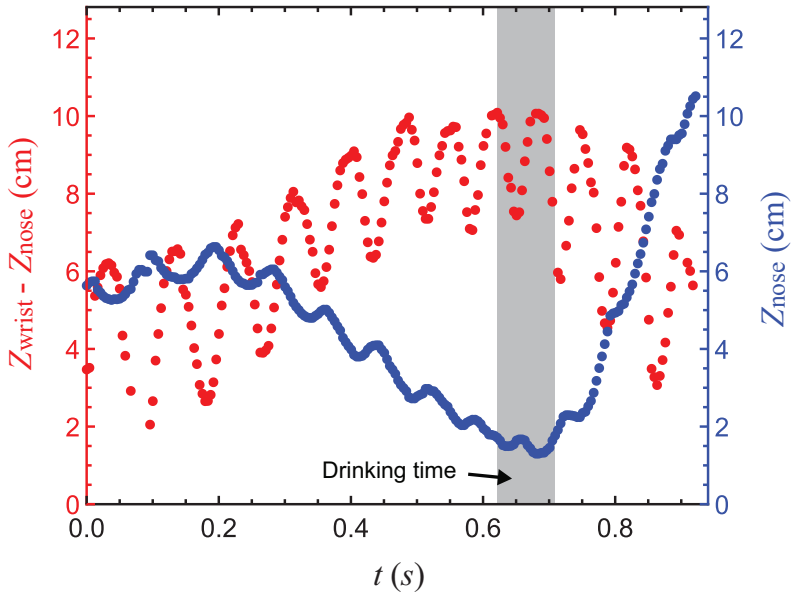

Fig. B.2 Vertical motions of the wrist (Z_{wrist}) and the nose (Z_{nose}) when a bat (*Rhinolophus ferrumequinum*) drinks water on the wing. With the left axis, the evolution of the relative location of the wrist to the nose is presented by red dots in a arch, which reveals that the bat keeps its wrist high, and flaps more frequently in a smaller amplitude. The blue dots with the right axis present the motion of the bat's nose that approaches down and close to the water surface in order to drink water, and then fly out after finished to drink water. Light gray region indicates the time duration when the bat drinks water.

reconstructed in a three-dimensional space by using the pre-built Matlab software [61], which employs the direct linear transformation for 3D reconstruction [1]. Finally, the reconstructed data were processed with in-house Mathematica code.

B.3 Results

B.3.1 Flight kinematics

Figure B.2 presents the vertical motions (red dots) of the wrist position (Z_{wrist}) relative to the nose position (Z_{nose}) of a flying bat (*Rhinolophus ferrumequinum*). A light gray region indicates the time duration when a bat drinks water on the wing. This relative distance ($Z_{\text{wirst}} - Z_{\text{nose}}$) moves along a parabolic trajectory, which reaches the maximum at the drinking moment. It indicates that the bat keeps its wrist as high as possible from the nose, and flaps with smaller amplitude and higher frequency. Meanwhile, the vertical position of the bat's nose (Z_{nose}) denoted by blue dots moves close to, but keeps above the water

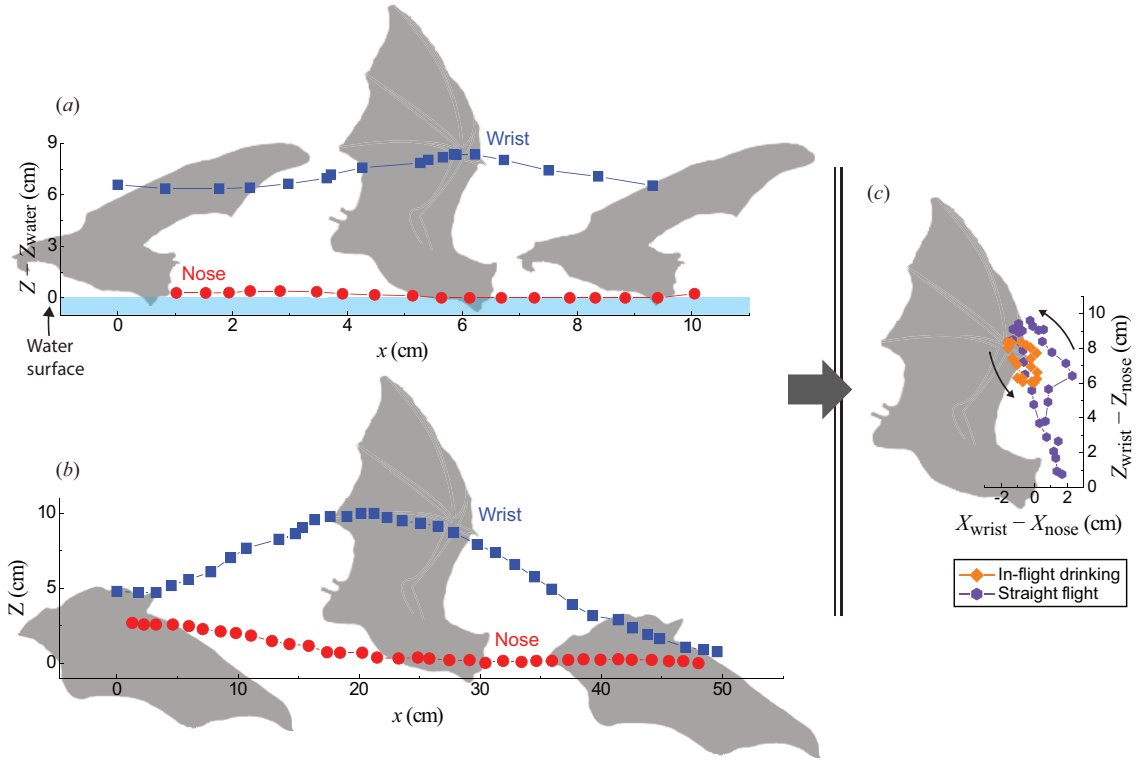

Fig. B.3 Comparison in the spatial motion (Z) of nose and wrist between (*a*) in-flight drinking and (*b*) straight flight of a bat (*Rhinolophus ferrumequinum*). (*a*) While the bat drinks water on the wing, the bat is restricted to fly with maintaining its wrist and wingtip high above the nose as the plot and the silhouette from the experiment image present. (*b*) However, the bat swings its wings fully during the downstroke in the straight flight, moving its wingtip below the nose. (*c*) The different flapping behavior can be more clearly contrasted when the relative motions of X and Z of the wrist to the nose are compared for the in-flight drinking and straight flight.

surface. Also, the bat reduces a vertical vibration of the nose in order to drink water without the face and the wing wet. After drink, the bat swings its wrist at full stroke again with larger amplitude to fly upwards ($Z_{\text{nose}} \uparrow$).

Such flight characteristics are clearly distinguished from those observed in the straight flight of bats [142]. In Fig. B.3, these differences in the wing-flapping behaviors are compared by the vertical motions of the wrist relative to the nose observed for a wingbeat cycle between the drinking flight and straight flight of a bat (*Rhinolophus ferrumequinum*). Please note that '$Z - Z_{\text{water}}$=0' indicates the water level in Fig. B.3(a). The bats are observed to restrict their flapping motions during the downstroke while drinking water, while maintaining the wrist and wingtip high above the water surface. They achieve this by swinging their wrist very little vertically (Fig. B.3(a)). However, during the straight flight, the full stroke of the wrist as shown in Fig. B.3(b) induces the wingtip to move below its nose. It is different from the wing-tip position of silhouette images captured during the downstroke of the in-flight drinking (Fig. B.3(a)). If the bats flap their wings at the full stroke during the drinking flight, their wings would hit the water and get wet, which results in a loss of mechanical energy and fatigue on the wing. Here, '$Z = 0$' does not mean any specific coordinate like the water level because there is no specific reference point for straight flight experiments in Fig. B.3(b). The different flying distance during the wingbeat cycle can be roughly stated. In the wingbeat cycle, the bat flies a shorter distance ≈ 9 cm than that measured in the straight flight ≈ 47 cm as shown in the Fig. B.3(a,b). It might imply that the bats flap at high frequency to drink and fly at a relatively slow speed in order to have better control on in-flight drinking behaviors. Figure B.3(c) presents the relative motions in the X and Z of the wrist to the nose in the moving body-fixed frame. We found that the wrist swing during the straight flight is larger than that during the drinking flight.

The changes in flapping frequency and amplitude are statistically compared for different bat species of *Rhinolophus ferrumequinum* (Fig. B.4(a)) and *Hipposideros pratti* (Fig. B.4(b)), where box plots and statistical significant pairs are presented. A horizontal black bar across the box indicates the median value, and the bottom and top of the box represent the first quartile ($Q1$) and third quartile ($Q3$) respectively. The highest and lowest parts of each whisker indicate the maximum and minimum values of the data. For the pairwise statistical comparison, a non-parametric test was conducted by Wilcoxon signed rank test with significance $\alpha = 0.05$.[153] This test verifies that the flapping frequency and amplitude are statistically different between straight and drinking flights for both *Rhinolophus ferrumequinum* with p-value < 0.001 and *Hipposideros pratti* with p-value < 0.05.

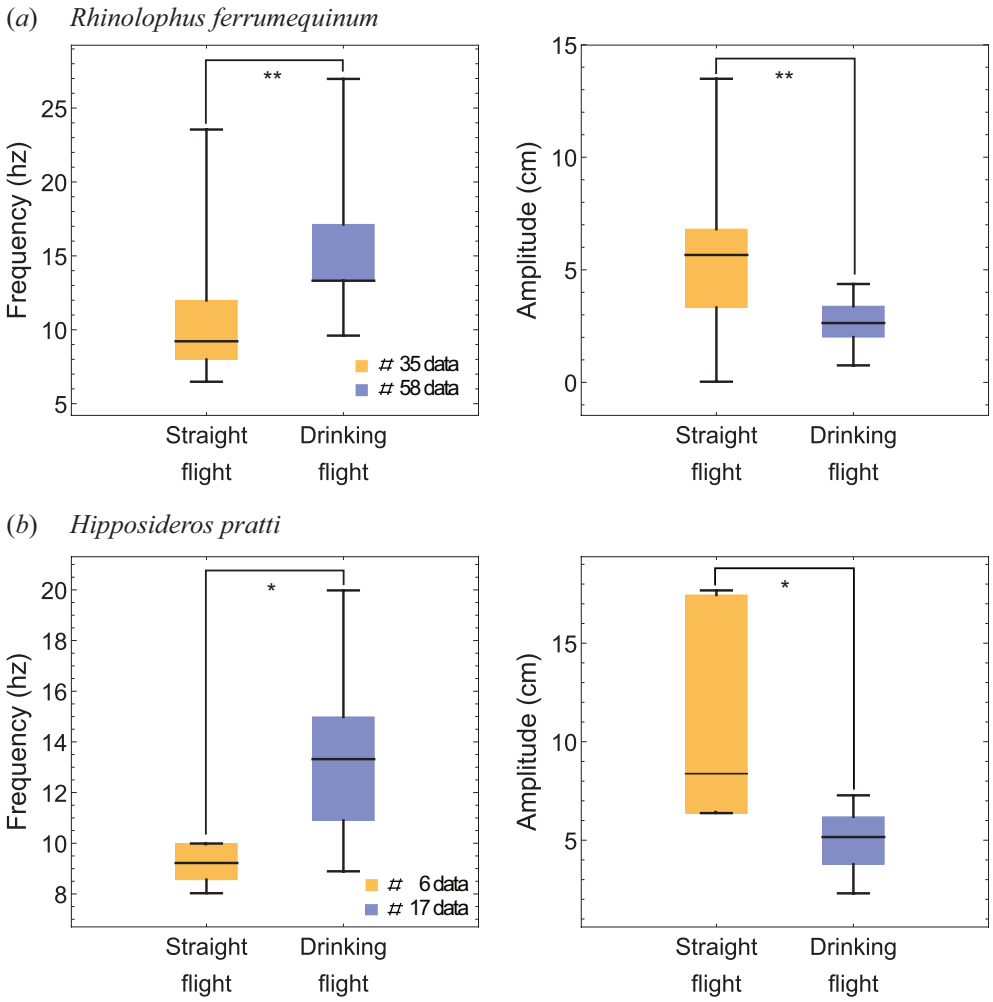

Fig. B.4 Box plots comparing different frequency and amplitude between straight and drinking flights for (*a*) *Rhinolophus ferrumequinum* and (*b*) *Hipposideros pratti*. Significant pairs estimated by Wilcoxon signed rank test are presented with different levels: * $p < 0.05$ and ** $p < 0.001$.

B.4 Conclusion

In-flight drinking behaviors of bats are studied in comparison with flying kinematics of straight flight. We found that bats flap their wings in a more restricted manner while drinking water on the wing. The vertical flapping motion of the bat's wrist is changed to a wing-beat stroke with smaller amplitude and higher frequency. Such a flight strategy helps the bat's nose less vibrate vertically while flying close to the water surface. Moreover, the bats keep their wrist high enough to avoid the wings from impacting the water surface and being wet.

Appendix C

Numerical method to simulate the moving contact line of liquid on a solid surface

C.1 Introduction

Moving contact line is fundamentally important in describing the interfacial behavior of the solid/liquid/air system. Also, the study on this topic is related to industrial applications like ink-jet printing [31]. So far, numerous works have been performed to mathematically model the motion of moving contact line for different experimental conditions [131]. In this appendix, previous approaches that have been used to describe a moving contact line will be summarized as well as these methods will be implemented for simulating a moving contact line of a liquid drop put on a solid surface.

C.2 Previous studies on a moving contact line

C.2.1 Navier slip condition

The most fundamental solid boundary condition is no-slip condition. However, it is apparently not suitable when considering a moving contact line. In the viewpoint of viscous shear stress that $\tau = \mu(\partial u/\partial y)$, it becomes to diverge mathematically for moving a contact line with an acute contact angle ($\theta < 90^\circ$) in that $y \to 0$ near the contact line, where μ is the viscosity and u the velocity being normal to y that is the height from the solid surface. This

divergence is referred to as contact line singularity [134]. From it, there should be no motion of contact line due to infinite viscous resistance. However, this mathematical singularity is definitely not real because a contact line moves easily. Therefore, it is required to modify the mathematical expression of τ at the contact line to allow to slip. Provided a viscous stress at the contact line is finite with not applying no-slip condition, a contact line becomes able to move. In this point of view, the previous studies on modeling a moving contact line have been focused on how to model a viscous stress on the contact line. Navier tried to remedy the limitation of no-slip condition by setting fluid velocity becomes zero virtually inside the solid [109], where l_s is called the slip length that was estimated to be of nanometer scale [42]. By assuming $\partial u/\partial y$ effectively linear beneath the solid due to small length scale, slip velocity can be described as

$$u|_{y=0} = l_s \left.\frac{\partial u}{\partial y}\right|_{y=0}. \tag{C.1}$$

By setting it, we can restrict τ not to diverge because $\delta u \to 0$ as $\delta y \to 0$ compared to the case of no-slip that δu approaches a finite value as $\delta y \to 0$. For Newtonian liquids, l_s is known to follow the proportionality as below [70]:

$$l_s \sim \frac{1}{a^3}\left[\frac{k_B T}{\sigma(1-\cos\theta_e)}\right]^2,$$

where T is the absolute temperature, σ the surface tension coefficient, a the liquid molecular size, θ_e the equilibrium contact angle, k_B the Boltzmann constant, which is the constant relating fluid thermal energy to mechanical pressure. Solving a moving contact-line problem crucially depends on l_s [124]. The l_s has been estimated experimentally and by molecular dynamic simulation [46]. l_s is known to depend on the shear rate ($\partial u/\partial y$) [46, 132, 73, 141] for the following three regimes: first, in the weak slip regime by moderate shear rate, l_s remains constant on the order of a molecular size. Above a critical shear stress, or called the transition regime, l_s becomes to increase linearly with increasing shear rate. In the strong slip regime across the transition regime, l_s stays as a constant value being large compared to that in the weak slip. Moreover, l_s is known to depend on the surface geometry such as roughness or micro & nano structure [144].

C.2.2 Method employing prewetted liquid layer

Along with Navier slip condition, method using prewetted liquid layer also has been acknowledged as an effective method to simulate contact line motion, which relies on

experimental observations: first it is based on the existence of the precursor layer [116]. When a liquid starts to spread on a wettable solid surface, a thin liquid film called 'precursor layer' proceeds faster than the motion of liquid bulk. The thickness of precursor layer is so thin on an order of molecular size that it is not visible by human eye or common optical camera. The existence of the precursor layer was found by use of specific optical device like ellipsometry or molecular dynamic simulation. Second, the spreading dynamics of a liquid on the prewetted surface with the same liquid is known to be identical with that of the liquid spreading on a dry surface if the prewetted thickness is thin enough compared to the liquid bulk thickness [25]. When the prewetted thickness is *not* thin, effective velocity slip makes liquid to spread faster. However, if the prewetted thickness is thin enough, strong viscous stress blocks the effective velocity slip, which might provide the reason why the liquid spreading with precursor layer does not accelerate. The critical thickness of the prewetted layer could be even thicker than a molecular level up to $\sim 100\ \mu$m that depends on μ. Previous numerical studies showed the usefulness of the prewetted layer and applying no-slip solid boundary condition in simulating a contact line motion [100, 101, 107]. One advantage of the prewetted layer method over Navier slip condition is that there is no need to specify l_s before starting a simulation. Because l_s and its dependency on the shear rate are not known for complex surface geometry and non-Newtonian liquids, the usage of prewetted layer could be beneficial. On the other hand, there is a drawback in that the method requires to have very small mesh size less than the critical prewetted thickness. Because the critical thickness depends on μ, careful consideration might be required to use a very fine mesh when it is used for simulating an inviscid flow.

C.3 Drop spreading simulation

In this section, the simulation result will be described based on two methods explained before. As a CFD code, the open source code named as *Gerris* was used [117], which discretizes simulation domain based on the finite volume method [126]. *Gerris* is capable of solving Navier-Stokes equation axi-symmetrically without simplifying the equation and employs volume of fluid method to track a liquid-gas interface [67].

$$\rho \frac{D\underline{u}}{Dt} = -\nabla p + \nabla \cdot \left[\mu(\nabla \underline{u} + \nabla \underline{u}^T)\right] + \sigma \kappa \delta_s \underline{n} + \rho_l \underline{g}, \tag{C.2}$$

where $\underline{u}$ is the fluid velocity vector, p the pressure, κ the curvature of an interface, δ_s the Dirac delta function of the interface being unity in the location of the interface, $\underline{n}$ the unit

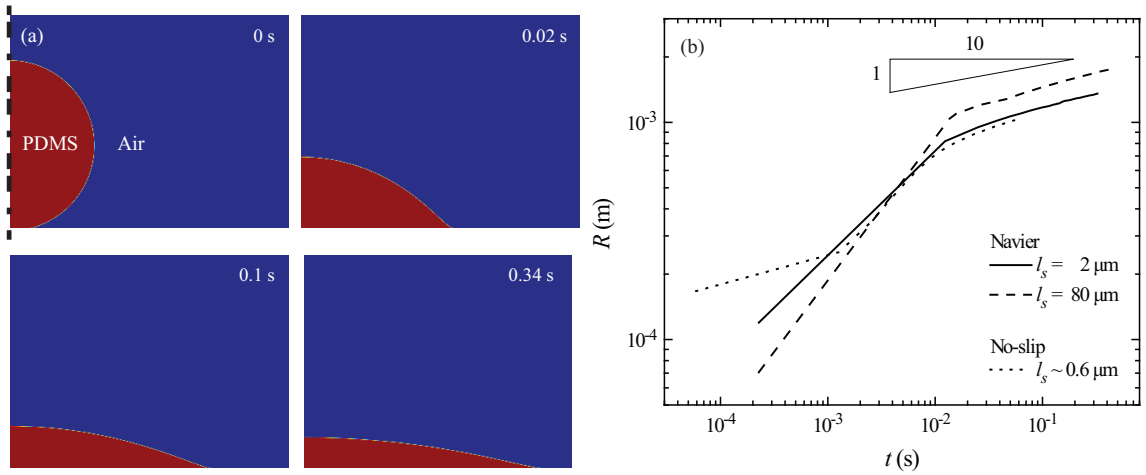

Fig. C.1 (a) Numerical solution of PDMS drop spreading with $a = 0.5$ mm on a solid surface with Navier slip condition with $l_s = 2$ μm. (b) Plot of spreading radius, R, as a function of t for different $l_s = 2$ and 80 μm and no-slip condition, which can be considered to have implicit $l_s \sim 0.6$ μm. For the numerical calculations employing Navier slip condition, the smallest cell size of 2.4 μm were used and 1.2 μm for that with the no-slip condition.

normal vector to the interface, and $\underline{g}$ the gravitational acceleration vector. For the simulation, a traditional liquid drop spreading was tested based on two different boundary conditions. As a liquid, the properties of PDMS (polydimethylsiloxane) 50 cSt were used as $\sigma = 0.02$ N/m, $\rho_l = 965$ kg/m^3, and $\mu = 0.04825$ kg/m·s, where ρ_l is the liquid density. For the air, $\rho_a = 1.2$ kg/m^3 and $\mu = 1.9 \times 10^{-5}$ kg/m·s. For the dynamics of a drop spreading, well-known experimental result is available to follow $R \sim t^{1/10}$ as t goes, which is called Tanner's law [139], where R is the spreading radius of a liquid drop. In the simulation, a liquid drop with $a = 0.5$ mm was gently put on a solid surface with Navier slip condition as in Section C.3.1 and a pre-wetted surface with the same liquid of thin thickness as in Section C.3.2. To evade unnecessary issue of air pocket formation while a liquid drop impacts a bottom, the numerical calculation starts after a little contact between a liquid drop and the bottom is made, which is $t = 0$. It is thought that it does not affect the result because the later spreading behavior is of major interest.

C.3.1 Navier slip condition

In the previous literature, l_s of PDMS was measured to be ≈ 2 μm over silica surface for the weak slip regime of the slip velocity < 5 μm/s and ≈ 80 μm for the strong slip regime > 0.3 mm/s [65]. *Gerris* allows to use Navier slip condition as a boundary condition for a simulation domain through the command of BcNavier. Figure C.1(a) shows temporal

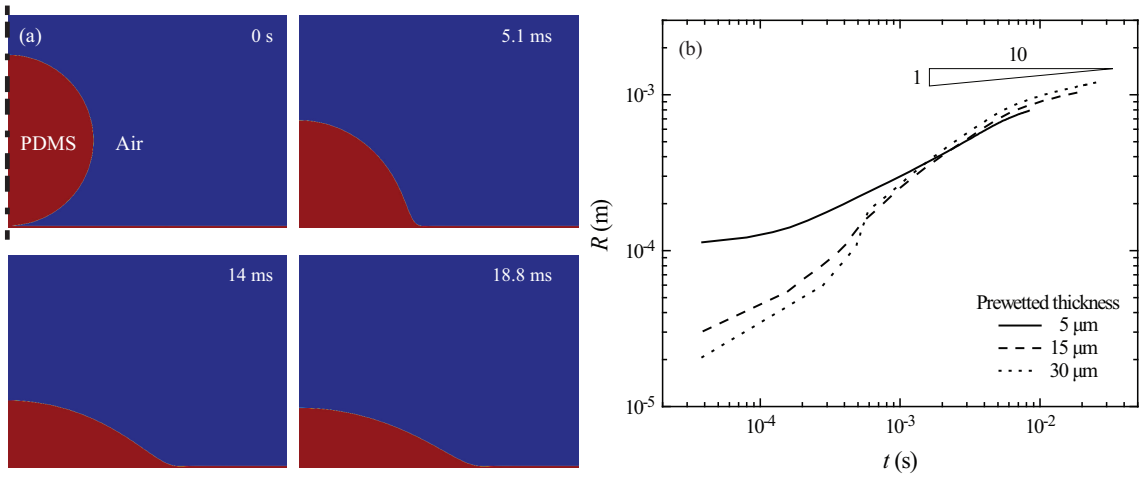

Fig. C.2 (a) Numerical solution of PDMS drop spreading with $a = 0.5$ mm on the prewetted liquid film with the thickness of 15 μm. (b) Plot of spreading radius, R, as a function of t for different prewetted film thickness of 5, 15, and 30 μm. For the numerical calculations employing prewetted liquid film, the smallest cell size of 1.2 μm was used for the thickness of 15 and 30 μm, and 0.61 μm for 5 μm.

evolution of a spreading liquid drop simulated by *Gerris*. Fig. C.1(b) presents the effect of different l_s on the R over t. It is plotted in the log-log scale to compare its log-log slope with 1/10 of Tanner's law. It is found that the log-log slope approaches to 1/10 as t goes , which coincides with the experimental finding, both for $l_s = 2$ and 80 μm. For the case of $l_s = 80$ μm compared to 5 μm, it shows faster spreading, which implies higher proportional constant of $R \sim t^{1/10}$. Slip velocities for Navier slip simulation are estimated ~ 1 mm/s in Tanner's regime for both l_s, which implies $l_s = 80$ μm of the strong slip could be more suitable than $l_s = 2$ μm of the weaker slip regime.

The numerical simulation carried out based on no-slip condition is also compared with Navier slip data as shown in Fig. C.1(b). The present numerical calculation employing the volume of fluid method in *Gerris* is considered to have implicit slip length even for no-slip boundary condition applied [2, 105]. It is because the liquid-air interface is calculated to advect with a velocity calculated inside a mesh, not an edge located on the solid surface. Therefore, it can be considered to have the implicit or effective slip length about half of mesh size. Plot in Fig. C.1(b) presents the time evolution of R over t for the no-slip condition with implicit slip length ~ 0.6 μm. From it, the no-slip data shows the similar time evolution with the data with Naiver slip condition of $l_s = 2$ μm.

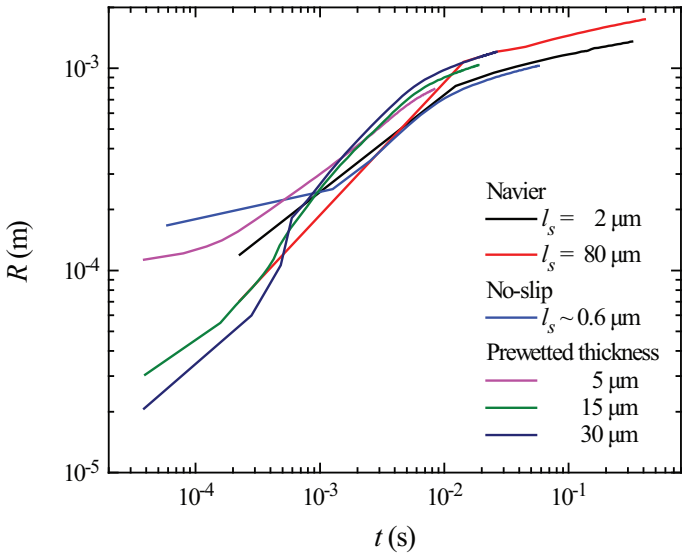

Fig. C.3 Plot of all the data simulated in the present report.

C.3.2 Simulation employing prewetted liquid layer

The same simulation was performed except applying no-slip boundary condition and thin prewetted liquid layer as shown in Fig. C.2, which presents the time evolution of the spreading radius for different film thickness of 5, 15, and 30 μm. The data are found to follow $R \sim t^{1/10}$ as t goes, which agrees with the experimental result. It is shown that the proportional constant for $R \sim t^{1/10}$ decreases as the prewetted film thickness decreases, which makes sense in the viewpoint that more strong viscous stress owing to thinner liquid film is supposed to retard a contact line spreading.

C.3.3 Comparison between two methods

As presented in Fig. C.3, all the data obtained from different methods are plotted in the same graph. All the prewetted data are found to similarly develop with that of the Navier data with $l_s = 80$ μm. For the data with the prewetted film thickness of 30 μm, it shows almost the same evolution with that of Navier data with $l_s = 80$ μm. Because the real slip length is expected to be between 2 and 80 μm [65], it is a desirable to see the data with thinner prewetted film thickness of 5 and 15 μm are plotted between the Navier data of $l_s = 2$ and 80 μm. Please note that it is expected that the data become more accurate when employing thinner prewetted film thickness. Even though the method employing the prewetted film thickness could be easier to be implemented because there is no need to prescribe l_s, there

could be a practical issue to use it because it requires small enough mesh size, which might demand much computation time.

C.4 Summary

The two methods of Naiver slip condition and prewetted liquid layer are discussed, which are widely being used in simulating a contact line motion. Employing the open-source code called *Gerris*, a liquid drop spreading on a bottom surface is tested and simulated to compare these two different boundary conditions. Both boundary conditions are proven to recover the experimental result known as Tanner's law successfully as t goes. Because true l_s is expected to be between 2 and 80 μm but more close to 80 μm, the data with thinner prewetted film thickness ≤ 15 μm is considered to show reasonable result. Even though the method employing the prewetted film thickness is beneficial in that there is no need to prescribe l_s provided that the prewetted film thickness is thin enough, it might demand much computation time owing to small mesh size.

C.5 Source code

C.5.1 Gerris code of Navier slip condition with $l_s = 80$ μm.

```
    # One box length (m)
Define DimensionL 1.25e-3

# Setting the resolution
Define LowResol 6
Define HighResol 8
Define HighResolInterface 8
Define MoreResol 0.0
Define CFLCondition 0.3

# Liquid initial locations (m) and radius (m)
Define LiquidDropRadius 5.0e-4
Define LiquidVertLocation 13e-5
Define LiquidHoriLocation 0.0

# Slip length (m)
Define SlipLength 80.0e-6

# Densities (kg/m^3)
Define Rho_l 965
Define Rho_a 1.2255

# Viscosities (kg/ms)
Define Viscosity_l 0.04825
Define Viscosity_a 1.85e-5

# Surface tension coefficient (kg/s^2)
Define Sigma 0.02

# Max time step (s)
Define TimeStepMax 1.0e-5
```

```
# How frequenty export the outputs
Define OutputPerNumber 250
Define GfsOutputPerNumber 250

# Setting related to movie
Define MovieStep 1.0e-5
Define MovieQuality 10

# Defining the function of VAR to export the viscosity and density as a function of T.
# For VAR, CLAMP function is used to make sure T being in the range of 0 and 1.
Define VAR(T,min,max) ((min-max)*(CLAMP(T,0.,1.)-1.0)/(0.0-1.0)+max)
Define Rho(T) VAR(T,Rho_a,Rho_l)
Define Mu(T) VAR(T,Viscosity_a,Viscosity_l)

#--------------------------------------------------------------------------

3 2 GfsAxi GfsBox GfsGEdge {} {
Time { end = 5.0 dtmax = TimeStepMax }

# Generating interface
VariableTracerVOFHeight T
VariableFiltered TF T 1

# Setting surface tension
VariableCurvature K T
SourceTension T Sigma K

# Below (surface position functions) in the parenthesis should be the same
InitFraction T ((LiquidDropRadius*LiquidDropRadius)-(x+LiquidVertLocation)*(x+LiquidVertLocation)-
y*y)
RefineSurface { return HighResolInterface; } ((LiquidDropRadius*LiquidDropRadius)-
(x+LiquidVertLocation)*(x+LiquidVertLocation)-y*y)
#--------------------------------------------------------------------------
```

```
# Adapting function
AdaptVorticity { istep = 1 } { maxlevel = HighResol minlevel = LowResol cmax = 1e-2
cfactor = 8 }
AdaptGradient { istep = 1 } { maxlevel = HighResolInterface minlevel = LowResol cmax =
1e-6 cfactor = 8 } T

# Setting viscosity, densities, and box length
SourceViscosity Mu(TF)
PhysicalParams {
L = DimensionL
alpha = (1./Rho(TF))
}

# Removing small droplets and bubbles
RemoveDroplets { istep = 1 } T 200 (1-T) 1
RemoveDroplets { istep = 1 } T 200

# Setting gravity
Source {} U -9.81

# Setting accuracy of the calculation
GfsAdvectionParams { cfl = CFLCondition }
ApproxProjectionParams { tolerance = 1e-7 }
ProjectionParams { tolerance = 1e-7 }

# Displaying the simulation sequence by time
OutputTime { istep = 10 } stderr

# Exporting gfs files
OutputSimulation { istart = GfsOutputPerNumber istep = GfsOutputPerNumber } GfsOutput-
Refine-HighResol-CFL-CFLCondition-%ld.gfs
# Exporting main outputs
OutputSimulation { istart = OutputPerNumber istep = OutputPerNumber } SimuOutput-
Refine-HighResol-CFL-CFLCondition-%ld.txt { format = text variables = P,U,V,T }
```

```
# Making movies
OutputPPM { step = MovieStep } { ppm2mpeg > Interface.mpg } {
min = 0 max = 1 v = T maxlevel = MovieQuality }
}

# Boundary conditions
GfsBox {
right = BoundaryOutflow
left = Boundary { BcNavier V 0 SlipLength
BcAngle T 0 }
bottom = Boundary
}
GfsBox {
right = BoundaryOutflow
left = Boundary { BcNavier V 0 SlipLength
BcAngle T 0 }
}
GfsBox {
right = BoundaryOutflow
left = Boundary { BcNavier V 0 SlipLength
BcAngle T 0 }
top = BoundaryOutflow
}
1 2 top
2 3 top
```

C.5.2 Gerris code for the prewetted film with the thickness of 15 μm.

```
# One box length (m)
Define DimensionL 1.25e-3

# Setting the resolution
Define LowResol 6
Define HighResol 9
```

```
Define HighResolInterface 9
Define MoreResol 0.0
Define CFLCondition 0.1

# Liquid initial locations (m) and radius (m)
Define LiquidDropRadius 5.0e-4
Define LiquidVertLocation -10.85e-5
Define LiquidHoriLocation 0.0

# Setting the thickness of prewettedLayer (m)
Define ThicknessPreWetted 15e-6

# Densities (kg/m^3)
Define Rho_l 965
Define Rho_a 1.2255

# Viscosities (kg/ms)
Define Viscosity_l 0.04825
Define Viscosity_a 1.85e-5

# Surface tension coefficient (kg/s^2)
Define Sigma 0.02

# Max time step (s)
Define TimeStepMax 1.0e-5

# How frequenty export the outputs
Define OutputPerNumber 250
Define GfsOutputPerNumber 250

# Setting related to movie
Define MovieStep 5e-6
Define MovieQuality 10

# Defining the function of VAR to export the viscosity and density as a function of T.
```

```
# For VAR, CLAMP function is used to make sure T being in the range of 0 and 1.
Define VAR(T,min,max) ((min-max)*(CLAMP(T,0.,1.)-1.0)/(0.0-1.0)+max)
Define Rho(T) VAR(T,Rho_a,Rho_l)
Define Mu(T) VAR(T,Viscosity_a,Viscosity_l)

#--------------------------------------------------------------------

3 2 GfsAxi GfsBox GfsGEdge {} {
Time { end = 5.0 dtmax = TimeStepMax }

# Generating interface
VariableTracerVOFHeight T
VariableFiltered TF T 1

# Setting surface tension
VariableCurvature K T
SourceTension T Sigma K

# Below (surface position functions) in the parenthesis should be the same
InitFraction T ({if (x <
(0.5*DimensionL-ThicknessPreWetted))
return
((LiquidDropRadius*LiquidDropRadius)-(x+LiquidVertLocation)*(x+LiquidVertLocation)-
y*y);
return (x-0.5*DimensionL+ThicknessPreWetted);})
RefineSurface { return HighResolInterface; } (x-0.5*DimensionL+ThicknessPreWetted)
RefineSurface { return HighResolInterface; } ((LiquidDropRadius*LiquidDropRadius)-
(x+LiquidVertLocation)*(x+LiquidVertLocation)-y*y)
#--------------------------------------------------------------------

# Adapting function
AdaptVorticity { istep = 1 } { maxlevel = HighResol minlevel = LowResol cmax = 1e-2
cfactor = 8 }
AdaptGradient { istep = 1 } { maxlevel = HighResolInterface minlevel = LowResol cmax =
1e-6 cfactor = 8 } T
```

```
# Setting viscosity, densities, and box length
SourceViscosity Mu(TF)
PhysicalParams {
L = DimensionL
alpha = (1./Rho(TF))
}

# Removing small droplets and bubbles
RemoveDroplets { istep = 1 } T 200 (1-T) 1
RemoveDroplets { istep = 1 } T 200

# Setting gravity
Source {} U 9.81

# Setting accuracy of the calculation
GfsAdvectionParams { cfl = CFLCondition }
ApproxProjectionParams { tolerance = 1e-7 }
ProjectionParams { tolerance = 1e-7 }

# Displaying the simulation sequence by time
OutputTime { istep = 10 } stderr

# Exporting gfs files
OutputSimulation { istart = GfsOutputPerNumber istep = GfsOutputPerNumber } GfsOutput-
Refine-HighResol-CFL-CFLCondition-%ld.gfs

# Exporting main outputs
OutputSimulation  istart = OutputPerNumber istep = OutputPerNumber  SimuOutput-Refine-
HighResol-CFL-CFLCondition-%ld.txt { format = text variables = P,U,V,T }

# Making movies OutputPPM { step = MovieStep } { ppm2mpeg > Interface.mpg } {
min = 0 max = 1 v = T maxlevel = MovieQuality }
}
# Boundary conditions
GfsBox { #pid = 0
```

```
left = BoundaryOutflow
right = Boundary { BcDirichlet U 0
BcDirichlet V 0}
bottom = Boundary
}
GfsBox { #pid = 1
left = BoundaryOutflow
right = Boundary { BcDirichlet U 0
BcDirichlet V 0}
}
GfsBox { #pid = 2
left = BoundaryOutflow
right = Boundary { BcDirichlet U 0
BcDirichlet V 0}
top = Boundary
}
1 2 top
2 3 top
```

References

[1] Abdel-Aziz, Y. and Karara, H. (1971). Direct linear transformation into object space coordinates in close-range photogrammetry. In *ASP Symposium on Close-Range Photogrammtery*, pages 1–18, USA. American Society of Photogrammetry.

[2] Afkhami, S., Zaleski, S., and Bussmann, M. (2009). A mesh-dependent model for applying dynamic contact angles to VOF simulations. *J. Comput. Phy.*, 228(15):5370–5389.

[3] Al-Otoom, A. (2008). An investigation into beneficiation of jordanian el-lajjun oil shale by froth floatation. *Oil Shale*, 25(2).

[4] Albijanic, B., Ozdemir, O., Nguyen, A. V., and Bradshaw, D. (2010). A review of induction and attachment times of wetting thin films between air bubbles and particles and its relevance in the separation of particles by flotation. *Adv. Colloid Interface Sci.*, 159(1):1–21.

[5] Aristoff, J. M. and Bush, J. W. (2009). Water entry of small hydrophobic spheres. *J. Fluid Mech.*, 619:45–78.

[6] Arndt, R. E. (1981). Cavitation in fluid machinery and hydraulic structures. *Annu. Rev. Fluid Mech.*, 13(1):273–326.

[7] Au, D. and Weihs, D. (1980). At high speeds dolphins save energy by leaping. *Nature*, 284(5756):548–550.

[8] Bartolo, D., Josserand, C., and Bonn, D. (2005). Retraction dynamics of aquous drops upon impact on nonwetting surfaces. *J. Fluid Mech.*, 545:329–338.

[9] Baver, C. E., Parlange, J., Stoof, C. R., DiCarlo, D. A., Wallach, R., Durnford, D. S., Steenhuis, T. S., et al. (2014). Capillary pressure overshoot for unstable wetting fronts

is explained by hoffman's velocity-dependent contact-angle relationship. *Water Resour. Res.*, 50(6):5290–5297.

[10] Biance, A.-L., Clanet, C., and Quéré, D. (2004). First steps in the spreading of a liquid droplet. *Phys. Rev. E*, 69(1):016301.

[11] Bonn, D., Eggers, J., Indekeu, J., Meunier, J., and Rolley, E. (2009). Wetting and spreading. *Rev. Mod. Phys.*, 81(2):739.

[12] Boreyko, J. B. and Chen, C.-H. (2009). Self-propelled dropwise condensate on superhydrophobic surfaces. *Phys. Rev. Lett.*, 103(18):184501.

[13] Brooks, J. L. and Dodson, S. I. (1965). Predation, body size, and composition of plankton. *Science*, 150(3692):28–35.

[14] Burton, J., Rutledge, J., and Taborek, P. (2004). Fluid pinch-off dynamics at nanometer length scales. *Phys. Rev. Lett.*, 92(24):244505.

[15] Burtt Jr, E. H., Bitterbaum, E. J., and Hailman, J. P. (1988). Head-scratching method in swallows depends on behavioral context. *Wilson Bull.*, pages 679–682.

[16] Bush, J. W. and Hu, D. L. (2006). Walking on water: biolocomotion at the interface. *Annu. Rev. Fluid Mech.*, 38:339–369.

[17] Bush, J. W., Hu, D. L., and Prakash, M. (2007). The integument of water-walking arthropods: form and function. *Adv. Insect Physiol.*, 34:117–192.

[18] Buskey, E. J. and Hartline, D. K. (2003). High-speed video analysis of the escape responses of the copepod acartia tonsa to shadows. *Biol. Bull.*, 204(1):28–37.

[19] Chang, B., Croson, M., Straker, L., Gart, S., Dove, C., Gerwin, J., and Jung, S. (2016). How seabirds plunge-dive without injuries. *Proc. Natl. Acad. Sci.*, page 201608628.

[20] Chen, J.-D. (1988). Experiments on a spreading drop and its contact angle on a solid. *J. Colloid Interf. Sci.*, 122(1):60–72.

[21] Cheney, J., Konow, N., Middleton, K., Breuer, K., Roberts, T., Giblin, E., and Swartz, S. (2014). Membrane muscle function in the compliant wings of bats. *Bioinspir. Biomim.*, 9(2):025007.

[22] Chin, D. D. and Lentink, D. (2016). Flapping wing aerodynamics: from insects to vertebrates. *J. Exp. Biol.*, 219(7):920–932.

[23] Choi, J., Kim, T.-H., Kim, H.-Y., and Kim, W. (2016). Ultrasonic washing of textiles. *Ultrason. Sonochem.*, 29:563–567.

[24] Choi, W., Tuteja, A., Mabry, J. M., Cohen, R. E., and McKinley, G. H. (2009). A modified cassie–baxter relationship to explain contact angle hysteresis and anisotropy on non-wetting textured surfaces. *J. Colloid Interf. Sci.*, 339(1):208–216.

[25] Cormier, S. L., McGraw, J. D., Salez, T., Raphaël, E., and Dalnoki-Veress, K. (2012). Beyond tanner's law: Crossover between spreading regimes of a viscous droplet on an identical film. *Phys. Rev. Lett.*, 109(15):154501.

[26] Cox, R. (1986). The dynamics of the spreading of liquids on a solid surface. part 1. viscous flow. *J. Fluid Mech.*, 168:169–194.

[27] Davenport, J. (1994). How and why do flying fish fly? *Rev. Fish Biol. Fisher*, 4(2):184–214.

[28] Dawson, W. R. and Fisher, C. D. (1969). Responses to temperature by the spotted nightjar (eurostopodus guttatus). *Condor*, 71(1):49–53.

[29] de Gennes, P.-G. (1986). Deposition of langmuir-blodgett layers. *Colloid Polym. Sci.*, 264(5):463–465.

[30] Dennis, S. and Walker, J. (1971). Calculation of the steady flow past a sphere at low and moderate reynolds numbers. *J. Fluid Mech.*, 48(04):771–789.

[31] Derby, B. (2010). Inkjet printing of functional and structural materials: fluid property requirements, feature stability, and resolution. *Annu. Rev. Mater. Res.*, 40:395–414.

[32] Ding, H., Chen, B.-Q., Liu, H.-R., Zhang, C.-Y., Gao, P., and Lu, X.-Y. (2015). On the contact-line pinning in cavity formation during solid–liquid impact. *J. Fluid Mech.*, 783:504–525.

[33] Do-Quang, M. and Amberg, G. (2009). The splash of a solid sphere impacting on a liquid surface: numerical simulation of the influence of wetting. *Phys. Fluids*, 21(2):022102.

[34] Dodds, S., Carvalho, M., and Kumar, S. (2011). Stretching liquid bridges with moving contact lines: The role of inertia. *Phys. Fluids*, 23(9):092101.

[35] Duchemin, L., Le Dizès, S., Vincent, L., and Villermaux, E. (2015). Self-similar impulsive capillary waves on a ligament. *Phys. Fluids*, 27(5):051704.

[36] Duclaux, V., Caillé, F., Duez, C., Ybert, C., Bocquet, L., and Clanet, C. (2007). Dynamics of transient cavities. *J. Fluid Mech.*, 591:1–19.

[37] Duez, C., Ybert, C., Clanet, C., and Bocquet, L. (2007). Making a splash with water repellency. *Nature Phys.*, 3(3):180–183.

[38] Eggers, J. (1993). Universal pinching of 3d axisymmetric free-surface flow. *Phys. Rev. Lett.*, 71(21):3458.

[39] Eggers, J. (1995). Theory of drop formation. *Phys. Fluids*, 7(5):941–953.

[40] Eggers, J. (2005). Existence of receding and advancing contact lines. *Phys. Fluids*, 17(8):082106.

[41] Eggers, J. and Dupont, T. F. (1994). Drop formation in a one-dimensional approximation of the navier–stokes equation. *J. Fluid Mech.*, 262:205–221.

[42] Eggers, J. and Stone, H. A. (2004). Characteristic lengths at moving contact lines for a perfectly wetting fluid: the influence of speed on the dynamic contact angle. *J. Fluid Mech.*, 505:309–321.

[43] Eggers, J. and Villermaux, E. (2008). Physics of liquid jets. *Rep. Prog. Phys.*, 71(3):036601.

[44] Eisenberg, P. (1950). *On the mechanism and prevention of cavitation*. Navy Department, David W. Taylor Model Basin.

[45] Ellington, C. P., Van Den Berg, C., Willmott, A. P., and Thomas, A. L. (1996). Leading-edge vortices in insect flight. *Nature*, 384(6610):626.

[46] Ellis, J. S. and Thompson, M. (2004). Slip and coupling phenomena at the liquid–solid interface. *Phys. Chem. Chem. Phys.*, 6(21):4928–4938.

[47] Fermigier, M. and Jenffer, P. (1991). An experimental investigation of the dynamic contact angle in liquid-liquid systems. *J. Colloid Interf. Sci.*, 146(1):226–241.

[48] Fezzaa, K. and Wang, Y. (2008). Ultrafast x-ray phase-contrast imaging of the initial coalescence phase of two water droplets. *Phys. Rev. Lett.*, 100(10):104501.

[49] Fisher, C. D., Lindgren, E., and Dawson, W. R. (1972). Drinking patterns and behavior of australian desert birds in relation to their ecology and abundance. *Condor*, 74(2):111–136.

[50] Frankel, I. and Weihs, D. (1985). Stability of a capillary jet with linearly increasing axial velocity (with application to shaped charges). *J. Fluid Mech.*, 155:289–307.

[51] Gart, S., Socha, J. J., Vlachos, P. P., and Jung, S. (2015). Dogs lap using acceleration-driven open pumping. *Proc. Natl. Acad. Sci.*, 112(52):15798–15802.

[52] Gart, S. W. (2016). *Interfacial fluid dynamics inspired by natural systems*. PhD thesis, Virginia Tech.

[53] Gemmell, B. J., Jiang, H., Strickler, J. R., and Buskey, E. J. (2012). Plankton reach new heights in effort to avoid predators. *Proc. R. Soc. Lond. B Biol. Sci.*, 279(1739):2786–2792.

[54] Gilet, T. and Bush, J. W. (2009). The fluid trampoline: droplets bouncing on a soap film. *J. Fluid Mech.*, 625:167–203.

[55] Greif, S. and Siemers, B. M. (2010). Innate recognition of water bodies in echolocating bats. *Nat. Commun.*, 1:107.

[56] Griffiths, S. R. (2013). Echolocating bats emit terminal phase buzz calls while drinking on the wing. *Behav. Process*, 98:58–60.

[57] Gueyffier, D., Li, J., Nadim, A., Scardovelli, R., and Zaleski, S. (1999). Volume-of-fluid interface tracking with smoothed surface stress methods for three-dimensional flows. *J. Comput. Phys.*, 152(2):423–456.

[58] Hansson, L.-A., Hylander, S., and Sommaruga, R. (2007). Escape from uv threats in zooplankton: a cocktail of behavior and protective pigmentation. *Ecology*, 88(8):1932–1939.

[59] Hedenström, A., Johansson, L., Wolf, M., Von Busse, R., Winter, Y., and Spedding, G. R. (2007). Bat flight generates complex aerodynamic tracks. *Science*, 316(5826):894–897.

[60] Hedenström, A., Johansson, L. C., and Spedding, G. R. (2009). Bird or bat: comparing airframe design and flight performance. *Bioinspir. Biomim.*, 4(1):015001.

[61] Hedrick, T. L. (2008). Software techniques for two-and three-dimensional kinematic measurements of biological and biomimetic systems. *Bioinspir. Biomim.*, 3(3):034001.

[62] Hedrick, T. L., Cheng, B., and Deng, X. (2009). Wingbeat time and the scaling of passive rotational damping in flapping flight. *Science*, 324(5924):252–255.

[63] Heidweiller, J. and Zweers, G. (1990). Drinking mechanisms in the zebra finch and the bengalese finch. *Condor*, 92:1–28.

[64] Herman, L. M. (1980). *Cetacean behavior: mechanisms and functions*. New York, NY (USA) Wiley Interscience.

[65] Hervet, H. and Léger, L. (2003). Flow with slip at the wall: from simple to complex fluids. *C. R. Phys.*, 4(2):241–249.

[66] Hinch, E. J. (1991). *Perturbation methods*. Cambridge university press.

[67] Hirt, C. W. and Nichols, B. D. (1981). Volume of fluid (vof) method for the dynamics of free boundaries. *J. Comput. Phys.*, 39(1):201–225.

[68] Hoffman, R. L. (1975). A study of the advancing interface. i. interface shape in liquid—gas systems. *J. Colloid Interf. Sci.*, 50(2):228–241.

[69] Hoffman, R. L. (1983). A study of the advancing interface: Ii. theoretical prediction of the dynamic contact angle in liquid-gas systems. *J. Colloid Interf. Sci.*, 94(2):470–486.

[70] Huang, D. M., Sendner, C., Horinek, D., Netz, R. R., and Bocquet, L. (2008). Water slippage versus contact angle: A quasiuniversal relationship. *Phys. Rev. Lett.*, 101(22):226101.

[71] Iriarte-Díaz, J. and Swartz, S. M. (2008). Kinematics of slow turn maneuvering in the fruit bat cynopterus brachyotis. *J. Exp. Biol.*, 211(21):3478–3489.

[72] Jiang, X. F., Zhu, C., and Li, H. Z. (2016). Bubble pinch-off in newtonian and non-newtonian fluids. *Chem. Eng. Sci.*

[73] Joseph, P. and Tabeling, P. (2005). Direct measurement of the apparent slip length. *Phys. Rev. E*, 71(3):035303.

[74] Keennon, M., Klingebiel, K., Won, H., and Andriukov, A. (2012). Development of the nano hummingbird: A tailless flapping wing micro air vehicle. In *AIAA aerospace sciences meeting*, pages 1–24. AIAA Reston, VA.

[75] Kim, H. J. and Durbin, P. A. (1988). Observations of the frequencies in a sphere wake and of drag increase by acoustic excitation. *Phys. fluids*, 31(11):3260–3265.

[76] Kim, S. J., Choi, J. W., Moon, M.-W., Lee, K.-R., Chang, Y. S., Lee, D.-Y., and Kim, H.-Y. (2015a). Wicking and flooding of liquids on vertical porous sheets. *Phys. Fluids*, 27(3):032105.

[77] Kim, S. J., Hasanyan, J., Gemmell, B. J., Lee, S., and Jung, S. (2015b). Dynamic criteria of plankton jumping out of water. *J. R. Soc. Interface*, 12(111):20150582.

[78] Kim, S. J., Kim, J., Moon, M.-W., Lee, K.-R., and Kim, H.-Y. (2013). Experimental study of drop spreading on textured superhydrophilic surfaces. *Phys. Fluids*, 25(9):092110.

[79] Kim, S. J., Moon, M.-W., Lee, K.-R., Lee, D.-Y., Chang, Y. S., and Kim, H.-y. (2011). Liquid spreading on superhydrophilic micropillar arrays. *J. Fluid Mech.*, 680:477–487.

[80] Kim, T.-H. and Kim, H.-Y. (2014). Disruptive bubble behaviour leading to microstructure damage in an ultrasonic field. *J. Fluid Mech.*, 750:355–371.

[81] Kim, W. and Bush, J. W. (2012). Natural drinking strategies. *J. Fluid Mech.*, 705:7–25.

[82] Kim, W., Park, K., Oh, J., Choi, J., and Kim, H.-Y. (2010). Visualization and minimization of disruptive bubble behavior in ultrasonic field. *Ultrasonics*, 50(8):798–802.

[83] Knutsen, T., Melle, W., and Calise, L. (2001). Determining the mass density of marine copepods and their eggs with a critical focus on some of the previously used methods. *J. Plankton Res.*, 23(8):859–873.

[84] Kondratieff, M. C. and Myrick, C. A. (2006). How high can brook trout jump? a laboratory evaluation of brook trout jumping performance. *T. Am. Fish Soc.*, 135(2):361–370.

[85] Kumar, S. (2015). Liquid transfer in printing processes: liquid bridges with moving contact lines. *Annu. Rev. Fluid Mech.*, 47:67–94.

[86] Landau L, L. E. (1959). *Fluid Mechanics*. London: Pergamon.

[87] Lee, D.-G. and Kim, H.-Y. (2011). Sinking of small sphere at low reynolds number through interface. *Phys. Fluids*, 23(7):072104.

[88] Lee, S. (2000). A numerical study of the unsteady wake behind a sphere in a uniform flow at moderate reynolds numbers. *Comput. Fluids*, 29(6):639–667.

[89] Lentink, D. and Dickinson, M. H. (2009a). Biofluiddynamic scaling of flapping, spinning and translating fins and wings. *J. Exp. Biol.*, 212(16):2691–2704.

[90] Lentink, D. and Dickinson, M. H. (2009b). Rotational accelerations stabilize leading edge vortices on revolving fly wings. *J Exp. Biol.*, 212(16):2705–2719.

[91] Lian, G., Thornton, C., and Adams, M. J. (1993). A theoretical study of the liquid bridge forces between two rigid spherical bodies. *J. Colloid Interf. Sci.*, 161(1):138–147.

[92] Liu, D., Evans, G., and He, Q. (2016). Critical fall height for particle capture in film flotation: Importance of three phase contact line velocity and dynamic contact angle. *Chem. Eng. Res. Des.*, 114:52–59.

[93] Liu, D., He, Q., and Evans, G. (2010). Penetration behaviour of individual hydrophilic particle at a gas–liquid interface. *Adv. Powder Technol.*, 21(4):401–411.

[94] Lockley, R. (1969). Non-stop flight and migration in the common swift apus apus. *Ostrich*, 40(S1):265–269.

[95] Lopez, J., Miller, C. A., and Ruckenstein, E. (1976). Spreading kinetics of liquid drops on solids. *J. Colloid Interf. Sci.*, 56(3):460–468.

[96] Louisnard, O. and González-García, J. (2011). Acoustic cavitation. In *Ultrasound technologies for food and bioprocessing*, pages 13–64. Springer.

[97] Lowry, D., Wintzer, A. P., Matott, M. P., Whitenack, L. B., Huber, D. R., Dean, M., and Motta, P. J. (2005). Aerial and aquatic feeding in the silver arawana, osteoglossum bicirrhosum. *Env. Biol. Fish.*, 73(4):453–462.

[98] Luo, J., Fang, Z., Smith Jr, R. L., and Qi, X. (2015). Fundamentals of acoustic cavitation in sonochemistry. In *Production of Biofuels and Chemicals with Ultrasound*, pages 3–33. Springer.

[99] Lusseau, D. (2006). Why do dolphins jump? interpreting the behavioural repertoire of bottlenose dolphins (tursiops sp.) in doubtful sound, new zealand. *Behav. Processes*, 73(3):257–265.

[100] Mahady, K., Afkhami, S., and Kondic, L. (2015). A volume of fluid method for simulating fluid/fluid interfaces in contact with solid boundaries. *J. Comput. Phys.*, 294:243–257.

[101] Mahady, K., Afkhami, S., and Kondic, L. (2016). A numerical approach for the direct computation of flows including fluid-solid interaction: Modeling contact angle, film rupture, and dewetting. *Phys. Fluids*, 28(6):062002.

[102] Marchand, A., Chan, T. S., Snoeijer, J. H., and Andreotti, B. (2012). Air entrainment by contact lines of a solid plate plunged into a viscous fluid. *Phys. Rev. Lett.*, 108(20):204501.

[103] Marmottant, P. and Villermaux, E. (2004). Fragmentation of stretched liquid ligaments. *Phys. Fluids*, 16(8):2732–2741.

[104] McHale, G., Newton, M. I., and Shirtcliffe, N. J. (2009). Dynamic wetting and spreading and the role of topography. *J. Phys. Condens. Matter*, 21(46):464122.

[105] Moriarty, J. and Schwartz, L. (1992). Effective slip in numerical calculations of moving-contact-line problems. *J. Eng. Math.*, 26(1):81–86.

[106] Muijres, F., Johansson, L., Barfield, R., Wolf, M., Spedding, G., and Hedenström, A. (2008). Leading-edge vortex improves lift in slow-flying bats. *Science*, 319(5867):1250–1253.

[107] Mumley, T. E., Radke, C., and Williams, M. C. (1986). Kinetics of liquid/liquid capillary rise: Ii. development and test of theory. *J. Colloid Interface Sci.*, 109(2):413–425.

[108] Naughton, D. (2012). *The natural history of Canadian mammals*. University of Toronto Press.

[109] Navier, C. (1823). Mémoire sur les lois du mouvement des fluids. *Mem. Acad. Sci. Inst. Fr.*, 6:389–416.

[110] NB., M. (2012). *Life of Fishes*. London: Weidenfield and Nicolson.

[111] Obreschkow, D., Tinguely, M., Dorsaz, N., Kobel, P., De Bosset, A., and Farhat, M. (2011). Universal scaling law for jets of collapsing bubbles. *Phys. Rev. Lett.*, 107(20):204501.

[112] Obreschkow, D., Tinguely, M., Dorsaz, N., Kobel, P., De Bosset, A., and Farhat, M. (2013). The quest for the most spherical bubble: experimental setup and data overview. *Exp. Fluids*, 54(4):1503.

[113] Peshkovsky, S. L. and Peshkovsky, A. S. (2008). Shock-wave model of acoustic cavitation. *Ultrason. Sonochem.*, 15(4):618–628.

[114] Petrov, J. and Sedev, R. (1985). On the existence of a maximum speed of wetting. *Colloids Surf.*, 13:313–322.

[115] Plateau, J. A. F. (1873). *Statique expérimentale et théorique des liquides soumis aux seules forces moléculaires*, volume 2. Gauthier-Villars.

[116] Popescu, M. N., Oshanin, G., Dietrich, S., and Cazabat, A. (2012). Precursor films in wetting phenomena. *J. Phys. Condens. Matter*, 24(24):243102.

[117] Popinet, S. (2003). Gerris: a tree-based adaptive solver for the incompressible euler equations in complex geometries. *J. Comput. Phys.*, 190(2):572–600.

[118] Popinet, S. (2018). Numerical models of surface tension. *Annu. Rev. Fluid Mech.*, 50:1–28.

[119] Prakash, M., Quéré, D., and Bush, J. W. (2008). Surface tension transport of prey by feeding shorebirds: the capillary ratchet. *Science*, 320(5878):931–934.

[120] Quéré, D. (2008). Wetting and roughness. *Annu. Rev. Mater. Res.*, 38:71–99.

[121] Ramezani, A., Chung, S.-J., and Hutchinson, S. (2017). A biomimetic robotic platform to study flight specializations of bats. *Sci. Robot.*, 2(3):eaal2505.

[122] Rayleigh, L. (1878). On the instability of jets. *Proc. Lond. Math. Soc.*, 1(1):4–13.

[123] Reis, P. M., Jung, S., Aristoff, J. M., and Stocker, R. (2010). How cats lap: water uptake by felis catus. *Science*, 330(6008):1231–1234.

[124] Renardy, M., Renardy, Y., and Li, J. (2001). Numerical simulation of moving contact line problems using a volume-of-fluid method. *J. Comput. Phys.*, 171(1):243–263.

[125] Rozenberg, L. (2013). *Physical principles of ultrasonic technology*, volume 1. Springer Science & Business Media.

[126] Samet, H. (1990). Applications of spatial data structures.

[127] Scheludko, A., Toshev, B., and Bojadjiev, D. (1976). Attachment of particles to a liquid surface (capillary theory of flotation). *J. Chem. Soc. Farad. T. 1*, 72:2815–2828.

[128] Schiaffino, S. and Sonin, A. A. (1997). Molten droplet deposition and solidification at low weber numbers. *Phys. Fluids*, 9(11):3172–3187.

[129] Shang, B., Yu, X., Zheng, H., Xie, B., Chen, Q., and Luo, X. (2016). Numerical and experimental study on the transferred volume in phosphor dip-transfer coating process of light-emitting diodes packaging. *J. Electron. Packag.*, 138(2):021003.

[130] Simon, J. C., Sapozhnikov, O. A., Khokhlova, V. A., Crum, L. A., and Bailey, M. R. (2015). Ultrasonic atomization of liquids in drop-chain acoustic fountains. *J. Fluid Mech.*, 766:129–146.

[131] Snoeijer, J. H. and Andreotti, B. (2013). Moving contact lines: scales, regimes, and dynamical transitions. *Annu. Rev. Fluid Mech.*, 45:269–292.

[132] Spikes, H. and Granick, S. (2003). Equation for slip of simple liquids at smooth solid surfaces. *Langmuir*, 19(12):5065–5071.

[133] Steckel, H. and Eskandar, F. (2003). Factors affecting aerosol performance during nebulization with jet and ultrasonic nebulizers. *Eur. J. Pharm. Sci.*, 19(5):443–455.

[134] Sui, Y., Ding, H., and Spelt, P. D. (2014). Numerical simulations of flows with moving contact lines. *Annu. Rev. Fluid Mech.*, 46:97–119.

[135] Sulak, K., Edwards, R., Hill, G., and Randall, M. (2002). Why do sturgeons jump? insights from acoustic investigations of the gulf sturgeon in the suwannee river, florida, usa. *J. Appl. Ichthyol.*, 18(4-6):617–620.

[136] Sung, C.-C., Bai, C.-Y., Chen, J.-H., and Chang, S.-J. (2013). Controllable fuel cell humidification by ultrasonic atomization. *J. Power Sources*, 239:151–156.

[137] Swartz, S. M., Breuer, K. S., and Willis, D. J. (2008). Aeromechanics in aeroecology: flight biology in the aerosphere. *Integr. Comp. Biol.*, 48(1):85–98.

[138] Tan, X., Wu, W. G., Wang, Z. M., and Liu, H. (2014). Experimental study on comprehensive recovery of valuable minerals from flotation tailings in copper–molybdenum mine. *Adv. Mat. Res*, 878:234–243.

[139] Tanner, L. H. (1979). The spreading of silicone oil drops on horizontal surfaces. *J. Phys. D: Appl. Phys.*, 12(9):1473.

[140] Taylor, G. K., Nudds, R. L., and Thomas, A. L. (2003). Flying and swimming animals cruise at a strouhal number tuned for high power efficiency. *Nature*, 425(6959):707.

[141] Thompson, P. A. and Troian, S. M. (1997). A general boundary condition for liquid flow at solid surfaces. *Nature*, 389(6649):360–362.

[142] Tian, X., Iriarte-Diaz, J., Middleton, K., Galvao, R., Israeli, E., Roemer, A., Sullivan, A., Song, A., Swartz, S., and Breuer, K. (2006). Direct measurements of the kinematics and dynamics of bat flight. *Bioinspir. Biomim.*, 1(4):S10.

[143] Truscott, T. T., Epps, B. P., and Belden, J. (2014). Water entry of projectiles. *Annu. Rev. Fluid Mech.*, 46:355–378.

[144] Tsai, P., Peters, A. M., Pirat, C., Wessling, M., Lammertink, R. G., and Lohse, D. (2009). Quantifying effective slip length over micropatterned hydrophobic surfaces. *Phys. Fluids*, 21(11):112002.

[145] Van Tets, G. F. (1965). A comparative study of some social communication patterns in the pelecaniformes. *Ornithol. Monogr.*, (2):1–88.

[146] Vella, D. (2015). Floating versus sinking. *Annu. Rev. Fluid Mech.*, 47:115–135.

[147] Vella, D., Lee, D.-G., and Kim, H.-Y. (2006). Sinking of a horizontal cylinder. *Langmuir*, 22(7):2972–2974.

[148] Vincent, L., Duchemin, L., and Villermaux, E. (2014). Remnants from fast liquid withdrawal. *Phys. Fluids*, 26(3):031701.

[149] Voinov, O. (1976). Hydrodynamics of wetting. *Fluid Dyn.*, 11(5):714–721.

[150] Wang, S., Zhang, X., He, G., and Liu, T. (2015). Lift enhancement by bats9 dynamically changing wingspan. *J. R. Soc. Interface*, 12(113):20150821.

[151] Warrick, D. R., Tobalske, B. W., and Powers, D. R. (2005). Aerodynamics of the hovering hummingbird. *Nature*, 435(7045):1094.

[152] Weickgenannt, C., Roisman, I. V., and Tropea, C. (2015). Pinch-off of a stretching viscous filament and drop transport. *New J. Phys.*, 17(8):083059.

[153] Wilcoxon, F. (1945). Individual comparisons by ranking methods. *Biometr. Bull.*, 1(6):80–83.

[154] Xu, C., Zhang, Z., Fu, J., and Huang, Y. (2017). Study of pinch-off locations during drop-on-demand inkjet printing of viscoelastic alginate solutions. *Langmuir*, 33(20):5037–5045.

[155] Yang, L., Tu, Y., and Fang, H. (2010). Modeling the rupture of a capillary liquid bridge between a sphere and plane. *Soft Matter*, 6(24):6178–6182.

[156] Zhang, P., Mines, J. M., Lee, S., and Jung, S. (2016). Particle-bubble interaction inside a hele-shaw cell. *Phys. Rev. E*, 94(2):023112.

[157] Zhang, X., Padgett, R., and Basaran, O. (1996). Nonlinear deformation and breakup of stretching liquid bridges. *J. Fluid Mech.*, 329:207–245.